2-oxazoline-based plasma coatings for anti-fouling applications

Tim Egghe

Supervisors: Prof. dr. ir. Nathalie De Geyter, Prof. dr. ir. Richard Hoogenboom
Counsellors: dr. Pieter Cools, Joachim Van Guyse

Master's dissertation submitted in order to obtain the academic degree of Master of Science in Biomedical Engineering

Department of Applied Physics
Chair: Prof. dr. ir. Christophe Leys

Department of Organic and Macromolecular Chemistry
Chair: Prof. dr. José Martins

Faculty of Engineering and Architecture
Academic year 2016-2017

GHENT UNIVERSITY

2-oxazoline-based plasma coatings for anti-fouling applications

Tim Egghe

Supervisors: Prof. dr. ir. Nathalie De Geyter, Prof. dr. ir. Richard Hoogenboom
Counsellors: dr. Pieter Cools, Joachim Van Guyse

Master's dissertation submitted in order to obtain the academic degree of Master of Science in Biomedical Engineering

Department of Applied Physics
Chair: Prof. dr. ir. Christophe Leys

Department of Organic and Macromolecular Chemistry
Chair: Prof. dr. José Martins

Faculty of Engineering and Architecture
Academic year 2016-2017

GHENT UNIVERSITY

Permission of usage

The author gives permission to make this master dissertation available for consultation and to copy parts of this master dissertation for personal use. In the case of any other use, the copyright terms have to be respected, in particular with regard to the obligation to state expressly the source when quoting results from this master dissertation.

Date: 02/06/2017

Foreword

First of all, my thanks go to Prof. dr. ir. Richard Hoogenboom and Prof. dr. ir. Nathalie De Geyter for allowing me to work on this subject and for their support through the year. I owe my deepest gratitude to Pieter Cools and Joachim Van Guyse. Your guidance, knowledge, dedication and patience helped me in delivering this work. Furthermore, I would like to thank the people of the Supramolecular Chemistry group and RUPT. Special thanks go to Maria for synthesizing the BuOx, Luismi for donating the 4-methoxy-4-oxobutanoic acid and Maarten and Bart for distilling my products, Tim for preparing and helping with my set-up and Joris and Stijn for helping me with problem along the way. Also a special thanks towards the tissue engineering group for the cell tests, towards Petra and Prof. Dr. Coenye for the bacterial adhesion tests and to dr. Edmondo Benneti for the protein adhesion tests. I would also like to thank my friends, especially my friends of the SLO for the support during this hard year. And last but not least, I want to thank my parents for allowing me to follow my own path during my studies, and my sister and my girlfriend, for all the support.

2-oxazoline-based plasma coatings for anti-fouling applications

Tim Egghe
Supervisors: Prof. dr. ir. Nathalie De Geyter, Prof. dr. ir. Richard Hoogenboom
Counsellors: dr. Pieter Cools, Joachim Van Guyse

Abstract **To this day a significant portion of all implanted medical devices fail prematurely, as the implant cannot perform its intended task or causes adverse reactions in the body. The most important reactions involved in implant failure are inflammation, fibrosis, thrombosis and infection and subsequent biofilm formation. A possible strategy for avoiding these reactions, is a surface modification with anti-fouling coatings, which resist protein and bacterial attachment. There are however some drawbacks linked to the typical anti-fouling brushes, for which plasma polymerization can be a solution. Therefore, the aim of this thesis is to develop anti-fouling coatings via plasma polymerization of 2-oxazolines with a varying side chain. Differences in coating stability and chemical composition were assessed for the varying side chain. However, bacterial adhesion and cell tests indicated that the obtained coatings had no anti-fouling effect.**

Keywords **Anti-fouling coating, plasma polymerized 2-oxazolines, stability, chemical composition**

I. INTRODUCTION

Medical implantations are common procedures that often save lives or ameliorate the quality of life of patients. However, these procedures come with certain risks: to this day a significant portion of all implanted medical devices fail prematurely, as the implant cannot perform its intended task or causes adverse reactions in the body. This premature failing poses a significant burden for the patient, which will require new medical intervention to either replace or remove the failed implant or to suppress the immune system. In order to minimize adverse reactions to implants within the body, the design parameters of the implant should be optimized. Some of these parameters are related to the bulk constituents of the implant, others are related to the material surface. Usually, the bulk constituents of existing implants are already designed to show the desired features. Thereto, extensive research towards implant surface modification is performed, as the surface is the part of the implant that interacts mostly with the body.

The most important of the aforementioned adverse reactions are inflammation, fibrosis, thrombosis and infection and subsequent biofilm formation. [1] [2] These are triggered by initial protein attachment to the implant. Therefore, interest is going to implant surface modification with anti-fouling coatings. These coatings resist protein and bacterial attachment, which results in the inhibition of biofilm formation, inflammation, fibrosis and thrombosis. Anti-fouling coatings have been applied as molecularly thin self-assembled monolayers (SAMs), polymer brushes, and thin or bulk hydrogels. Different polymers are used for anti-fouling brushes, which are the most widely described kind of anti-fouling coatings. In general, the mechanisms of action leading to the anti-fouling properties of these brushes are not yet fully understood, though several factors have been found to add to the non-fouling behaviour: the electrical neutrality reduces electrostatic interactions with charged protein domains, the hydrophilicity reduces nonpolar interactions between proteins and hydrophobic surfaces, protein adsorption may also be reduced by steric hindrance and likely, their hydrophilic nature results in the formation of a hydration layer which inhibits protein interaction with the coating. [3] Poly (Ethylene Glycol) (PEG) is the golden standard of anti-fouling brushes, but is has some disadvantages, such as the oxidative degradation of the polyether backbone among others. [4] Therefore, research shifted to other anti-fouling polymers with an increased stability: zwitterionic polymers, Poly(hydroxy-functional) acrylates, poly(glycerol) and peptido-mimetic polymers like poly(2-alkyl/aryl-2-oxazoline)s (PAOx), poly(vinyl-pyrrolidone) and poly(peptoids).

There are however some drawbacks related to the use of anti-fouling coatings. The anchoring of the coating to the implant surface requires a multi-step process which is performed in solvents. This increases the amount of chemical waste, making the coating process not environmentally friendly and increasing the cost. Therefore, in this research, an alternative way of applying anti-fouling coatings to a substrate is researched. This method uses plasma polymerization, which is a one-step, surface independent technique. It uses no solvent or initiator and therefore, it causes no liquid organic waste production. It also consumes minimal monomer quantities. This makes it a cost effective and environmentally friendly technique and therefore, an interesting alternative to the conventional application of non-fouling coatings. [5] Previous studies report successful plasma polymerization of PEG-like and PAOx-like coatings with an anti-fouling effect. [5], [6]

In this research, the aim is to synthesize peptido-mimetic anti-fouling coatings, because of its increased stability in comparison with PEG-like coatings. Therefore, 2-oxazolines (monomer for PAOx synthesis) are chosen as plasma precursor, as previous plasma polymerization of these monomers resulted in coatings with a high amide-content. [5] Additionally, 2-oxazolines have a high structural variability, enabling the plasma polymerization of several monomers and a specific reactivity towards acids is reported for 2-oxazoline plasma coatings, which makes the coating interesting for functionalization. In this thesis, five 2-oxazoline monomers are used: 2-methyl-2-oxazoline (MeOx), 2-ethyl-2-oxazoline (EtOx), 2-*n*-propyl-2-oxazoline (PrOx), 2-*n*-butyl-2-oxazoline (BuOx) and methyl 3-(2-oxazoline-2-yl) propanoate (C_2-MestOx). These monomers are also shown in its respective order in figure 1.

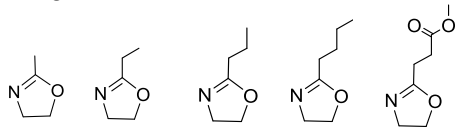

Figure 1: 2-oxazoline precursors used for plasma polymerization in this thesis

By comparing the plasma polymerization of the first four monomers in figure 1, the difference in stability, wettability, chemical composition, deposition speed and non-fouling capacity of the deposited coatings for a growing aliphatic side chain is investigated. By comparing the fifth monomer in figure 1 with the previous monomers, the influence of an extra hydrophilic functionality in the side chain on the stability, wettability, chemical composition and anti-fouling capacity of the plasma polymerized coatings can be studied.

II. Materials and Methods

A. Materials

The used solvents were of HPLC grade and include: dichloromethane (DCM, ≥99.8%, Sigma-Aldrich), acetonitrile (ACN, ≥99.9%, Sigma-Aldrich) *N,N*-dimethylacetamide (DMA, _99.9%, Sigma-Aldrich) and triethylamine (TEA, ≥99.5%, Sigma-Aldrich). Chloroform-D (CDCl3, ≥ 99.8%) was purchased from Euriso-top. Dry DCM, TEA and ACN were obtained from a custom made JW Meyer solvent purification system and dried over aluminum oxide columns.

The following chemicals were used as received: butyronitrile (≥99%, Sigma-Aldrich), ethanolamine (≥99%, TCI), zinc acetate dihydrate (≥98%, Sigma-Aldrich), BaO (90%, Acros Organics), $MgSO_4$ (anhydrous, 97%, Acros Organics), ($SOCl_2$ (≥99%, Sigma-Aldrich), 2-chloroethylamine hydrochloride (98%, Acros Organics), sodium carbonate (Na_2CO_3, anhydrous, 99.95%, Sigma-Aldrich), methyl-*p*-toluenesulfonate (MeOTs, 98%, Sigma-Aldrich), 2-ethyl-2-oxazoline (≥99,8%, Polymer Chemistry Innovations), 2-methyl-2-oxazoline (98%, Chemical point) 4-methoxy-4-oxobutanoic acid (synthesized in the group).

Argon (Alphagaz 1) was purchased from Air Liquide and used as supplied. A roll of polypropylene (PP) (thickness: 0.05 mm, biaxially oriented) and a roll of ultra-high-molecular-weight polyethylene (UHMWPE) (thickness: 0.25 mm) was ordered from Goodfellow Cambridge UK.

B. Monomer synthesis

For the synthesis of PrOx, Butyronitrile (1 eq.) and ethanolamine (1.1 eq.) were mixed together, while zinc acetate was added in catalytic amounts (0.02 eq.). [7] The solution was refluxed for three days at 130°C. After the reaction, two fractional distillations were performed. The first fractional distillation was performed to obtain the product from the residual mixture. The second distillation was performed to remove water and ammonia. A yield of 54% was obtained after the second distillation. The formation of the product was confirmed with proton nuclear magnetic resonance (^{1}H-NMR) (Bruker Avance 300 MHz Ultrashield spectrometer) and liquid chromatography mass spectrometry (LC-MS) (Agilent 1100 HPLC). The same synthesis strategy was used for BuOx, but valeronitrile is used instead of butyronitrile.

For the synthesis of C_2-MestOx, 2-chloroethylamino hydrochloride was added to the acid chloride dissolved in dry dichloromethane (DCM). [8] Then, dry TEA was added dropwise. The water and organic phase of the resulting mixture were separated. The organic phase was dried with $MgSO_4$ and all volatiles were removed. As a last step, ring closure of the C_2-MestOx-precursor was performed by addition of anhydrous sodium carbonate in a rotavapor set at 40°C and 50 mbar. The reaction mixture was filtered over celite and thereafter, the formed C_2-MestOx was purified by fractional distillation. A second distillation over BaO was performed to dry the product. A yield of 16% was obtained after the second distillation.

C. Plasma methods

The plasma activation and polymerization were performed in a dielectric barrier discharge reactor (DBD), which consists of a lower copper electrode that is covered with a ceramic layer and an upper woven stainless steel electrode through which the gas is fed. Further details are included in section B.2.

D. Electrical characterization

To electrically characterize the DBD, the applied high voltage and the resultant discharge current of the plasma reactor were measured. The high voltage applied to the lower copper electrode was measured using a 1000:1 high voltage probe (Tektronix P6015A). The discharge current was measured by measuring the voltage across a 50 Ω resistor connected in series with the reactor to the ground. Via Ohm's law, the discharge current was calculated. The obtained waveforms were recorded using a digital oscilloscope (Picoscope 3204A) and the discharge power was calculated by performing a discrete integration method of the multiplication of voltage and current.

E. Coating characterization

Static water contact angle (WCA) measurements were obtained at room temperature, using a commercial Kruss Easy Drop system (Krüss Gmbh, Germany). A water droplet of 2.0 µl was placed on the sample surface. The contact angle values, shown in this summary, are an average of at least 8 measurements at the right side of the sample.

Fourier transform infrared spectroscopy (FT-IR) analysis is performed with a Bruker Tensor 27, with a liquid N_2 cooled MCT detector. For each measurement, 64 scans are made. The scan region is 4000-700 cm^{-1} with a resolution of 4 cm^{-1}. Each sample was supported with 0.25 mm of UHMWPE, in order to avoid piercing the sample.

XPS surface analysis was performed on a PHI 5000 Versaprobe II spectrometer. This equipment uses a monochromatic Al K_α X-ray source (hv = 1486.6 eV) operating at 23.3 W. A vacuum of at least 10^{-6} Pa was obtained for all measurements. Surveys scans and high resolution spectra (C1s, N1s, O1s) were recorded with a pass energy of 187.85 eV and 23.5 eV respectively. 4 points on the sample are measured.

The thickness of the coating was measured with AFM, by using a XE-70 atomic force microscope (Park Systems), used in non-contact mode with silicon cantilever (Nanosensors TM PPP-NCHR).

F. Stability of the coating

To assess the stability of the coatings, 2 samples of approximately 0.7 x 1 cm^2 were incubated in deionized water for respectively three and seven days, while the other sample was stored in vacuum. An FT-IR measurement was performed on each sample as described. By taking the ratio of the area of an absorbance peak that is typical to the coating and an

absorbance peak from the substrate and the supporting UHMWPE, a measure of the thickness of the coating was obtained.

G. Anti-fouling capacity of the coating

To assess the anti-fouling capacity of the coating, cell tests and bacterial adhesion tests were performed. For the cell tests, all samples were sterilized by exposure to UV for 30 min. Human foreskin fibroblasts (HFF) were seeded onto samples in a 24-well plate at a density of 10.000 cells/1000 µL of medium per each. The cultures were incubated at 37°C under 5% CO_2 for 1 and 3 days. Cell proliferation and viability was measured for 1 and 3 days by an MTT assay and life/dead staining. Tissue culture polystyrene (TCPS) was collected as a positive control for the MTT assay.

For the bacterial adhesion tests, all samples were sterilized by 30 minutes UV exposure. The microorganisms were grown on Tryptic Soy Agar (TSA) (Oxoid, Drongen, Belgium) (*P. aeruginosa* and *S. aureus*) under aerobic conditions at 37°C. Using a sterile forceps, the samples were placed in the wells of a 24-well microtiter plate and subsequently 1 mL of the cell suspension, containing approx. 104 colony forming units (CFU)/mL was added. The plates were incubated for 4 h at 37 °C. Following incubation, the samples were transferred to 10 mL 0.9% (w/v) NaCl and subjected to three cycles of 30 s vortex mixing and 30 s sonication. Tenfold serial dilutions were made in 0.9% (w/v) NaCl and the number of CFU was determined by plate counting. To this end, one mL of each dilution was plated on TSA and the plates were incubated at 37°C for 48 h.

III. Results and Discussion

A. Electrical characterization

A pulsed power supply was used, in order to reduce the heating of the electrode and obtain lower monomer fragmentation. Due to the nature of the used voltage source, a small amount of power was still supplied during the 'off'-period. The sinusoidal voltage generates a discharge current that comprises a superposition of a sinusoidal waveform and several small current peaks. This indicates that the DBD set-up is operating as a pseudo-glow discharge. This leads to a homogeneous plasma treatment of the sample. There is a change in duty cycle in between the different monomers: for plasma polymerized EtOx (pPEtOx), a duty cycle of 54.6 %, was observed, while a duty cycle of 62.6 % was observed for the other monomers. By changing the voltage during the 'on'-period, different powers are applied.

B. Incompatibility of C_2-MestOx

The second day after the monomer was inserted in the set-up, no monomer was flowing when the valve was opened. Opening the set-up made clear that the monomer was solidified. The valve in the controlled evaporation and mixing (CEM) system was also blocked by the solidified monomer. It may also be possible that the high boiling point (56°C at 0.3 mbar for the destillation) has influenced the mass flow. By introducing a bubbler system for the evaporation of the monomer, a set-up could be designed that can be compatible with the C2-MestOx. The other results will not be presented of this monomer, because of its limited relevance.

C. Water contact angle measurements

Initial water contact angle (WCA) measurements indicated that the WCAs varied over the sample surface. The inhomogeneity of the WCA over the sample indicates that different plasma conditions were present in the reactor, which resulted in an inhomogeneous coating composition over the sample surface. A similarity for the varying WCA is observed for all monomers: by increasing the power, the WCAs at the right side of the sample increased to a stable value. The WCAs at the right side of the sample were taken as reference and a more detailed study of these WCAs in function of the applied power was performed. These results are shown in figure 2.

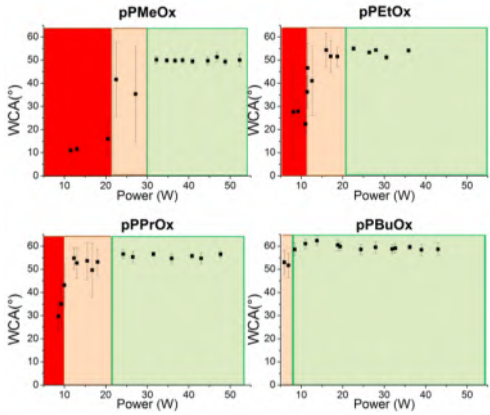

Figure 2: WCA for pPMeOx, pPEtOx, pPPrOx and pPBuOx as a function of discharge power. The colors mark three different zones in each graph (green: 'stable', orange: 'metastable' and red: 'unstable').

Figure 2 shows three different regimes for the WCAs for each monomer. The names for the regimes are explained in section D. In the 'stable' regime (at high powers, green area in figure 2), the WCAs are comparable at the right side of the sample, resulting in small standard deviations. In the 'metastable' regime (at intermediate powers, orange area in figure 2), some WCAs at the right side of the sample are still comparable with the WCAs of the first regime, but lower WCAs are measured, which results in larger standard deviations. In the 'unstable' regime (at low powers, red area in figure 2), no WCAs are comparable with the WCA of the first regime.

Despite a lack of data in the transition zones between the regimes, a clear trend is observed: the borders of the 'stable' and 'metastable' regime shift towards lower powers with a growing aliphatic side chain. No clear distinction can be made between pPEtOx and pPPrOx. This can probably be attributed to the difference in duty cycle for pPEtOx: the on-period mostly contributes for the P_{avg} at the boundary limit power and it is expected that this period mostly determines the composition of the coating. As the 'on'-period is shorter for pPEtOx, the power during this peak will be higher compared to the peak power during the 'on'-period for pPPrOx at the same P_{avg}. Therefore, the boundary limit of the 'stable' regime would be at a higher peak power for pPEtOx than for pPPrOx,

further indicating the observed trend. However, further measurements would be needed to confirm this hypothesis.

It is a remarkable result that the WCA is constant in regime 1. This indicates that a similar coating composition is obtained at a wide range of different applied powers for these monomers. Further, a clear trend is observed towards higher WCAs for the growing aliphatic side chain of the monomers in this regime. This can be correlated to an increasing carbon content in the plasma coating for the growing aliphatic side chain, as also illustrated with XPS.

D. Coating stability

The stability assessment of the coating is shown in figure 3. These results were obtained with an integration method with an oblique baseline. Similar results were obtained with a straight baseline.

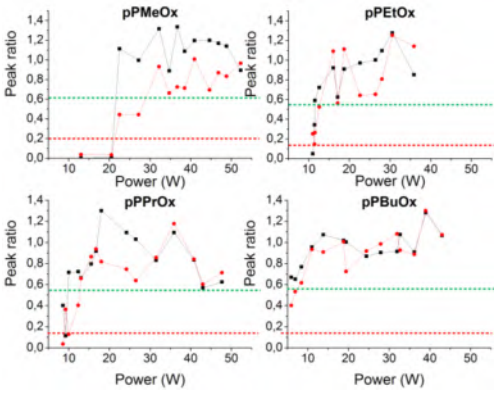

Figure 3: Ratio of the area of characteristic coating peak (scaled to substrate peak) for 3 (black) and 7 (red) days on the characteristic coating peak (scaled to substrate peak) for 0 days. Areas are calculated with integration method 1.

Several variables influence the FT-IR measurement, and therefore, this stability assessment can only be used as a qualitative technique. Three different regimes can be distinguished, based on WCA measurements and the stability assessment: regime 1: 'Stable' coatings: if the WCAs of the plasmOx-coating reach a stable value (which is different for each monomer as illustrated in figure 2) over a total surface area, the observed peak ratio did not drop below 0.55. This value is chosen, based on the lowest peak ratios of pPPrOx and the peak ratio of pPBuOx in regime 2 on figure 2. 'Stable' does not refer to a coating that does not lose any of its thickness. This cannot be concluded out of the used stability assessment. 'Stable' refers to a coating that still has a considerable FT-IR signal at the specific coating peak (at least a peak ratio of 0.55) after seven days of incubation in deionized water. Regime 2: 'Metastable' coatings: the WCAs of the plasmOx-coating over a total surface area are composed of a mixture of both high WCAs (corresponding with stable values of regime 1) and low WCAs. A considerable FT-IR signal at the specific coating peak cannot be expected anymore after water incubation, but its presence is still a posibility. However, an FT-IR signal at the specific coating peak will be present to a lesser extent, indicating still a presence of coating after 7 days of water incubation. At peak ratios between 0.2 and 0.55, loss of coating thickness is highly plausible. Regime 3: 'Unstable' coatings: the WCAs of the plasmOx-coating over a total surface area are composed of considerably lower WCAs than in regime 1. Incubation in water of these samples will lead to a considerably lower FT-IR signal at the specific coating peak. A significant amount of the coating is lost. A peak ratio lower than 0.2 was measured for these coatings. A shift of the borders of the 'stable' and 'metastable' regime towards lower powers with a growing aliphatic side chain is observed. Comparing this stability boundary for molar flow, instead of the mass flow, still indicates the same trend. This is a strong indication that cross-linking via the side chain is promoted with increasing side chain length.

E. Chemical composition

1) FT-IR

A typical FT-IR spectrum of a plasma polymerized 2-oxazoline is presented in figure 4.

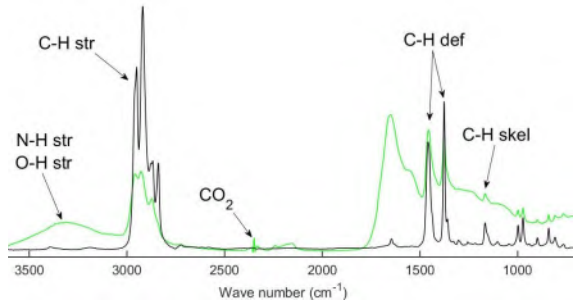

Figure 4: FT-IR signal of the PP (substrate) and UHMWPE (backing) (green) and pPEtOx Pavg=35.86 W.

Several peaks of the PP+UHMWPE spectrum are also observed in the signal of the pPEtOx sample. These are indicated with an arrow in figure 4. The peaks between 3000 and 2800 cm^{-1}can be assigned to C-H stretching vibrations, while the peaks at 1459 and 1375 cm^{-1} correspond to C-H deformations. All coatings have a broad peak between 3500 and 3000 cm^{-1}, which can be assigned to N-H or O-H stretching vibrations. Making a distinction between them is difficult in this case. The broader peak around 2345 cm^{-1} is a consequence of bad CO_2 compensation of the software and is not related to the coating. The small broader peak between 2250 and 2150 cm^{-1} is observed for all different monomers. There are differences in the form of this small broad peak for the different monomers, but an analysis in function of power and monomer did not indicate clear trends in these differences. All FTIR-measurements of the coatings resulted in a small broad peak that seemed to be composed of 4 peaks. Assigning these peaks is difficult, because of the unknown plasma process. Possibly, the peaks at 2243 cm^{-1} and 2154 cm^{-1} corresponds to a nitrile (range: 2260-2230 cm-1) and an isonitrile (range: 2175-2130 cm-1) respectively. The peaks at 1656 and 1547 cm^{-1} are difficult to assign. The peaks at lower wavenumbers than 1375 cm^{-1} (indicated C-H def in figure 4), show no consistency in function of power and monomer. Because of the unknown plasma process and the ambiguous assignment of the most pronounced peaks, no analysis of these peaks is performed.

2) XPS

The results of the XPS surveys are presented in table 1, where all values are averaged in the stable and unstable region.

Table 1: Overview of the elemental contents for the four plasma polymerized monomers.

C content (at%)	pPMeOx	pPEtOx	pPPrOx	pPBuOx
'Stable' region	76.3 ± 1.1	79.8 ± 1.8	80.3 ± 1.1	81.8 ± 1.4
'Unstable' region	73.5 ± 1.5	79.0 ± 1.1	78.3 ± 1.9	79.7 ± 1.5*

N content (at%)	pPMeOx	pPEtOx	pPPrOx	pPBuOx
'Stable' region	15.8 ± 0.7	12.1 ± 1.8	10.7 ± 0.8	9.4 ± 0.9
'Unstable' region	16.5 ± 0.6	11.6 ± 0.9	11.6 ± 1.3	10.0 ± 1.0*

O content (at%)	pPMeOx	pPEtOx	pPPrOx	pPBuOx
'Stable' region	7.7 ± 0.6	8.1 ± 0.9	8.9 ± 0.7	8.8 ± 0.9
'Unstable' region	10.0 ± 1.4	9.4 ± 0.5	10.0 ± 1.0	10.3 ± 0.7*

For the 'stable' region, the oxygen content does not change significantly, while a decrease in nitrogen content and a corresponding increase in carbon content is noticed. For the 'unstable' region, a significant increase in oxygen content is observed with respect to the 'stable' region. The nitrogen content does not seem to change significantly for 'stable' and 'unstable region. The carbon content is significantly lower for pPMeOx at 'unstable' coatings in comparison with the 'stable' coating, as expected by the oxygen content increase. For the other monomers, this change in content is less pronounced. This may indicate that stability of the coating is obtained by more partitioning of oxygen containing particles. The higher amount of oxygen in the 'unstable' regime can be related to the lower WCAs. In the 'stable' region, the increase of the carbon content can be related to the increasing WCAs in function of a longer aliphatic side chain. A greater increase in carbon content is observed between pPMeOx and pPEtOx than compared to the other monomers. This may be linked to a higher fragmentation of the side chain when this side chain becomes longer.

The high resolution spectra of the different monomers in function of power do not show major differences or trends. In figure 5, one example of high resolution spectra of a plasma polymer is given, which is representative for the other plasma polymers. Also included in this figure, is the comparison with pPEtOx, (poly-2-ethyl-2-oxazoline) (PEtOx) and ring-opened poly-(2-isopropenyl-2-oxazoline) (RO-PIPRO). PEtOx is the polymer obtained by the cationic ring opening polymerization of EtOx and it contains tertiary amides, while RO-PIPRO contains secondary amides and esters.

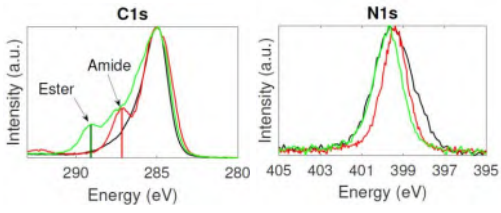

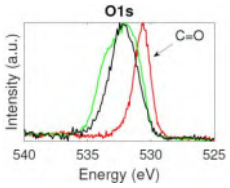

Figure 5: High resolution C1s-, N1s- and O1s-spectra from pPEtOx (Pavg=35.86 W) (black), PEtOx (red) and RO-PIPRO (green).

This comparison gives an indication that other processes are involved in the plasma polymerization than in the conventional polymerization. This can be observed in the C1s-spectrum of the coatings, where no pronounced amide peak is present. An extensive formation of tertiary amides can also be excluded on the basis of the O1s-spectrum. This does not mean that no secondary or tertiary amides are present in the coating, but it is clear that these structures will not be the main component of the coating.

3) Influence of water incubation

The differences between the water incubated samples and the samples that were stored in vacuum is compared. In FT-IR measurements, a peak broadening of the peak at 3500-3000 cm^{-1} is observed, which may indicate that relative to the amount of N-H functionalities, more O-H functionalities are present in the coating after water incubation. This may be caused by reaction of the coating with water or by residual water in the coating that is not evaporated after vacuum incubation. The peak at 2154 cm^{-1} also disappears, which could be an indication that this peak originates from isonitriles, as isonitriles undergo acid catalyzed hydrolysis (deionized water is slightly acidic).

From XPS surveys, it is clear water incubation results in a decrease in C and N content and a corresponding increase in O content. This is probably caused by a reaction of N-containing groups with water. These groups could for example be imines or isonitriles. The presence of isonitriles is previously discussed in this section, while the presence of imines will be discussed in section 4.

From high resolution spectra, a clear shift in the N1s-spectra after water incubation, is observed. This may be caused by the aforementioned reaction of N-containing groups with water. In the other spectra, no clear trends are visible.

4) NMR

Because of the dificulties with determining the chemical composition of the coatings, an additional analysis technique is tested at the end of this thesis. Therefore, ^{1}H- and ^{13}C-NMR spectra were measured of a dissolved coating. The ^{1}H-NMR-spectrum of pPPrOx is compared with the spectra of conventionally polymerized PrOx and the monomer in figure 6.

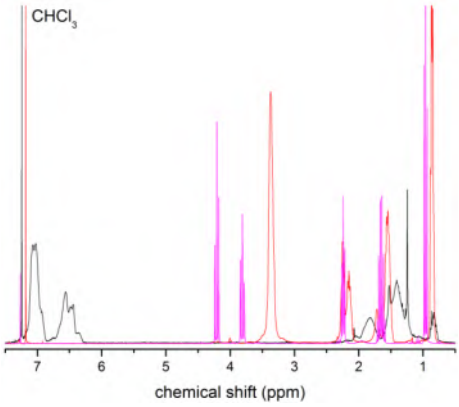

Figure 6: ^{1}H-NMR spectrum of pPPrOx Pavg=30.5 W (black), PPrOx (red) and PrOx (purple).

The spectrum for pPPrOx is remarkable: the plasma process can be expected to have a random character, but only a limited amount of different peaks is observed, indicating the presence of a number of well defined processes. It is clear that the peaks around 7.0 and 6.5 ppm, which correspond to the coating, are not found in the monomer or polymer. The peak at 3.37 ppm of PPrOx, corresponds to the protons of the carbon adjacent to the nitrogen of the amide. This excludes the presence of tertiary amides in a large amount. This also excludes the presence of secondary amides in a large amount, as the carbon adjacent to the nitrogen will also have a similar chemical shift. The absence of the peaks typical to the oxazoline, exclude the presence of closed oxazoline-rings in high amounts in the coating. The peaks below 2 ppm for the plasmOx-coating relate to different protons in aliphatic bonds. Associating a chemical structure is difficult because of the unknown plasma process. It is also difficult to draw conclusions based on one NMR-measurement. Likely, the peak at 6.80-6.28 ppm in the ^{1}H-NMR is related with the proton bounded to the carbon in an imine. This also corresponds with the ^{13}C-NMR-spectrum. The peak at 7.23-6.85 ppm is more difficult to designate. A possible chemical structure that corresponds with this peak is an oxazole or another type of aromatic proton. This can also explain the fluorescence that was observed from a pPEtOx coating. Further research is however needed to confirm this.

F. Deposition speed

Measurements to assess the deposition speed indicated a large variation in coating thickness, which can be explained by the high Ar flow that is used for plasma polymerization. With the designed strategy, it was not possible to observe clear trends in the deposition speed of the different monomers.

G. Anti-fouling capacity of the coating

The cell proliferation tests, as well as the bacterial adhesion tests indicated no anti-fouling effect. As illustrated in figure 7, good cell proliferation is observed for the coatings. This compromises the use of these coatings in anti-fouling applications, but they could be interesting substrates for tissue regeneration.

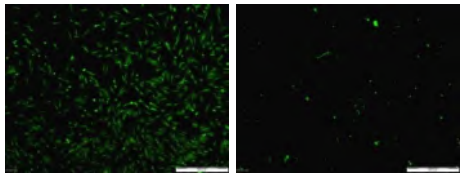

Figure 7: Life/dead staining after 1 day of cell culture for pPBuOx (P_{avg}=25.1W) (left) and untreated PP (right).

IV. Conclusions

'Stable' coatings were obtained for 4 different 2-oxazolines. A link was observed between the stability and the WCAs and a shift of the boundary for which the coatings became 'stable' at the right side of the reactor is also observed for an increasing aliphatic side chain. The lack of anti-fouling behaviour of the coatings can be attributed to the chemical composition of the plasmOx-coating, which is different from conventional PAOx. FT-IR and XPS have proven to be insufficient to efficiently characterize the coating composition and therefore, no conclusion could be made within this thesis on the chemical composition of the coating. However, XPS data could strongly indicate that the coating is not mainly composed of amides, in contrast to PAOx. Further analysis is needed to identify the chemical composition of the coating. The lack of anti-fouling character differs from previously reported plasma polymerized 2-oxazoline-coatings. These studies postulated an anti-fouling effect of the coatings. It is however not clear if this effect is originating from the coating itself or from coating detachment.

References

[1] W. J. Hu, J. W. Eaton, T. P. Ugarova and L. P. Tang, "Molecular basis of biomaterial-mediated foreign body reactions," *Blood*, vol. 98, no. 4, pp. 1231-1238, 2001.

[2] J. M. Anderson, A. Rodriguez and D. T. . Chang, "Foreign body reaction to biomaterials.," *Seminars in Immunology*, vol. 20, no. 2, pp. 86-100, 2008.

[3] S. Lowe, N. M. O'Brien-Simpson and C. L. A, "Antibiofouling polymer interfaces: poly(ethylene glycol) and otherpromising candidates," *Polymer Chemistry*, vol. 6, no. 2, pp. 198-212, 2015.

[4] R. Konradi, C. Acikgoz and M. Textor, "Polyoxazolines for nonfouling surface coatings - A direct comparison to the gold standard PEG," *Macromolecular Rapid Communications*, vol. 33, no. 19, pp. 1663-1676, 2012.

[5] M. N. Macgregor-Ramiasa, A. a. Cavallaro and V. Krasimir, "Antibiofouling Properties of Plasma-Deposited Oxazoline-Based Thin Films," *ACS Applied Materials and Interfaces*, vol. 8, no. 10, pp. 6354-6362, 2016.

[6] F. Brétagnol, M. Lejeune, A. Papadopoulou-Bouraoui, M. Hasiwa, H. Rauscher, G. Ceccone, P. Colpo and F. Rossi, "Fouling and non-fouling surfaces produced by plasma polymerization of ethylene oxide monomer.," *Acta Biomaterialia*, vol. 2, no. 2, pp. 165-172, 2006.

[7] M. A. Boerman, H. L. Van der Laan, J. C. M. E. Bender, R. Hoogenboom, J. A. Jansen, S. C. Leeuwenburgh and J. C. M. Van Hest, "Synthesis of pH- and Thermoresponsive Poly(2-n-propyl-2-Oxazoline)," *Polymer chemistry*, vol. 54, p. 1573–1582, 2016.

[8] P. J. M. Bouten, D. Hertsen, M. Vergaelen, B. D. Monnery, M. A. Boerman, H. Goossens, S. Catak, J. C. M. van Hest, V. Van Speybroeck and R. Hoogenboom, "Accelerated living cationic ring-opening polymerization of a methyl ester functionalized 2-oxazoline monomer.," *Polymer Chemistry*, vol. 6, no. 4, pp. 514-518, 2015.

Contents

List of abbreviations

Ar	argon
ACN	acetonitrile
BaO	barium oxide
BuOx	2-*n*-butyl-2-oxazoline
C_2-MestOx	methyl 3-(2-oxazoline-2-yl) propanoate
$CDCl_3$	chloroform-D
CEM	controlled evaporation and mixing
CF_4	tetrafluoromethane
CFU	colony forming units
CROP	cationic ring-opening polymerization
DBD	dielectric barrier discharge
DCM	dichloromethane
DMA	N,N-dimethylacetamide
ESI	electrospray ionization
EtOx	2-ethyl-2-oxazoline
FBGC	foreign body giant cells
FT-IR	fourier transform infrared spectroscopy
FWHM	full width at half maximum
GC	gas chromatography
^{1}H-NMR	proton nuclear magnetic resonance
He	helium
HFF	human foreskin fibroblasts
HPLC	high-performance liquid chromatography
LC-MS	liquid chromatography–mass spectrometry
LDA	lithium diisopropylamine
MeOTs	methyl-*p*-toluenesulfonate
MeOx	2-methyl-2-oxazoline
$MgSO_4$	magnesium sulfate
n-BuLi	*n*-butyllithium
N_2	nitrogen gas
Na_2CO_3	sodium carbonate

NH_3	ammonia
O_2	oxygen gas
PAOx	poly(2-alkyl/aryl-2-oxazoline)s
PBS	phosphate-buffered saline
PBuOx	poly-(2-*n*-butyl-2-oxazoline)
PDI	polydispersity index
PEtOx	poly-(2-ethyl-2-oxazoline)
PEG	poly(ethylene glycol)
PHEMA	poly(2-hydroxyethyl methacrylate)
PIPRO	poly-(2-isopropenyl-2-oxazoline)
PlasmOx	plasma-polymerized 2-oxazoline
PMeOx	poly(2-methyl-2-oxazoline)
PMMA	poly(methyl methacrylate)
pPBuOx	plasma-polymerized 2-*n*-butyl-2-oxazoline
pPC_2-MestOx	plasma-polymerized methyl 3-(2-oxazoline-2-yl) propanoate
PP	polypropylene
pPEtOx	plasma-polymerized 2-ethyl-2-oxazoline
ppm	parts per million
pPMeOx	plasma-polymerized 2-methyl-2-oxazoline
pPPrOx	plasma-polymerized 2-*n*-propyl-2-oxazoline
PPrOx	poly-(2-*n*-propyl-2-oxazoline)
PrOx	2-*n*-propyl-2-oxazoline
PVA	poly(vinyl alcohol)
RGD	arginylglycylaspartic acid
RO-PIPRO	ring-opened poly-(2-isopropenyl-2-oxazoline)
SAM	self-assembled monolayers
SEC	size exclusion chromatography
slm	standard liter per minute
$SOCl_2$	thionyl chloride
TEA	triethylamine
THA	total hip arthroplasty
TKA	total knee arthroplasties
TMEDA	tetramethylethylenediamine
TMS	tetramethylsilane
UHMWPE	ultra-high-molecular-weight polyethylene
WCA	water contact angle
XPS	x-ray photoelectron spectroscopy
YF	Yasuda factor

Chapter 1

Medical implants

Medical implants are devices or tissues that are placed inside or on the surface of the body. [1] They can have different intended functions, like the replacement or support of a body part, the delivery of medication and/or the monitoring of body functions. The number of medical implantations has risen over the past years and will continue to rise in the future, due to the aging population and the increasing prevalence of chronic diseases. Data of 2011 estimates the amount of the eleven most implanted medical devices around 6.7 million per year in the United States alone. [2] In recent years, the market of medical implants has continuously expanded and a specific market study predicts a growth of the market for at least 7 more years. [3]

1.1 Problems related to medical implantation

Implantations of medical devices are therefore considered to be common procedures. They often save lives or ameliorate the quality of life of patients, but they also involve certain risks: to this day a significant portion of all implanted medical devices fail prematurely, as the implant cannot perform its intended task or causes adverse reactions in the body. This situation often poses a significant burden for the patient, sometimes even leading to death. The processes that accompany medical implantation and cause implant failure are quite complex. The following sections will provide a general overview of these different processes.

In general, the implantation of a medical device can cause reactions like inflammation, fibrous tissue formation, thrombosis and infection, but also other adverse reactions can take place. [4] All together, these

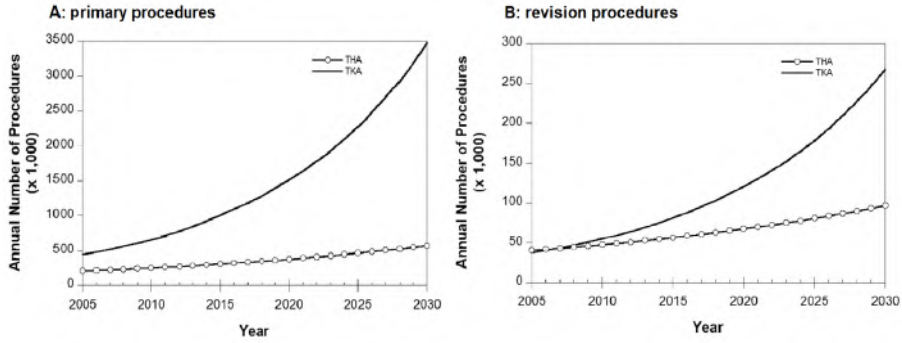

Figure 1.1: The projected number of primary total hip arthroplasty (THA) and total knee arthroplasty (TKA) procedures (A) and revision procedures (B) in the United States from 2005 to 2030. [6]

reactions can lead to the aforementioned complications or failure of the implant. Inflammation, fibrous tissue formation and thrombosis immediately relate to the effects of the implant on the body and *vice versa*. These processes are described in section 1.2, where the concept of biocompatibility is introduced. Infection, on the other hand, is a major cause of adverse body reactions originating from biofilm formation by invading microorganisms. This process is explained in section 1.3.

Avoiding complications and implant failure, and the aforementioned reactions, is of major importance. Even if the risk of implant failure for the patient is non-life threatening, this still demands supplementary medical care, which increases the financial burden on healthcare systems. [5] A common strategy for minimizing the body reaction to the implant is modifying the implant surface instead of changing the implant bulk material. This will be explained in chapter 2, based on the considerations of sections 1.2 and 1.3.

Total knee arthroplasties (TKA) and total hip arthroplasties (THA), two of the most commonly reported procedures, are taken as an example to illustrate the increasing importance of medical implants and the problems related to medical implantation. A projective study estimated the growth of the number of THA and TKA procedures in the United States as shown in figure 1.1.A, illustrating the expanding medical implant market. [6] Figure 1.1.B illustrates that the need for revisions will increase according to the rising prevalence of THA and TKA procedures.

The three most important failure modes or causes of revision of TKA are, according to Khan *et al.*, infection, instability of the implant and aseptic loosening, which is the failure of fixation of the implant that is

not caused by infection. [7] In two studies, respectively 39.9% and 33% of the total amount of revisions is caused by aseptic loosening, 27% and 38% of the revisions is caused by infection and 7.5% and 26% of the revisions is caused by instability of the implant. [5] To the best of the author's knowledge, no recent extensive studies of implant failure costs are published. A large study of the costs of TKA of 2010 estimated the average cost of a revision for TKA at 49 360 USD. [8] According to the aforementioned data, it becomes evident that the number of implant-related revisions will increase in the near future, resulting in an exorbitant cost to society.

1.2 Biocompatibility

Before a medical device can be implanted, it must satisfy a number of requirements. These requirements can be framed within the concept of biocompatibility. This concept is defined as followed: "Biocompatibility refers to the ability of a material to perform with an appropriate host response in a specific situation". [9] This definition comprises two aspects that will be treated separately. First, the medical implant should be able to perform its desired function. This means that the reaction of the body to the device should not interfere with the device function. An illustration thereof is the fibrous tissue formation during the foreign body response as described in section 1.2.1. This process can be beneficial to anchor the implant or disadvantageous when it isolates a part of the implant that should not be isolated. The sewing ring of a heart valve for example needs anchoring in the tissue. The newly formed fibrous tissue can perform this task. An example of disadvantageous fibrous tissue formation can be found in glucose sensoring: frequent *in vivo* calibration of the sensor is needed because of the decreasing response to glucose caused by the fibrous tissue formation. [10]

The second aspect in the definition is the requirement that the host response should be appropriate in a specific situation. This implies that biocompatibility is not a property of a material or implant itself. It can only be considered for the material together with the biological host. [11] This also implies that the host response should result in clinically acceptable effects as shown in figure 1.2.

Implantation will always elicit some reaction, but this should be limited and tolerable. An ideal implant should therefore comply with several requirements: [9], [12]

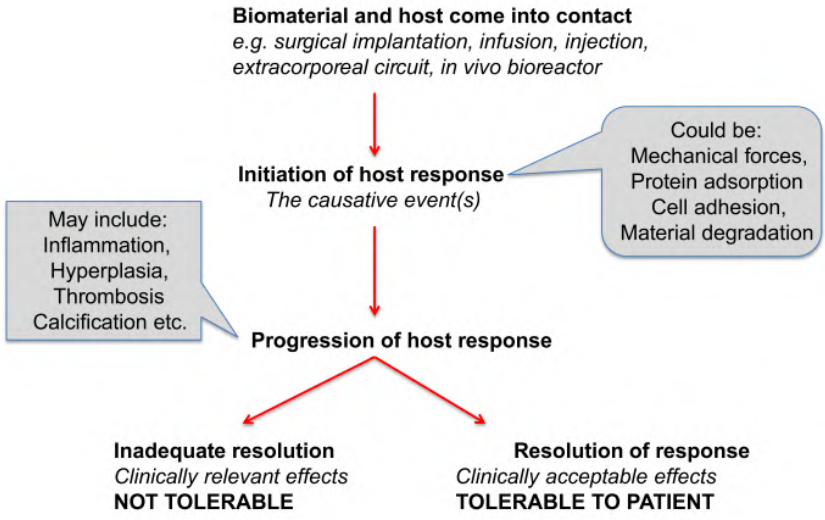

Figure 1.2: Scheme indicating the causative events after biomaterial and host tissue contact. [11]

1. The immunologic response as described in section 1.2.1 should be limited and should not cause excessive damage to nearby tissues.
2. The formation of thrombi or emboli, as described in section 1.2.2, should be avoided at all time.
3. The implant may not induce major cytotoxic or genotoxic effects.
4. The implant cannot cause hypersensitivity.
5. The implant may not be carcinogenic.

This all depends on a great number of different implant parameters. Some of them are related to the bulk of the materials of which the implant is made, others are related to the material surface. The most important factors are listed in table 1.1.

This thesis aims to develop a coating that can alter inflammation and the subsequent fibrous tissue formation, to which often is referred to as the foreign body response and thrombus and embolism formation. Therefore, only these processes are further described in the following sections. These sections will particularly illustrate the importance of initial protein attachment for the following course of the reaction. Naturally, the coating should also not cause any other adverse reaction like cytotoxic, genotoxic or carcinogenic effects.

Table 1.1: Factors influencing the host response.

Bulk properties		Surface properties
- Mechanical composition - Toxicity of metal ions for corrosion of metallic materials - Degradation profile, degradation product form and toxicity for polymeric and ceramic materials	- Wear debris release profile - Leachables, additives, catalysts, contaminants and their toxicity (for polymeric materials) - Elastic constants - Crystallinity and crystallography - Bulk porosity	- Surface chemical composition - Surface molecular mobility - Surface topography - Surface energy - Surface electrical/electronic properties - Surface porosity

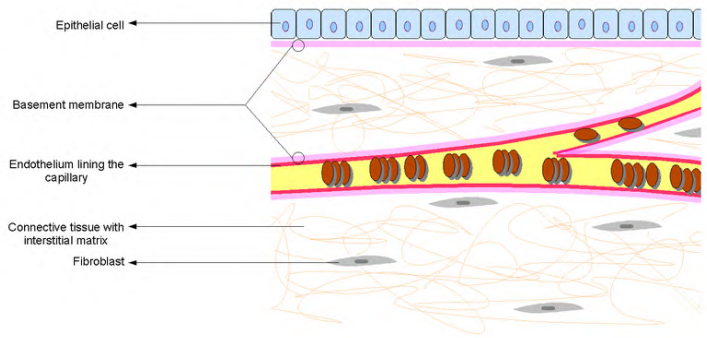

Figure 1.3: The basement membrane and its surrounding structures.

1.2.1 Foreign body response

The implantation of a medical device, causes a cascade of reactions, to which is commonly referred to as the foreign body response. [13] The first step is the injury of the tissue. This is accompanied by cell death, loss of extracellular matrix and loss of basement membrane structure, the latter being thin layers of extracellular matrix specialized in supporting epithelial and endothelial cells. [14] Cells can proliferate on them, making the basement membrane the extracellular base for blood vessels. The basement membrane and its surrounding structures are shown in figure 1.3.

The amount of cell death, loss of basement membrane, loss of extracellular matrix and the proliferative capacity of the damaged tissue will influence the development of new tissue after implantation. The pre-existing architecture of the tissue can be restored (restitution) or formation of fibrous tissue can occur. [12] Prior to new tissue formation, the blood in the damaged blood vessels will first interact with the material.

This process will be explained in section 1.2.1.1. Next, an inflammation process will take place, which will be explained in section 1.2.1.2. In section 1.2.1.3, the new tissue formation is described. These general reaction mechanisms deal with implantations in vascularized tissues, as these are the most abundant. The particular case for implantations in avascular tissues is not discussed in detail, but a similar body reaction will be obtained.

1.2.1.1 Blood-material interaction

When a medical implant is inserted in vascularized tissue, it can cause damage to the basement membrane and the surrounding blood vessels. This will be accompanied by three different processes. The first process is hemostasis, which aims to stop blood leakage from these blood vessels and to prevent invasion of microorganisms. [15], [16] This process consists of three steps:

1. Platelets, components in the blood stream, adhere to subendothelial matrix components, leading to platelet activation. [17] This results in the production and secretion of soluble agonists that will attract more platelets from the blood stream. Activation of these attracted platelets leads to a cascade reaction that results in the formation of a plug.

2. The damaged blood vessels contract to reduce the blood loss, which is known as vasoconstriction.

3. A complex cascade of reactions results in the formation of fibrin, which will come in contact with the platelets and form a more stable plug. This is called the blood coagulation cascade. It is mediated by different proteins, called blood clotting factors and it can start via two different ways: after contact with an activator, which can be an artificial surface, or after tissue damage. [18]

Hemostasis occurs rapidly: the adhesion of platelets happens within seconds and the first fibrin strands adhere to the clot within 30 to 60 seconds. Depending on the size of the damage, a stable clot is formed within a couple of hours.

The second process is the provisional matrix formation. Directly after the tissue damage, the permeability of the blood vessels is altered. Together with the blood vessel damage, this leads to leaking of blood

cells, proteins and fluid into the damaged tissue. This results in the fast formation of a blood protein layer on and around the implant. This is called the provisional matrix. As the body is now in direct contact with this protein layer, the composition of this matrix will influence the further reaction of the body. [4] The protein adhesion is surface mediated, causing the implant surface to have an influence on the reaction of the body. The adsorbed proteins show time variance: proteins with the highest mobility arrive first and over time they are replaced by proteins with a higher affinity towards the surface. This is described in literature as the Vroman effect. [19] Generally, albumin arrives first and is later replaced by fibrinogen, fibronectin and vitronectin among others.

The third process is the activation of the complement system. This is a series of proteins residing in the blood plasma and on cell surfaces, involved in inflammatory regulation. [20] Antigens, foreign body components and coagulation cascade activation among others, trigger interaction between the different complement components. [16] This results in the production of several components involved in the inflammation process.

1.2.1.2 The inflammation process

Chemoattractants secreted by blood clots and platelets and the activation of the complement system results in attraction of white blood cells to the implantation site. In particular neutrophils, monocytes and macrophages are attracted. As explained in the previous section, the material will be coated with plasma proteins over time. Also extracellular proteins will interact with the material surface. The protein matrix on the material will give the white blood cells adhesion opportunities. This happens through the use of integrins, which are trans-membrane proteins. They mediate cell-extracellular matrix adhesion and cell-cell interactions. They also can activate many intracellular signaling pathways. [21] For example, macrophages and monocytes can attach via various integrins to fibronectin, laminin, complement fragment C3bi, fibrinogen, Factor X, vitronectin and other extracellular proteins that contain Arginylglycylaspartic acid (RGD). [22] RGD is a tripeptide that is a common element in cellular recognition. Depending on which protein the integrin binds, different intracellular processes can be triggered. The conformation of the provisional matrix is therefore determining the inflammation reaction to the implant.

Neutrophils and macrophages will try to phagocytose foreign materials and microorganisms. [12] As the implant surface is greater than the

cell, it cannot be phagocyted. Following these inflammation processes, further reaction steps will occur depending on the surface to which the cells are bound. Macrophages can fuse together to form foreign body giant cells (FBGC). Macrophages and FBGC can both release products that will try to degrade the implanted material, like reactive oxygen free radicals and degradative enzymes. These can damage the surrounding tissue. The influence of the surface can be illustrated by following example: a breast prosthesis, which has a smooth surface, has one or two macrophage thick layer attached to it, while a vascular prosthesis with a rough surface has FBGCs and macrophages attached to it. [12]

1.2.1.3 Fibrous and grannulation tissue formation

Macrophages will also secrete growth factors that lead to the infiltration and proliferation of fibroblasts and endothelial cells in the implantation area. [23] In a process called angiogenesis, these growth factors activate endothelial cells. They secrete enzymes to locally degrade the basement membrane. The endothelial cells proliferate, migrate and organize themself at the injured area, to form new capillaries. [24] The proliferating fibroblasts synthesize collagen and proteoglycans. Over time, proportionally more collagen is produced. [25] Some fibroblasts can also differentiate into myofibroblasts, which have special contractile function to contract the wound. [23] The small blood vessels supply oxygen and nutrients to the forming tissue. Because of the granular appearance due to the invasion of a network of capillary blood vessels, this newly formed tissue is called granulation tissue. After maturation of this tissue, a fibrous vascularized capsule consisting of collagen is formed around the implant. This isolates the implant from the body. When the supporting extracellular structure can be maintained, no major cell death occurs and the original cells have a good proliferating character, the original cells can proliferate back into the injured area. Then, no fibrous capsule is formed but restitution of the original tissue is obtained.

1.2.2 Thrombosis and embolism

The processes of hemostasis and blood coagulation as described in section 1.2.1.1 create a clot at the material surface. The blood in the small damaged vessels can be isolated from the implant by this process. Another process, where the initial clot is dissolved by an enzyme called plasmin and replaced by new endothelial cells, creates a new closed blood vessel. The dissolution process is performed by the fibrinolytic

system, in which fibrin is degraded in soluble components. [26] These processes happen in all damaged blood vessels during implantation. But for blood-contacting devices, like artificial heart valves, catheters, stents and artificial grafts, the activation of platelets and the coagulation cascade can lead to the formation of a larger clot at the material surface than for other types of implants. Because of the amplifying cascade and the large surface in contact with the blood, the fibrinolytic system cannot compensate the blood clot formation. Hereby, a large blood clot can form at the surface of a blood-contacting device, which is called a thrombosis. This can compromise the functioning of the device in the case of a mechanical heart valve or block the blood flow in the case of stents or grafts. This can have serious consequences, like the induction of myocardial infarction or death in the thrombosis of coronary stents. [27] The blood clot can also detach to form an embolism.

1.3 Infection and biofilm formation

Besides the general reactions described in section 1.2, infection is another important factor that influences the success of medical implantation. It is a general problem for implantation applications, as almost any type of medical implant is susceptible to infections. [8], [28], [29]

Bacteria and fungi can infiltrate the patient in several ways, attach to the medical implant and start colonizing the surface. [30] This results in the formation of a so called biofilm. In this section, the different steps towards the formation of a biofilm are explained. Furthermore, it is important to note that the foreign body response that accompanies the implantation of a medical device, also leads to the formation of an immunosuppressive environment around the implant. [31], [32] This makes medical devices extra susceptible to infection.

1.3.1 Origin of the microorganisms

Bacteria and fungi live in a wide variety of habitats and just a small fraction of them are pathogenic for humans. [33] They also colonize different surface tissues of the body, namely the skin and mucosal membranes, like the mucosa of the gastrointestinal tract, the upper respiratory tract and oral cavity. [34] In the mixture of microorganisms, which is called the human flora, bacteria are far more abundant than fungi. This colonization of surface tissues is in contrast with the internal tissues that are normally free of microorganisms. If species of the normal

human flora remain in their normal biotope, they are non-pathogenic, but if they penetrate other areas, some of these species can cause pathogenic reactions. The implantation of a medical device can be the origin of bacteria or fungi entering areas where they normally not reside. This can occur during the surgical procedure: the implant surface can be infected prior to the implantation, bacteria or fungi can enter the patient via contaminated surgical equipment or disinfectants or from the surgeon's or patient's skin. [35] But bacteria and fungi can also reach the implant surface via hematogeneous spread of another infection site. [36] As bacterial biofilms are clinically most abundant and described the most in literature, the following sections describe specific bacterial biofilm formation. Parallels can be made for fungal biofilms.

1.3.2 Attachment of the microorganisms

Both types of bacterial infiltration as described in the previous section result in a number of microorganisms that are near the implant surface. Bacteria prefer to grow on available surfaces rather than in the surrounding aqueous phase. [37] They are moved to the material surface by physical phenomena such as Brownian motion, Van der Waals, electrostatic and hydrophobic forces. [38] The surface attachment process of the bacteria consists of two phases. In the first phase, the microorganism interacts non-specifically and reversible with the material surface via hydrophobic, electrostatic and Van der Waals forces. [29] In the second phase, bacterial surface adhesins will interact specifically and irreversible with host proteins that are adsorbed on the implant surface as explained in section 1.2.1. [39] An example is the specific interaction between *staphylococcus aureus* and fibronectin. [37] This is also shown in figure 1.4.

1.3.3 Biofilm maturation and detachment

Once the bacteria are adhered to the surface, cell proliferation and intercellular adhesion take place. So, the bacteria form microcolonies of layered cell clusters. The cells secrete polysaccharides in this phase, which facilitates further cell adhesion to the surface. These microcolonies then further develop into macrocolonies that are enclosed in an extracellular matrix. [35] The composition of this matrix varies between species. However, several biofilms contain polysaccharide, proteins and extracellular DNA. [40] A similar composition is observed for fungal biofilms. [41] The cells organize themselves in the matrix in such a way

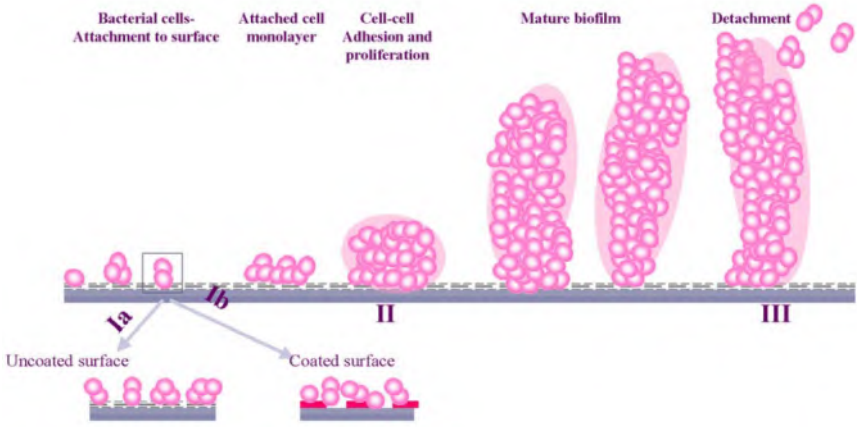

Figure 1.4: Different steps in the formation of a biofilm activation pathways. [37]

that fluid-filled channels in the matrix enable transport of nutrients to the cells at the bottom of the film. [42]

Based on the cell density, the bacteria modify their gene transcription which is called 'quorum sensing'. This plays a role in the biofilm formation and particularly in the last step of the biofilm formation, namely the detachment of cells from the biofilm. [36] Depending on the kind of species, different mechanisms play a role in the detachment phase, like enzymatic release in staphylococcus aureus biofilms. [40] In general, cells detach because of the depletion in nutrients and space. [35], [36] The dynamics and shear of the fluid contacting the biofilm, play also a role in the detachment. The bacteria can then move into the bloodstream and spread infection to other regions of the body. Aggregates of bacteria that detach can also cause embolic complications. [35] The contaminated implant is in this case a reservoir for infection towards the rest of the body.

1.3.4 Antimicrobial resistance

The major problem of biofilm formation is the resistance of the biofilm and the detached aggregates to antimicrobial therapy and the immune defense system. [43] The innate immune system is not able to effectively phagocytose the bacterial cells because of restricted access caused by the biofilm matrix. Antibodies of the adaptive immune system are not able to penetrate this matrix once the biofilm has matured. [36] This can

lead to a chronic inflammation at the surface and to a loosely attached implant, which is undesirable for orthopedic implants. [44], [45]

As the immune system is not capable of eliminating the bacteria, antimicrobial therapy could be the next option. However, different mechanisms make a biofilm highly resistant against therapies that normally can cope with planktonic bacteria. Firstly, the matrix limits diffusion of some antibiotics. [30] Secondly, antibiotics that can diffuse into the biofilm, can be inactivated by the extracellular polysaccharides or enzymes in the matrix and bacteria within the biofilm can develop a resistant phenotype for the antimicrobial therapy. [29] Also the growth rate plays a role: bacteria in a mature biofilm grow more slowly than their planktonic form and this is generally accompanied by a higher resistance towards antibiotics. [46]

Because of the antimicrobial resistance of the biofilm, it is very difficult to effectively treat the infected patient. The standard procedure is still the removal of the implant. In cases where the removal is not possible, continued suppressive antibiotic treatment to prevent regrowth of the biofilm is recommended. [47] However, new strategies are emerging, like the interference with 'quorum sensing' and the modulation of a signaling pathway involved in the detachment of the biofilm. [47], [48]

Chapter 2

Surface modifications

As discussed in section 1.2, the reaction of the body towards any implant depends on the bulk material and the surface. For existing devices, the used materials are biomaterials that already limit the adverse effects to the body. The implant is already designed to show the desired features. An example is the load bearing capacity of orthopedic implants. [49] However, progress can still be made to avoid biofilm formation and the foreign body response. Thereto, extensive research towards implant surface modification is performed, as the surface is the part of the implant that interacts mostly with the body. [50] Hereby, the desired bulk properties remain, while the surface characteristics can change the body response largely. [51] For example, the surface of orthopedic implants evolved from smooth to rough to promote new bone formation instead of fibrous tissue formation as discussed in section 1.2.1. [52]

Many different kinds of surface modifications exist, depending on the application. A possible distinction can be made between two types of coatings:

1. Bioactive coatings are designed to interact with the host tissue. These coatings can be used for implants that need good integration with the tissue or interaction with the body can be used to avoid the unwanted reactions as described in chapter 1.

2. Bioinert or non-fouling coatings are designed to avoid interaction with the host tissue. These coatings are used for implants where tissue integration is unwanted. Ideal bioinert coatings also avoid the foreign body response, infection and thrombus formation. This will be explained in great detail in section 2.2.

As this thesis pursues a new generation of non-fouling coatings, bioactive coatings will not be discussed in much detail.

2.1 Bioactive coatings

The composition of the bioactive coating depends on the intended application. Describing all different types of coatings lies outside of the scope of this thesis and therefore, some examples are used to explain the most relevant kind of coatings.

1. Bioactive coatings can be used to limit the inflammation related to medical implantation. This can be done by delivering immunomodulatory agents in soluble form from the coating. These agents can also be immobilized on the surface. [53]

2. Biofilm formation can be inhibited by the use of antimicrobial coatings. A number of different antimicrobial coatings exist and new strategies are still developed. Comparable to anti-inflammatory coatings, two different types of antimicrobial coatings can be distinguished. The first type is a release-based coating, where the antimicrobial substance leaches out of the coating. The second type is a non-release based coating, where the antimicrobial substance is immobilized on the surface. [51] Common examples of antimicrobial substances are antibiotics, antimicrobial peptides, metals like silver and copper and nitric oxide.

3. Restriction of thrombosis can also be achieved by bioactive coatings. Several thrombin inhibitors, like heparin, bivalirudin and hirudin, have been immobilized on the implant surface. [54] Perfectly inhibiting thrombin formation, also inhibits fibrin production. As a result, no blood clot formation takes place. Heparin also exhibits anti-inflammatory properties. [53]

4. To promote new bone formation instead of fibrous tissue formation in orthopaedic implants, a number of coating strategies exist. An example is the coating with hydroxyapatite, a calcium phosphate structure found in the natural apatite bone minerals. The apatite layer acts as a scaffold for osteoblasts. Over time, this matrix is resorbed by osteoclasts and replaced by new bony tissue. [55] Hydroxyapatite coatings promote better implant integration.

Ongoing research studies possible combinations of different strategies. To illustrate such a combination, the examples of TKA and THA in chapter 1 are taken. To minimize the two most occurring modes of failure, namely loosening of the implant and infection, two kinds of bioactive coatings can be combined. In the above enumeration, coatings 2. and 4. can be used to achieve this goal. A clinical study of Eto *et al.* involves a hip implant that is coated with silver oxide-containing hydroxyapatite. [56] *In vivo* tests of this coating with rats already indicated comparable osteoconductivity to normal hydroxyapatite and suppressed inflammation and bacterial proliferation. First results of 20 patients show no infection and no implant failure due to loosening after 1 year. However, more clinical data is needed to support the evidence that the coating inhibits biofilm formation.

In general, the bioactive coatings described in the aforementioned enumeration also face problems. Immobilized antimicrobial can be insufficiently sensitive to react to weak stimuli. [57] Release based antimicrobial coatings solve this problem, but they are prone to other complications: the long-term stability due to the limited reservoir, cytotoxicity, inflammatory responses, the controlled release of the substance and the fouling of the surface with cells and proteins. [58] This last problem is also of major relevance for anti-inflammatory coatings and anti-thrombotic coatings. [54], [53]

2.2 Non-fouling coatings

Ideal non-fouling coatings do not interact with the body. Non-fouling coatings have been applied as molecularly thin self-assembled monolayers (SAMs), polymer brushes, and thin or bulk hydrogels. This section will specifically focus on the attachment of non-fouling brushes, as they are most widely described and of most interest for this thesis. Moreover, SAMs have limited stability, making them less interesting for applications. [53] Non-fouling coatings are also referred to as anti-fouling or ultra-low fouling coatings. Non-fouling refers to ideal coatings not undergoing any fouling. In the remainder of this thesis, 'non-fouling coatings' is used for coatings that prevent substantial fouling.

Firstly, the clinical relevance of non-fouling coatings will be explained in section 2.2.1. Then, the characteristics of non-fouling brushes are described in section 2.2.2. After that, examples of polymers used for non-fouling brushes are discussed in section 2.2.3. To conclude, the

general problems related to the use of non-fouling brushes is discussed in section 2.2.4.

2.2.1 Clinical relevance

Non-fouling coatings owe their properties to their ability of preventing any interaction of the body towards the coating. An ideal non-fouling coating prevents all protein and cell adsorption. As protein adsorption determines the body response as explained in section 1.2 and bacterial attachment as explained in section 1.3, non-fouling coatings will alter the following complications of implantation:

1. Non-fouling surfaces will influence the foreign body response. Because the protein adsorption cannot take place or at least is minimized, less or no white blood cells will adhere to the surface. This will lead to less activation and a reduced foreign body response. [59] Recently, the implantation of a zwitterionic non-fouling hydrogel in mice resisted fibrous capsule formation for three months, leading to the belief that a completely non-fouling coating can prevent the foreign body response. [60]

2. Thrombosis and embolisms are caused by the interaction of plasma proteins and the implant. An inert material surface would prevent these reactions and thus prevents the formation of a large blood clot. [61] This would theoretically eliminate the need for chronic anticoagulant and antiplatelet therapies. Besides life-long costs, these therapies cause dangerous side-effects, like the induction of a hemorrhage, as they limit the capacity of the blood to clot. [62][63] Medical implants that eliminate or reduce the need of anticoagulation or antiplatelet therapy, would be a great progress in implant technology. It should however be noted that blood clot formation is not only influenced by the surface of an implant. Implantation can for example lead to blood stasis, which also activates the coagulation cascade. [64]

3. Non-fouling coatings inhibit biofilm formation. By inhibiting protein adsorption, bacteria and fungi cannot attach specifically to the implant and remain in their planktonic state. [65] So, they are more susceptible to antimicrobial therapy and the immune system.

Thus, non-fouling coatings can solve several problems related to medical implantation. It is a particularly interesting coating strategy because

it solves multiple problems at once. With bioactive coatings, a combination of strategies is needed to achieve the same result. As the fibrous tissue formation is absent or at least altered, a loosely integrated implant will be the result. This is advantageous for applications like catheters and biosensors, but other implants, like orthopedic devices, will not be able to perform its intended task without adhesion and integration of the implant. [66] Therefore, interest is also going to non-fouling coatings with bioactive functions. As such, the coating is not non-fouling anymore, but it can be referred to as a targeted non-fouling coating: the coating should maintain the bacteria and protein repellant properties and should only be cell-interactive. An example is the integration of adhesion peptide sequences in the coating. [67], [68] This type of coatings can also play another important role: if an implant can be fully colonized by cells of the patient, microbes cannot adhere to the surface anymore. This competitive process between microbes and the normal tissue is sometimes referred to as 'the race for the surface'. [69]

2.2.2 Characteristics of non-fouling brushes

To prevent protein adsorption, non-fouling brushes need to have certain characteristics. In 2001, Chapman *et al.* [61] described the characteristics of non-fouling coatings: they should be hydrophilic, overall electrically neutral and have hydrogen-bond acceptors but not hydrogen-bond donors. However, the 'no hydrogen-bond donors' criterion seems to be the least important for polymer brushes, as polymer brushes containing poly(vinyl alcohol) (PVA), poly(glycerol) or poly(2-hydroxyethyl methacrylate) (PHEMA) show good non-fouling properties. [70] In general, the mechanisms of action leading to the non-fouling properties of these brushes are not yet fully understood, though several factors have been found to add to the non-fouling behaviour: the electrical neutrality reduces electrostatic interactions with charged protein domains, the hydrophilicity reduces nonpolar interactions between proteins and hydrophobic surfaces, protein adsorption may also be reduced by steric hindrance and likely, their hydrophilic nature results in the formation of a hydration layer which inhibits protein interaction with the coating. [71] In general, the higher the chain density, the better the non-fouling character of the coating. [72] The chain length should not be too small, making sure that the expected interactions can take place, but the chain length should not be too large either, to avoid entanglement of the chains, reducing its performance. [73]

2.2.3 Examples of non-fouling polymers

A wide range of non-fouling polymers exists. Two polymers are discussed in more detail in sections 2.2.3.1 and 2.2.3.2: poly(ethylene glycol) (PEG) is the gold standard of non-fouling coatings and poly(2-alkyl/aryl-2-oxazoline)s (PAOx) are relevant for this thesis. In section 2.2.3.3, a number of other common examples are shown. [71],[74–77]

2.2.3.1 Poly (Ethylene Glycol) and its derivatives

PEG is the golden standard in polymer-based biomedical applications, due to its low polydispersity, biocompatibility and non-fouling behavior. [78] It remains the golden standard of non-fouling polymer brushes, owing its properties to the characteristics described in section 2.2.2. [71] Additionally, PEG-based coatings give nanoparticle drug delivery systems stealth behavior: by the formation of surface barrier layers, nanoparticles become 'invisible' to phagocytic cells. [79] The body does not interact with the nanoparticle system and thus does not recognize it. This leads to increased circulation time in the body, because the particles are phagocytized more slowly than without the coating. [77] However, the use of PEG is linked to some disadvantages: the polyether backbone of PEG is prone to oxidative degradation. This makes the polymer less interesting for long term applications as non-fouling surfaces for implants. Besides this aspect, complement activation that is probably induced by PEG has been observed. Also the development of anti-PEG antibodies has been observed in some patients, including 25 % of patients never treated with PEG drugs (due to its ubiquity in cosmetics, and food additives). [78] Additionally, a variety of compositions and applications of PEG-based formulations are protected by patents. This hinders further research and development. [78] In more recent years, research shifted towards other types of non-fouling polymers because of these problems. The examples in section 2.2.3.2 and 2.2.3.3 have similar or better non-fouling capacity than PEG and their improved stability is already tested or at least expected because of their chemical structure.

2.2.3.2 Poly(2-oxazolines)

An alternative to PEG are PAOx. PAOx are a biocompatible polymer class with numerous biomedical applications. [78] They are synthesized by the living cationic ring-opening polymerization of 2-oxazolines. This

provides low polydispersity and the possibility of synthesizing well-defined block copolymers. The polymerization also gives the ability to choose the end-group functionality by selection of initiator and terminator and the ability of tuning the polymer side chains by selection of the 2-oxazoline monomer. [80] Different side chains in the polymer alter the hydrophilicity and thermoresponsive behavior of the polymer. Beside the selection of the 2-oxazoline monomer, these characteristics can be specifically tuned by the synthesis of specific block co-polymers. These polymers are also peptidomimetics, with a structure isomeric to that of polypeptides. [81]

The thermoresponisivity of these polymer class makes them suitable for drug and gene delivery. [82] Several studies show the ability of poly(2-oxazoline)s to be used in polymer-drug conjugates, polymer-protein conjugates and polymeric micelles with respect to drug delivery. [78] Particularly, poly(2-methyl-2-oxazoline)s (PMeOx) proved similar non-fouling capacity as PEG in *in vitro* studies. [83], [81] Poly(2-ethyl-2-oxazoline)s (PEtOx) also showed non-fouling character in a dynamic test. [84] However, this result is not directly comparable to performances of other coatings.

The major advantage of these polymers with respect to PEG, is their better chemical stability. This is related to the less polarized N-vicinal C-H bonds in poly(2-oxazoline)s in comparison with the O-vicinal C-H bonds in PEG. Degradation processes initiated through hydrogen abstraction are thus less likely. [85] This is also proven by studies that compare these two polymers in a reactive medium consisting of a hydrogen peroxide solution. [70] Pidhatika *et al.* proved that poly(2-methyl-2-oxazoline) brush coating lost only 10-20 % of the initial mass in this environment, while PEG brush coatings revealed a mass loss of 40-60 %, which also diminished their non-fouling properties. [85]

2.2.3.3 Other examples of anti-fouling coatings

In table 2.1, other examples of anti-fouling coatings are presented.

Table 2.1: Examples of non-fouling polymers.

Name	Structure	Non-fouling capacity	Stability
Zwitterionic polymers	Example: Poly (carboxybetaine methacrylate) 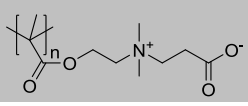	Comparable to PEG. Some zwitterionic polymers like the example given even surpass PEG.	*In vivo* stability of 3 months for a zwitterionic hydrogel. For brushes, *in vitro* stability of 15 days in undiluted bovine serum is observed.
Poly(hydroxy-functional) acrylates	Example: poly(2-hydroxy-propylmethacrylate) 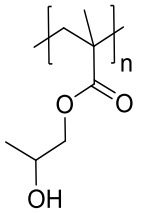	Comparable to PEG. Some polymers like the example given even surpass PEG.	*In vitro* stability up to 20 days in PBS. A higher stability is observed for these polymers than zwitterionic polymers.
Poly (glycerol)	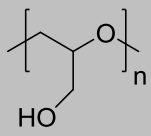	Comparable to PEG. No extensive tests in complex media are performed.	Less susceptible to oxidation or thermal stress than PEG. No direct comparison between poly (glycerol) and other polymer brushes is made.
Poly(vinyl pyrrolidone)	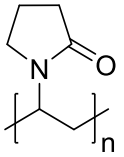	Comparable to PEG.	Comparable to Poly(2-oxazoline)s in 1h study. No extensive studies are present.
Poly (peptoids)	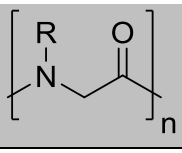	Comparable to PEG.	*In vitro* stability up to 5 months.

2.2.4 General problems of non-fouling polymer coatings

All this promising research shows a number of general problems. The first one is the extraction from good *in vitro* results to *in vivo* performance. PEG and PHEMA hydrogels gave good results *in vitro*, but *in vivo*, fibrous tissue formation was observed. As this was not seen in zwitterionic hydrogels described by Zhang *et al.*, this is an indication that protein adsorption still took place. [60] As this adsorption could still lead to microbial attachment, these hydrogels would not be perfect as antimicrobial coatings. This deviation between *in vitro* and *in vivo* tests is caused by the increased complexity of protein fouling *in vivo*. Not only because protein structures and conformation can vary in different biological environments, but also due to the diversity of proteins and the unknown influence among different proteins and/or compositions in biological media. [86]

The second problem is the multi-step process of anchoring the coating to the implant surface. At least, a polymerization step is needed to create the polymer brushes and an anchoring step is needed to attach the polymer brushes to the implant. On top of that, sometimes additional steps are required for the synthesis of the monomer building blocks. The third problem is related to this multi-step process: the application of the coating to the implant is performed in solvents. This increases the amount of chemical waste, making the coating process not environmentally friendly and increasing the cost. [87]

Therefore, in this thesis, an alternative way of applying a non-fouling coating to a substrate is researched. This method will be explained in chapter 3.

Chapter 3

Plasma polymerization of non-fouling coatings

A solution for the problem discussed in section 2.2.4, is the use of plasma technology, more specifically plasma polymerization. Plasma polymerization solves the problems related to the conventional chemical coating strategies. It is a one-step substrate-independent process: the polymerization and anchoring step proceed simultaneously. It is a solvent- and initiator-free technique, causing no liquid organic waste production. It also uses minimal monomer quantities. [88] This makes it a cost effective and environmentally friendly technique and therefore, an interesting alternative to the conventional application of non-fouling coatings. [89]

Firstly, this chapter will introduce the general concepts of plasma technology in section 3.1. Secondly, the plasma polymerizations for non-fouling coatings described in literature are summarized in section 3.2. Based on this, the strategic approach for the synthesis of non-fouling coatings in this research is explained in section 3.3. In section 3.4, the synthesis methods are described for the monomers that are used in this thesis. To conclude, the goal of this research is explained in section 3.5.

3.1 Plasma technology

Plasma is a partly ionized gas that is generated by supplying energy to a neutral gas causing the formation of charge carriers. [90] As such, plasma is sometimes referred to as the fourth state of matter. [91] The ionized gas is a mixture of highly excited electrons and atomic,

molecular, ionic and radical species. [92] A subdivision is made between thermal and non-thermal plasmas. The particles in a thermal plasma are in a thermal equilibrium: electrons as well as heavy particles have the same temperature situated around 4000-5000 K or higher. In non-thermal plasma, there is a thermal difference between electrons and heavy particles: electrons have a high temperature, while the heavier particles have a low temperature, giving the total plasma a lower temperature. This can still result in a temperature of a few 1000 K. To avoid degradation of the plasma treated material, only non-thermal plasma treatment is suitable for polymeric biomedical applications. In this case, the degree of ionization is kept below 1%. [93]

The necessary energy needed to create a plasma can be supplied in various ways. The most commonly used method of generating a plasma in lab environment is the application of an electric field to a neutral gas. Any neutral gas contains a few electrons and ions, resulting from the interaction of cosmic rays or radioactive radiation with the gas. The electric field will accelerate these free charge carriers, leading to creation of new charged particles when the accelerated charge carriers collide with other gas particles or with the surfaces of the electrodes, resulting in plasma formation. [90]

3.1.1 Plasma sources

There are a number of different concepts in which an electric field can be used to generate a plasma. For each concept, different plasma reactor designs are possible. Discussing all different concepts and designs lies outside the scope of this chapter. A widely used design that is also used in this research, is the dielectric barrier discharge (DBD). It is a type of discharge in which at least one of the electrodes is covered with a dielectric material. [94] Different configurations can be used. Several examples of the volume discharge configuration are shown in figure 3.1.

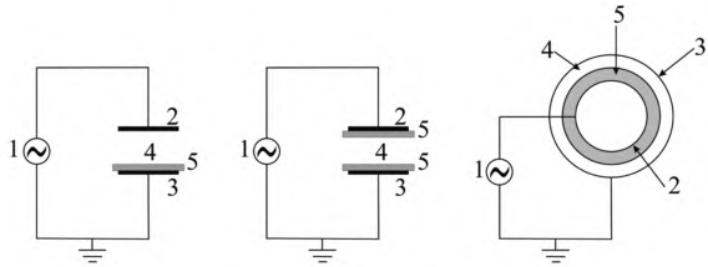

Figure 3.1: Typical planar and cylindrical DBD configurations: (1) Alternating high voltage source; (2) High voltage electrode; (3) Ground electrode; (4) Discharge gap; (5) Dielectric barrier. [91]

A high alternating voltage is supplied to one the electrode, with a typical frequency in the range of 1 to 100 kHz and an amplitude sufficient for breakdown. [91] The other electrode is grounded. The high voltage creates ionization in the discharge gap, causing the created charge to accumulate at the dielectric surface. This counteracts the applied electrical field, reducing the current flow after a few nanoseconds and counteracting breakdown. This process takes place in a large number of independent microdischarges. The exact duration of these discharges depends on the pressure, gas composition, and dielectric properties. [91] The dielectric barrier limits the amount of charge and energy deposited in a microdischarge and distributes the microdischarges over the entire electrode surface. [95] A dielectric barrier discharge set-up has a number of advantages: the possibility of working at higher pressures eliminates the need for extensive vacuum equipment. This makes the set-up cheaper and time-effective. There is also low heat generation, enabling a wider application range. [93]

3.1.2 Plasma applications

Plasma can interact with a material surface in different ways. The parameters of the plasma process will determine the dominant interaction. Depending on the main interaction, different applications of plasma can be distinguished.

3.1.2.1 Plasma activation

Plasma activation is the process where several gases can be used to create functional groups or free radicals on the surface of polymers. [91]

Common gases are argon (Ar), helium (He), oxygen gas (O_2), nitrogen gas (N_2), ammonia (NH_3), and tetrafluoromethane (CF_4). A plasma generated from a noble gas, like Ar and He, will introduce free radicals onto the surface. When the surface is then exposed to the air, oxygen will interact with these radicals. [96] Plasmas of other gases will introduce new chemical functionalities onto the surface that depend on the kind of gas. For example, O_2-plasma treatment leads to the introduction of oxygen-containing functional groups such as carboxylic acid groups, peroxide groups (due to postplasma reactions), and hydroxyl groups, while nitrogen, ammonia and N_2/H_2-plasmas introduce primary, secondary, and tertiary amines, as well as amides. [91] In general, most plasma treatments introduce polar groups onto the surface leading to a more hydrophilic surface. [97]. However, the plasma treatment with CF_4 for example, leads to the incorporation of C-F bonds onto the surface, which results in a very hydrophobic surface. [98]

Surface characteristics introduced by plasma activation can change over time, a process often referred to as 'ageing'. From thermodynamics, it is known that a system strives to minimize its (surface) energy. To accomplish this, surface adaptions can take place. Polar groups will be oriented outside of the surface in an aqueous environment, while in air, they will be reoriented towards the bulk of the material. [91] A study of Sharma *et al.* showed that the helium plasma treatment of polycarbonate films resulted in an initial increase of the wettability from 93 degrees to 30 degrees, but after three days, it already decreased to values around 60 degrees. [99] This change can be explained by the reorganization of the hydrophilic groups onto the surface. Due to ageing, it is therefore important to look at the properties of the implant surface upon the implantation time when it is plasma modified, as they can change over time. [100]

3.1.2.2 Plasma cleaning and etching

Besides activation, the reactive species in a plasma also have a cleaning effect. Plasma is efficient in the inactivation of some kinds of viruses, bacteria and fungi, although the reaction mechanisms are still under debate. [101] Plasma was also effective in removing protein residues from dental implants for example and carbon contamination from titanium. [102], [103] This process takes place without having any major influence on the underlying surface. [93]

Besides a cleaning effect, plasma will also have an etching effect. The etching efficiency depends on the material surface, the discharge power

and the treatment time. Hard materials will need a longer treatment time and/or higher discharge powers, while polymers will experience some kind of etching effect when exposed to a non-thermal plasma. [93]

3.1.2.3 Plasma polymerization

Plasma polymerization is the process where a precursor is introduced in a plasma, leading to conversion of the monomer into reactive fragments. These fragments combine to polymers in the gas phase and they are deposited on a substrate. [91] Plasma polymerization differs substantially from chemical polymerization: in a plasma, the active radicals introduce initiation sites for polymerization on the substrate surface and the monomer molecules, leading to nonspecific bindings. [93] This is in contrast with chemical polymerization, where the initiation process is specific and leads to specific bonds between monomer molecules. This results in a plasma polymer that will not necessarily have a structure and composition comparable to polymers achieved by conventional polymerization. Another consequence is the fact that organic compounds that cannot polymerize via conventional polymerization, can form a plasma-polymer. [104]

A number of different processes is involved in plasma polymerization and their relative contributions are still not completely understood. In general, the electrons in the plasma will cause further ionization, leading to the formation of reactive plasma gas and monomer-derived compounds. Depending on the inertness of the plasma gas, the monomer-derived compounds will solely react with each other or with each other and the plasma gas. Besides radical formation and recombination, also fragmentation, ion-molecule interactions and other reactions ultimately lead to the formation of a polymer network. [105] This network is in general amorphous, highly cross-linked and free from pinholes. [106] To chemically anchor the polymer film to the surface, the plasma polymerization process is almost always preceded by plasma activation. [93]

The plasma process parameters influence the chemical composition of the plasma polymer film and the deposition rate. The Yasuda factor (YF) is an important quantity in this regard:

$$YF = \frac{W}{MF} \tag{3.1}$$

with power W (J/s), monomer flow rate M (mol/s) and molecular weight of the monomer F (kg/mol). [105] This factor represents the apparent

power input for monomers of different molecular weight. [96] Different regimes can be distinguished for plasma polymerization: for high YF, the discharge power is more than sufficient to fragment the monomers. This is the 'monomer deficient' region. Further power increase will result in further fragmentation of the monomer, leading to lower deposition rates. In the 'monomer sufficient' region, excess monomer is present in the reaction chamber. Increasing the power will result in a larger amount of monomer that participate in the plasma polymerization. This results in a higher deposition rate for higher powers. In between two regions, there is a 'competition range'. In this range, there is no increase of deposition rates or plasma treatment efficiency with increasing YF.

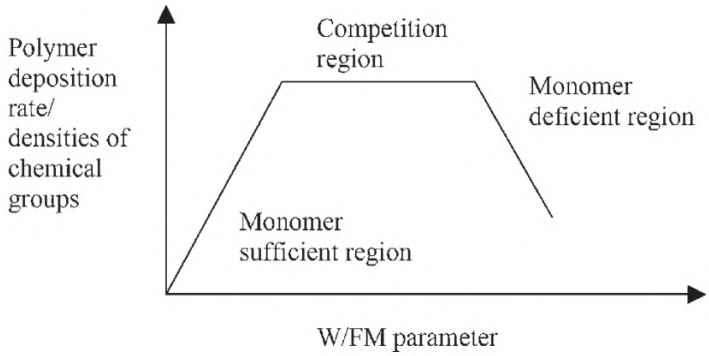

Figure 3.2: Schematic representation of the regions of plasma polymer deposition. [96]

Most research aims to retain a substantial density of the functional groups of the monomer. This requires less extensive fragmentation of the monomer. Therefore, most studies use plasma conditions that fall into the 'monomer sufficient' region.

Functional group retention can be enhanced by applying a pulsed power while maintaining plasma polymerization. In a pulsed power system, energy is not continuously supplied to the plasma. There is a period where energy is supplied but there is also a period where no energy is supplied to the plasma. During the 'on'-pulses, plasma polymerization can gets initiated and after the pulse is over, the reactive compounds that are created can further interact with each other and form oligomer fragments. For monomers containing a vinyl group, which polymerize via a radical mechanism, the plasma polymerization process will at least partially resemble the chemical polymerization mechanism. [105] Using a pulsed plasma system has two other advantages: a higher peak

Table 3.1: Examples of plasma precursors for deposition of PEG-like coatings.

Name	Structure	Name	Structure
Di(ethylene glycol) vinyl ether	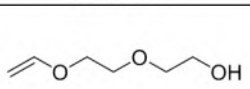	12-Crown-4-Ether	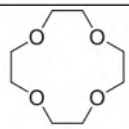
Di/tri/tetra (ethylene glycol) dimethyl ether (n=2,3,4)	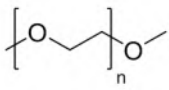	15-crown-5-ether	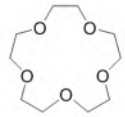

discharge power can be used without thermally damaging the substrate and a more homogeneous coating is applied. [93]

3.2 Examples of plasma polymerizations to obtain non-fouling coatings

Plasma polymerization has gained interest over the years as a medium for the deposition of non-fouling coatings. Hereby, the disadvantages of the chemical deposition of non-fouling coatings, as described in section 2.2.4, can be avoided. Typically, the monomers used for plasma polymerization are comparable to the monomers needed for the conventional polymerization of the polymers discussed in section 2.2. This is done to synthesize plasma coatings with comparable characteristics as the conventional non-fouling coatings. However, it is no certitude that the same non-fouling character from the conventional polymers can be achieved by the plasma polymer, because of the difference in polymerization characteristics as discussed in the previous section. In the following subsections, different efforts of plasma polymerization of non-fouling coatings are described.

3.2.1 Plasma polymerization for PEG-like coatings

Several research groups used different plasma precursors to deposit PEG-like coatings. Examples are given in table 3.1. [107–112]

All these precursors have the typical ether bond that is also found in PEG. The retention of these bond in the plasma polymerization process

is an important factor in the performance of the coating in repelling proteins and bacteria. The highest retention (85%) was achieved by Johnston *et al.* for 2 precursors (tetra (ethylene glycol) dimethyl ether and 15-crown-5). [112] Apparently, a retention of approximately 60% and higher leads to good non-fouling behavior. [107] Higher retention of the ether bond was linked to lower plasma powers and pulsed plasma systems, due to the lesser degree of fragmentation of the precursors. [107] Not all studies assess the stability of the coatings. Stable coatings obtained by Brétagnol *et al.* show 95% of reduction of bovine serum albumin attachment as compared to the reference. Most studies used a low pressure plasma set-up, but an example of a dielectric barrier atmospheric pressure plasma set-up is also reported. [107] No studies are conducted to test the stability of these coatings in oxidative environments, as was performed by Konradi *et al.* for PEG brushes. [70]

3.2.2 Plasma polymerization of *N*-vinylpyrrolidone and hydroxy-functional acrylates

The plasma polymerization process of *N*-vinylpyrrolidone and hydroxy-functional acrylates has not been researched extensively. There are a couple of studies, but the main focus is not on the possible non-fouling capacity of the plasma coating. Studies of Andersen *et al.* and Kamath *et al.* synthesized plasma polymerized vinylpyrrolidone coatings that could not resist respectively complement protein attachment or platelet activation. [113], [114] A study by Cökeliler *et al.* of a plasma polymerization process of 2-hydroxyethylmethacrylate showed a reduction of 62.3% in *staphylococcus epidermidis* attachment. [115] It should be noted that no assessment of the stability is performed for this coatings.

3.2.3 Plasma polymerization 2-oxazolines

Two commercially available 2-oxazoline monomers, 2-methyl-2-oxazoline and 2-ethyl-2-oxazoline, are used as a plasma precursor. The research group of the Future Industries Institute of the University of South Australia has used both monomers to create plasma polymerized films. [88], [89], [116] Bhatt *et al.* and Zanini *et al.* used only 2-ethyl-2-oxazoline. [117], [118] All these studies used a low pressure plasma system with various plasma sources. Two papers discuss the non-fouling character of these coatings. Cavallaro *et al.* discussed the adhesion of *S. epidermidis* after overnight incubation. [116] Bhatt *et al.* assessed the

adhesion of human ovarian carcinoma cells for 24, 48 and 96 hours. [117] Both studies conclude that there is non-fouling behaviour. A maximal relative decrease in surface coverage for *S. epidermidis* to 33.6% is obtained for a stable coating. Cell repelling effects on the human ovarian carcinoma cells were observed for a couple of conditions after 96 hours but not after 24 and 48 hours, which is a remarkable result. Stability tests indicate that this result can most likely be attributed to the loss of coating that detaches cells with it.

The coatings show to have a complex chemistry consisting of amide, amine, imine, nitrile, alkyne, isocyanate and carboxyl functional group. [89] The retention of the oxazoline monomer structure could not be derived from this elemental studies, according to the authors. However, they postulated that there is retention of the oxazoline ring structure because of the ability of the coating to covalently bind to the carboxylic acid function of poly(acrylic acid) and COOH-functionalized gold nanoparticles. [89], [118] This also allows the binding of the coatings with proteins. It should however be noted that an oxazoline-ring is not the only functional group that is reactive towards carboxylic acid groups.

3.3 Strategic approach for synthesis of non-fouling coating in this research

Aforementioned results of plasma polymerization for non-fouling purposes are promising but show possibilities for improvement. Therefore, a next step in the synthesis of non-fouling coatings will be examined in this thesis. The first option that needs consideration is the plasma polymerization of a zwitterionic-like coating. However, it would be impossible to synthesize a charge neutral coating via the random process of plasma polymerization of a zwitterionic precursor. As a second option, the synthesis of a peptido-mimetic coating seems to be favorable over PEG-like coatings: PAOx have proven a greater stability in oxidative environments than PEG and poly(peptoids) have shown great stability and resistance to proteolytic degradation. In this research, the preference is going to 2-oxazolines as precursors because of the following reasons:

1. The aforementioned studies, described in section 3.2.3, indicate high amide functionality of the plasma polymer and a non-fouling effect. A cross-linked peptido-mimetic coating is expected to

have good stability. The non-fouling effect can be improved by modifying cell-interactive functionalities like amines.

2. A large variation exist in the side chain on the 2-position of 2-oxazolines. The different synthesis methods to obtain 2-oxazolines with varying R-group are discussed in section 3.4. This structural variation enables a study of the influence of the side chain on the plasma polymerization process, the composition of the coating and the non-fouling effect.

3. The reactivity of the coating as described in section 3.2.3 makes the coating interesting for functionalization. This can be used to immobilize RGD-peptides among others on the coatings. The relevance of this strategy is explained in section 2.2.1.

3.4 Synthesis of 2-oxazolines

2-oxazolines are 5-membered cyclic imino ethers. [119] The number 2 signifies the position of the double bond in the ring structure, as shown in figure 3.3. [120] The cationic ring-opening polymerization (CROP) of 2-substituted-2-oxazolines has gained more interest in comparison with the CROP of chiral 4- and 5-substituted-2-oxazolines, because of their slower polymerization. In this thesis, 2-substituted-2-oxazolines are used for plasma polymerization. In the following sections, three synthesis methods for these monomers are described.

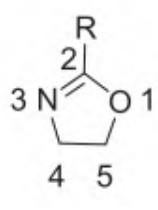

Figure 3.3: Numbering of a 2-oxazoline with R=H, aryl or alkyl. [120]

3.4.1 Direct synthesis of 2-oxazolines via non-activated carboxyl acids

This synthesis procedure is industrially applied for the synthesis of 2-oxazolines. It is a one-pot two-step protocol consisting of the direct condensation of carboxylic acids and 2-ethanolamine and the dehydration of the formed amide (fig. 3.4). [120] The first step is performed at

~170℃, while the second step is catalyzed by a Lewis acid catalyst at an elevated temperature and under reduced pressure. Due to the high temperature requirements, this process is rarely used on lab scale.

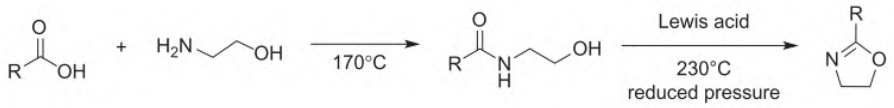

Figure 3.4: Direct synthesis of 2-oxazolines via non-activated carboxyl acids. [120]

3.4.2 Witte-Seeliger synthesis of 2-oxazolines from nitriles

The Witte-Seeliger synthesis is more applicable on laboratory scale. It is a one-step method that proceeds through a reaction between a nitrile and 2-ethanolamine. The reaction is catalyzed by a moderate Lewis acid, such as zinc acetate or cadmium acetate, to activate the nitrile function. The reaction results in the release of ammonia, which interferes with the CROP leading to termination and is reactive towards ester groups among others.

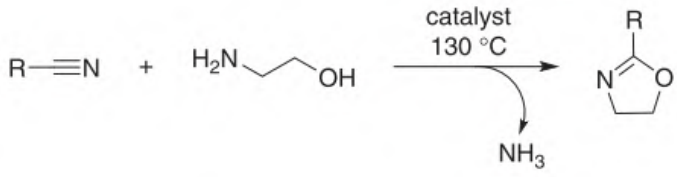

Figure 3.5: The Witte-Seeliger reaction for synthesis of 2-oxazolines. [120]

3.4.3 Modified Wenker method via cyclization of β-haloamides

The modified Wenker method is a milder method than the previous two because the reaction can occur at room temperature. There are two routes to obtain a N-chloroethylamide, which is then treated with a base which leads to ring closure. This results in the formation of the corresponding 2-oxazoline. The first route is the treatment of an acid chloride with 2-chloroethyl amine hydrochloride. The second route is the treatment of an acid chloride with ethanolamine, resulting in the formation of a similar amide as in the direct method described in

section 3.4.1. This amide is then converted into N-chloroethylamide with thionylchloride.

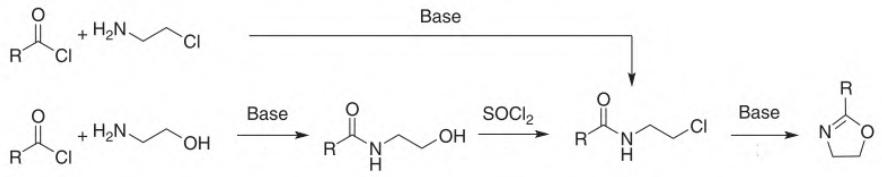

Figure 3.6: Modified Wenker method for synthesis of 2-oxazolines. [120]

3.4.4 α-deprotonation of 2-methyl-2-oxazoline

This mechanism uses commercially available 2-methyl-2-oxazolines and deprotonates the molecule, followed by a nucleophilic substitution with an alkylbromide. There are two alternatives for the deprotonation step: the use of lithium diisopropylamine (LDA) or tetramethylethylenediamine (TMEDA) and *n*-butyllithium (n-BuLi).

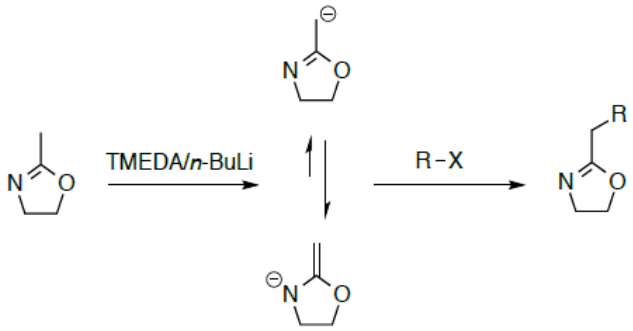

Figure 3.7: α-deprotonation of 2-methyl-2-oxazoline for synthesis of 2-oxazolines. [121]

3.5 Goal of this research

The main objective of this thesis is obtaining stable coatings from different plasma polymerized 2-oxazoline monomers and study the non-fouling behavior by cell tests and bacterial adhesion tests. Besides the use of previously tested and commercially available monomers (2-methyl-2-oxazoline and 2-ethyl-2-oxazoline), three other precursors will be plasma polymerized, which are not reported in literature yet. These

monomers are shown in table 3.2. By comparing the different monomers and varying the plasma polymerization power, the influence of the monomer side chain and plasma power on the coating characteristics will be investigated.

Table 3.2: 2-oxazoline plasma precursors used in this thesis.

2-methyl-2-oxazoline	2-ethyl-2-oxazoline	2-*n*-propyl-2-oxazoline	2-*n*-butyl-2-oxazoline	methyl 3-(2-oxazoline-2-yl) propanoate.
	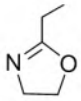	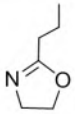	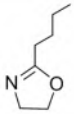	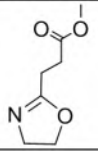

By comparing the plasma polymerization of the first four monomers in table 3.2, the differences in stability, wettability, chemical composition, deposition speed and non-fouling capacity of the deposited coatings for a growing aliphatic side chain will be investigated. By comparing the fifth monomer in table 3.2 with the previous monomers, the influence of an extra hydrophilic functionality in the side chain on the stability, wettability and chemical composition of the plasma polymerized coatings will be studied.

The plasma polymerization process is performed by using a medium pressure dielectric barrier discharge. This is also not reported in literature for 2-oxazoline monomers, as only low pressure plasma sources are used. This provides a faster deposition of the coatings and enables the extensiveness of this study within its duration. Comparing the plasma polymerization of different 2-oxazoline monomers can also give additional information on involved processes.

Chapter 4

Influence of aliphatic side chain length on the plasma polymerization of 2-oxazolines

4.1 2-oxazoline monomer synthesis

In this chapter, the plasma polymerization of the first four monomers in table 3.2 is discussed. The first two monomers, 2-methyl-2-oxazoline (MeOx) and 2-ethyl-2-oxazoline (EtOx), were acquired commercially. The third monomer, 2-*n*-propyl-2-oxazoline (PrOx), was synthesized within this thesis. In order to distribute the workload, the synthesis of 2-*n*-butyl-2-oxazoline (BuOx) was distributed within Supramolecular Chemistry group. Both monomers are synthesized via the Witte Seeliger method.

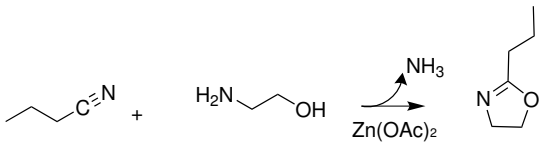

Figure 4.1: Synthesis of 2-*n*-propyl-2-oxazoline via the Witte Seeliger method.

For PrOx, the corresponding nitrile is commercially available. Butyronitrile (1 eq.) and ethanolamine (1.1 eq.) are mixed together, while zinc acetate is added in catalytic amounts (0.02 eq.). The solution is refluxed

for three days at 130°C. By leaving the reflux condenser open to air, the formed ammonia can escape. Ammonia needs to be removed because of its nucleophilic character. It interferes with the CROP of the monomer and the aim is to investigate the plasma polymerization process of 2-oxazolines and reduce the influence of nucleophiles in this process. During the synthesis process, a color change is observed from yellow to red and finally to black because of the oxidation of ethanolamine at high temperatures. After the reaction, two fractional distillations are performed. The first fractional distillation is performed to obtain the product from the residual mixture. The second distillation is performed to remove water and ammonia. A yield of 54% is obtained after these distillations and the formation of the product is confirmed with proton nuclear magnetic resonance (^{1}H-NMR) and liquid chromatography–mass spectrometry (LC-MS). A SEC measurement of a test polymerization resulted in a polydispersity index (PDI) that indicated the presence of nucleophilic residues in the product. Due to the parallel program with the plasma polymerization process, a further purification step was distributed within the Supramolecular Chemistry group. For a complete description of the monomer synthesis, the reader is referred to appendix A. BuOx synthesis follows the same synthesis strategy, but butyronitrile was replaced by valeronitrile (Sigma-Aldrich).

4.2 Electrical characterization of the discharge

The electrical characterization of the discharge is performed as described in section B.3. An example of the pulsed discharge voltage and the resulting current used for plasma polymerization of the different 2-oxazoline monomers is given in figure 4.2.

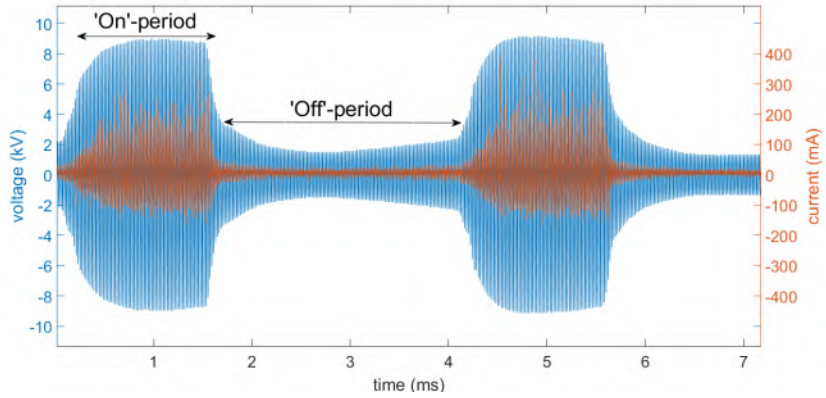

Figure 4.2: Example of discharge voltage and current waveforms at high power (P_{avg}=46.8 W).

A pulsed voltage is used consisting of an 'on'- and 'off' period, as illustrated in figure 4.2. During the 'on'-period, a high voltage is applied to the electrodes, leading to a high current. During the 'off'-period, a lower voltage is applied to the electrodes, leading to a low current. Typically, a pulsed plasma system employs an 'off'-period in which no power is supplied to the plasma. In this thesis, this is not the case due to the nature of the used voltage source. Thereby, a small amount of power is supplied during the 'off'-period. The choice for a pulsed power supply was based on measurements with plasma-polymerized 2-ethyl-2-oxazoline (pPEtOx) prior to this thesis: at powers where the coating was stable, significant heating of the electrode was observed. By using a pulsed power supply, the heating of the electrode can be reduced and lower monomer fragmentation can be obtained as discussed in section 3.1.2.3.

In figure 4.3, a more detailed representation is shown of the discharge voltage and current waveforms during an 'on'-period. The voltage has a sinusoidal form, while the discharge current is a superposition of a sinusoidal waveform and several small current peaks. This indicates that the DBD set-up is operating as a pseudo-glow discharge, which is desirable, as it leads to homogeneous plasma treatment of the sample. [122] This is representative for all applied voltages.

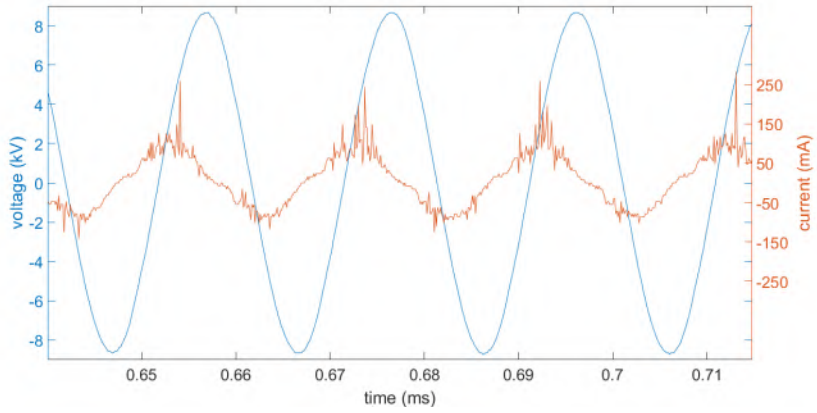

Figure 4.3: Detail of discharge voltage and current waveforms during 'on'-period (P_{avg}=46.8 W).

The 'on'- and 'off'-period is fixed and the voltage applied by the source is varied. This results in varying discharge powers during the 'on'-period and thus varying average discharge powers. However, several uncontrolled variabilities in the applied voltages were observed during the course of this thesis. These have been listed below:

1. Variation in the observed duty cycle for different monomers due to pulse generator manipulations.

2. By lowering the discharge voltage during the 'on'-period, the discharge voltage during the 'off'-period increases. This leads to a variation in the power during the 'off'-period. This power ranges from $\pm$ 2 W at P_{avg}=52.3 W to $\pm$ 4.5 W at P_{avg}=12.3 W. Reducing the discharge voltage even more, results in an almost continuous applied power.

3. By lowering the discharge voltage during the 'on'-period, it becomes less stable: the magnitude of the voltage peaks is not as constant as shown in figure 4.2.

In figure 4.4, a discharge voltage and current waveform is displayed for a lower discharge power, illustrating the above-mentioned points 2 and 3. As this variation in the applied voltage pulse is reoccurring for all monomers this will have little influence on the results.

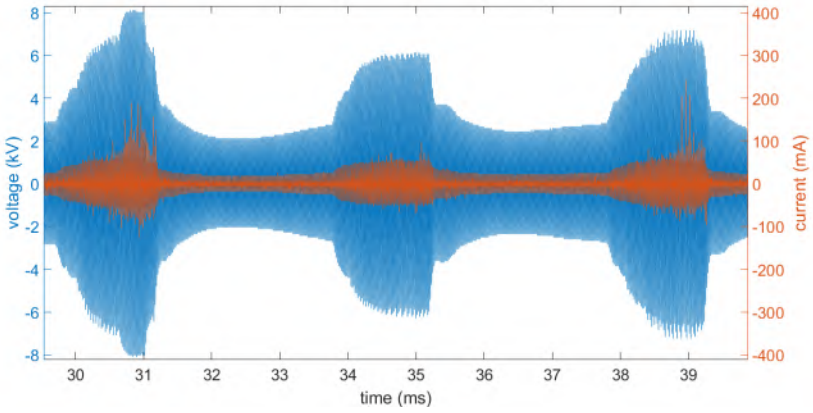

Figure 4.4: Example of discharge voltage and current waveforms at lower power (P_{avg}=13.0 W).

The difference in duty cycle between ppEtox and the other monomers is shown in table 4.1, illustrating the above-mentioned points 1. This may have an influence on the results and additional attention needs to be given to compare the data of pPEtOx and the other monomers.

Table 4.1: Assessment of difference in duty cycle for different monomers.

monomer	'on'-period (ms)	'off'-period (ms)	Duty cycle (%)
ppMeOx ppPrOx ppBuOx	1.548 ± 0.030	2.471 ± 0.033	62.6
ppEtOx	1.329 ± 0.040	2.435 ± 0.040	54.6

4.3 Water contact angle measurements

When performing initial water contact angle (WCA) measurements, it was clear that the WCA values varied considerably over the sample surface. To illustrate this, the sample surface is divided in 9 equal parts of 1 x 1 cm^2, as presented in figure B.4 in appendix B.

Table 4.2: Varying WCA for pPMeOx and pPPrOx at three different powers. pPEtOx and pPBuOx follow a similar trend as the pPPrOx.

pPPrOx 47.7 W		
52.2	56.4	57.1
56.3	56.6	56.4
55.9	55.7	57.2

pPPrOx 24.2 W		
18.8	22.3	56.5
18.2	27.9	55.7
33	25.7	57.8

pPPrOx 9.9 W		
13.5	28.8	45.7
16.5	35.4	48.1
23.5	31.5	35.7

pPPrOx 48.8 W		
<10	<10	49.7
<10	14.8	48.9
<10	<10	49.2

pPPrOx 27.2 W		
<10	12.1	14.4
<10	11.4	51.5
<10	<10	38.3

pPPrOx 12.9 W		
<10	<10	11.5
<10	<10	11
<10	11.7	12.5

As shown in table 4.2, a distinction is observed in the varying WCA over the sample surface for pPMeOx and the other monomers. For pPMeOx, the WCA on the right side of the samples vary from low values at low powers (around 10° at 11.9 W), to higher values at higher powers (around 50° at 48.8 W), while on the right side, the WCA remain low for all powers. Just two different kinds of values for the WCA are obtained for this monomer: low WCA (<15°) and high WCA (± 50°). The WCA of 38.3° is obtained by averaging over low and high WCA. The other monomers show resemblance with the result of pPPrOx in table 4.2: for high powers, the WCA are comparable over the total surface area. Lowering the power results in WCAs that decrease, which occurs first at the left side of the sample. For these monomers, also a wider range of measured WCA is obtained. For pPEtOx and pPPrOx, several values ranging from 10° to ± 54° or ± 57° for the respective monomers were measured. For pBuOx, all WCA ranged from 40° to ± 59°. The inhomogeneity of the WCA over the sample indicates that different plasma conditions are present in the reactor, which results in an inhomogeneous coating composition over the sample surface.

Despite the differences in between pPMeOx and the other monomers, a similarity is observed between all monomers: by increasing the power, the WCAs at the right side of the sample increase to a stable value. By increasing the power even further, comparable WCA are measured at other areas of the sample surface for pPEtOx, pPPrOx and pPBuOx. As already indicated, the WCA at other areas remain low for pPMeOx (<15°). The WCAs at the right side of the sample are taken as the reference and a more detailed study of these WCAs in function of the applied power is performed. These results are shown in figure 4.5.

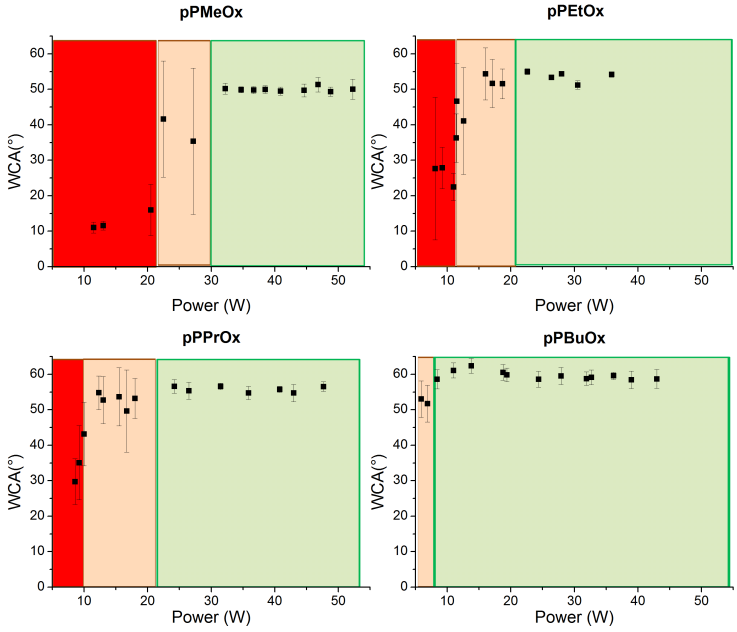

Figure 4.5: WCA for pPMeOx, pPEtOx, pPPrOx and pPBuOx as a function of discharge power. The colors demarcate three different zones in each graph (green: 'stable', orange: 'metastable' and red: 'unstable'). At least 8 measurements are conducted on the right side of each sample.

Figure 4.5 shows three different regimes for the WCAs for each monomer. In the first regime (at high powers, green area in figure 4.5), the WCAs are comparable at the right side of the sample, resulting in small standard deviations. In the second regime (at intermediate powers, orange area in figure 4.5), some WCAs at the right side of the sample are still comparable with the WCAs of the first regime, but lower WCAs are measured as well, which results in larger standard deviations. For pPMeOx, these values are smaller than 15°, resulting in a significant drop of the average contact angle. In the third regime (at low powers, red area in figure 4.5), no WCAs are comparable with the WCA of the first regime. For pPMeOx, small standard deviations are obtained in this area, because only values smaller than 15° were measured. For pPEtOx and pPrOx, larger standard deviation are obtained, as a variety of WCAs is measured. Comparing the WCAs for these two monomers in regime 3 is difficult because of the limited amount of measurements and the large standard deviation. For pPBuOx, the WCAs of the right side of the sample still contain WCAs comparable with the first regime at the lowest power. Therefore, pPBuOx has no measurements in regime

3.

Despite a lack of data in the transition zones between the regimes, a clear trend is observed: the borders of regime 1 and 2 shifts towards lower powers with a growing aliphatic side chain. No clear distinction can be made between pPEtOx and pPPrOx. This can probably be attributed to the difference in duty cycle for pPEtOx: the on-period mostly contributes for the P_{avg} at the boundary limit power and it is expected that this period mostly determines the composition of the coating. As the on-period is shorter for pPEtOx, the power during this peak will be higher compared to the peak power during the on-period for pPPrOx at the same P_{avg}. Therefore, the boundary limit of regime 1 would be at a higher peak power for pPEtOx than for pPPrOx, further indicating the observed trend. However, further measurements would be needed to confirm this hypothesis.

It is a remarkable result that the WCA is constant in regime 1. This indicates that a similar coating composition is obtained at a wide range of different applied powers for these monomers. As illustrated in table 4.2, the WCA at other regions of the sample also go towards these constant value. This means that increasing the power keeps the WCA at the right side of the sample constant, while other areas start experiencing plasma conditions that also result in these values of WCAs. For pPMeOx, the plasma conditions at these areas are not sufficient to obtain the same coating composition over the total surface. Further, a clear trend is observed towards higher WCAs for the growing aliphatic side chain of the monomers in this regime. This is a result of an increased carbon content in the plasma coating for the growing aliphatic side chain, as also illustrated with XPS in section 4.5.2.1.

4.4 Coating stability

The stability assessment of the coating is shown in figures 4.6 and 4.7.

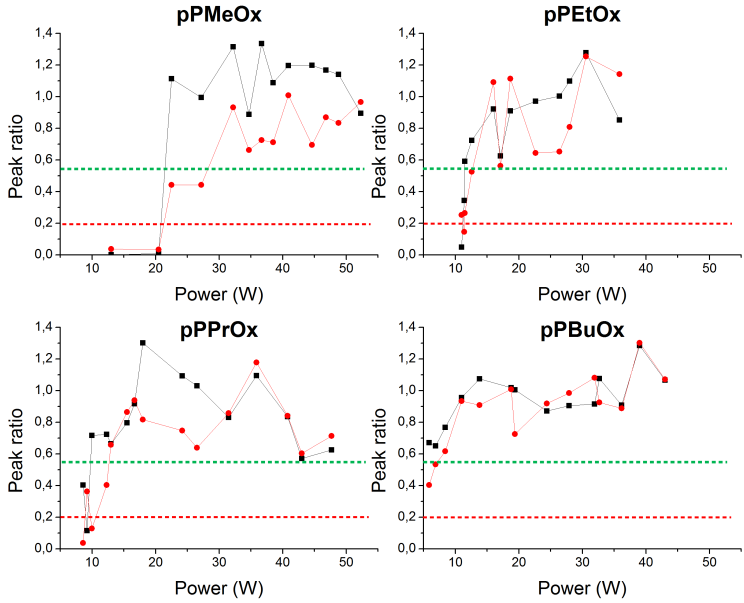

Figure 4.6: Ratio of the area of characteristic coating peak (scaled to substrate peak) for 3 (black) and 7 (red) days on the characteristic coating peak (scaled to substrate peak) for 0 days. Areas are calculated with integration method 1 as discussed in section B.5. Three regimes are distinguished: 'stable' (above the green dotted line), 'metastable' (in between the dotted lines), 'unstable' (under the red dotted line).

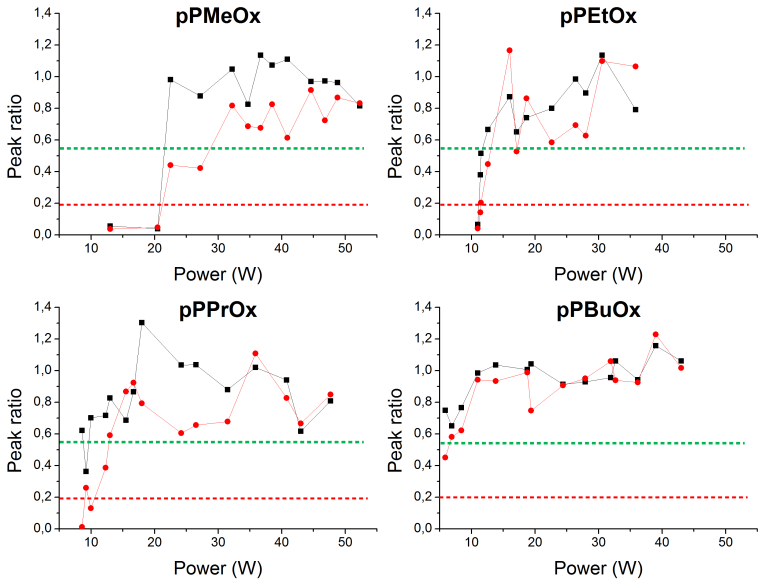

Figure 4.7: Ratio of the area of characteristic coating peak (scaled to substrate peak) for 3 (black) and 7 (red) days on the characteristic coating peak (scaled to substrate peak) for 0 days. Areas are calculated with integration method 2 as discussed in section B.5. Three regimes are distinguished: 'stable' (above the green dotted line), 'metastable' (in between the dotted lines), 'unstable' (under the red dotted line).

The results of both integration strategies are very similar. This means that peak shifts are negligible or have no influence on the outcome of the integration method. Theoretically, a stable coating will result in the same intensity for all peaks, giving the same ratio of the characteristic coating peak to the carbon peak from the ultra-high-molecular-weight polyethylene (UHMWPE) backing, the polypropylene (PP) substrate and the coating for 0, 3 and 7 days in water. This would give a peak ratio, as shown in figure 4.6 and 4.7, equal to 1. When the coating thickness decreases, the decrease in characteristic peak intensity will be larger than the decrease in carbon peak intensity, giving a peak ratio lower than 1.

Several variables influence the Fourier transform infrared spectroscopy (FT-IR) measurement and it is needed to take them into account:

1. The FT-IR measurements for pPMeOx and pPEtOx were conducted on several days: measurements for 0 and 3 days of incubation in deionized water, were measured on the same day,

the measurement for 7 days was conducted on another day. For pPPrOx and pPBuOx, these measurements were conducted on the same day. This may explain why the peak ratios are closer to each for these monomers at high powers. Further analysis (thickness measurements) is needed to confirm this.

2. The thickness varies over the sample surface, as indicated in section 4.6.

3. The measurement for 0 days is always performed on the part of the sample that is closest to the suction point. As indicated in section 4.6, the overall deposition is higher than for the rest of the sample.

4. The handle for fixating the sample will not be turned as hard for each measurement. This can result in variations in compression of the coating, the UHMWPE backing and/or the PP substrate. This can influence FT-IR peak intensities.

5. The broad peak at 3500-3000 cm^{-1} overlaps partially with the carbon peak. The intensity of this peak therefore influences that measurement.

6. Hydrolysis of the coating can result in a decrease in intensity for the specific coating peak.

These variables make this stability assessment a qualitative technique. To compare between monomers, a boundary for the peak ratio is chosen by studying the data.

Both figures show large deviations within the measurements. The most divergent results are:

1. The value of 1.33 at 36.7 W for pPMeOx after 3 days in water, which would theoretically mean that the coating is thicker after water incubation. This can be caused by point 1, 2, 4 and/or 5 of the above-mentioned enumeration. This cannot be caused by swelling of the coating, because the samples are incubated in vacuum before the measurement.

2. The value of 0.57 at 43 W for pPPrOx after 3 days in water, which was confirmed by repeated measurements. This matches with a thickness decrease at high power, while at lower powers, more stable coatings are obtained. This can be caused by point

2, 3, 4 and/or 5 of the above-mentioned enumeration or because of instability of part of the coating. It is difficult to know which caused the obtained peak ratio.

Ratios smaller than 1, as well as ratios larger than 1, can be explained by means of the influencing variables and it is impossible to know the cause of the smaller peak ratios: is it really coating loss or is it caused by an influencing variable. By comparing the results of the stability assessment and the results of the WCA measurement, which is performed on the same samples, a relation can be distinguished. For pPMeOx, this relation is most clear. In regime 1, which will be described as the 'stable' region, the peak ratios vary but remain all above 0.6. The peak ratios in regime 2, which will be described as the 'metastable' region, decrease to $\pm$ 0.4 for 7 days of water incubation; a value never reached in regime 1. In regime 3, which will be described as the 'unstable' region, this ratio decreases to values below 0.1. This demarcation between values above 0.6, around 0.4 and under 0.2 is also shown in figure 4.6 and 4.7. For pPEtOx and pPPrOx, the plasma conditions in regime 3, also result in peak ratios below 0.2 for at least 3 or 7 days of water incubation and all plasma conditions in regime 1 have peak ratios above 0.55. The relation between regime 2 and the intermediate peak ratios is however less clear for these monomers: higher peak ratios are obtained in comparison with pPMeOx. This can be explained by the presence of WCA values that are comparable to regime 1, which results in peak ratios comparable to values of regime 1. For pPBuOx, the plasma conditions in regime 2 result in peak ratios below 0.55.

Based on the aforementioned reasoning, the three stability regimes are defined based on WCA measurements and the stability assessment. These stability regimes are also shown in figure 4.5:

1. 'Stable' coatings: if the WCAs of the plasma-polymerized 2-oxazoline coatings (plasmOx-coatings) reach a stable value (which is different for each monomer as illustrated in figure 4.5) over a total surface area, the peak ratio will never drop below 0.55. This value is chosen, based on the lowest peak ratios of pPPrOx and the peak ratio of pPBuOx in regime 2 on figure 4.5. 'Stable' does not refer to a coating that does not lose any of its thickness. This cannot be concluded out of the used stability assessment. 'Stable' refers to a coating that still has a considerable FT-IR signal at the specific coating peak (at least a peak ratio of 0.55) after seven days of incubation in deionized water. This is also shown in figure

4.8, where the FT-IR measurements of pPPrOx at P_{avg}=43 W for 0, 3 and 7 days of water incubation are presented.

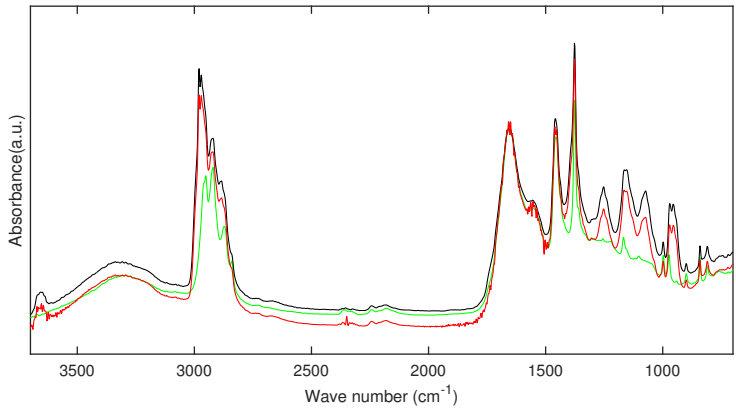

Figure 4.8: FT-IR measurements of pPPrOx at P_{avg}=43 W for 0 (green) for 3 (black) and 7 (red) days of water incubation. For 3 days of water incubation, peak ratios of 0.57 (method 1) and 0.62 (method 2) are obtained. For 7 days of water incubation, peak ratios of 0.60 (method 1) and 0.67 (method 2) are obtained.

2. 'Metastable' coatings: the WCAs of the plasmOx-coating over a total surface area are composed of a mixture of both high WCAs (corresponding with stable values of regime 1) and low WCAs. A considerable FT-IR signal at the specific coating peak cannot be expected anymore after water incubation, but its presence is still a posibility. However, an FT-IR signal at the specific coating peak will be present to a lesser extent, indicating still a presence of coating after 7 days of water incubation. At peak ratios between 0.2 and 0.55, loss of coating thickness is highly plausible.

3. 'Unstable' coatings: the WCAs of the plasmOx-coating over a total surface area are composed of considerably lower WCAs than in regime 1. Incubation in water of these samples will lead to a considerably lower FT-IR signal at the specific coating peak. A significant amount of the coating is lost. A peak ratio lower than 0.2 was measured for these coatings.

To illustrate the peak ratios related to 'metastable' and 'unstable' coatings, the FT-IR measurements of pPEtOx at P_{avg}=11.4 W for 0, 3 and 7 days of water incubation are presented in figure 4.9.

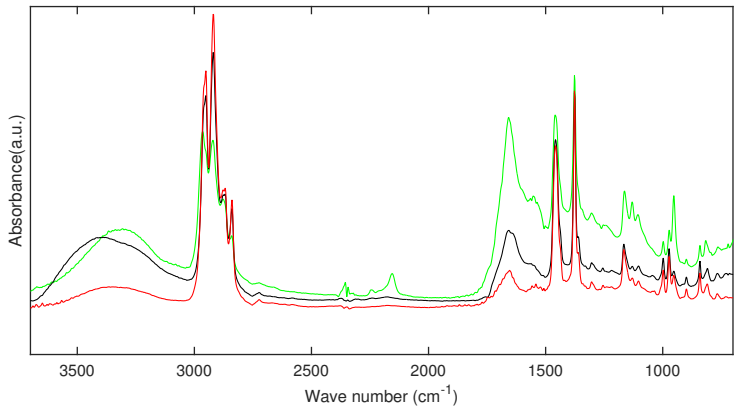

Figure 4.9: FT-IR measurements of pPEtOx at P_{avg}=11.4 W for 0 (green) for 3 (black) and 7 (red) days of water incubation. For 3 days of water incubation, peak ratios of 0.34 (method 1) and 0.38 (method 2) are obtained. For 7 days of water incubation, peak ratios of 0.15 (method 1) and 0.14 (method 2) are obtained.

By defining these stability regions, a comparison can be made for the obtained stability of the coating for the different monomers. As described in section 4.3, a shift of the borders 'stable' and 'metastable' regime towards lower powers with a growing aliphatic side chain is observed. This means that a growing aliphatic side chain enables stability at lower powers for the same mass flow. This means that in the conditions of this thesis, a plasmOx coating with a monomer with longer aliphatic side chain will reach stability at lower YF.

It is however also interesting to look at the relation of the stability in function of the following factor: $\frac{W}{M}$, with power W (J/s) and monomer flow rate M (mol/s). Thereby, the stability boundary for the different monomers can be compared for the same molar flow instead of mass flow. The values of the boundary between 'stable' and 'metastable' region for the monomers are shown in table 4.3. The chosen boundaries are approximations, but a trend is still visible. For pPMeOx, the highest value of $\frac{W}{M}$ is obtained. pPEtOx and pPPrOx have a lower value and pPBuOx has the lowest value. For pPEtOx and pPPrOx, the values are deviating, which is possibly caused by the difference in duty cycle. This seems to indicate that even for the same molar flows, a monomer with a longer aliphatic side chain will obtain 'stable' coatings more easily. This is a strong indication that cross-linking via the side chain becomes more easy when this chain is longer.

Table 4.3: Comparison of the factor $\frac{W}{M}$ for the different monomers.

monomer	boundary (W)	$\frac{W}{M}$ $(\frac{W}{mol/h})$
pPMeOx	30	$13 . 10^3$
pPEtOx	21	$10 . 10^3$
pPPrOx	21	$12 . 10^3$
pPBuOx	7	$4 . 10^3$

4.5 Chemical composition

4.5.1 Fourier transform infrared spectroscopy

FT-IR is used as a first analysis technique for the chemical composition of the coating. In figure 4.10, an FT-IR spectrum of a coated PP sample backed with UHMWPE is compared with a bare PP sample with UHMWPE backing.

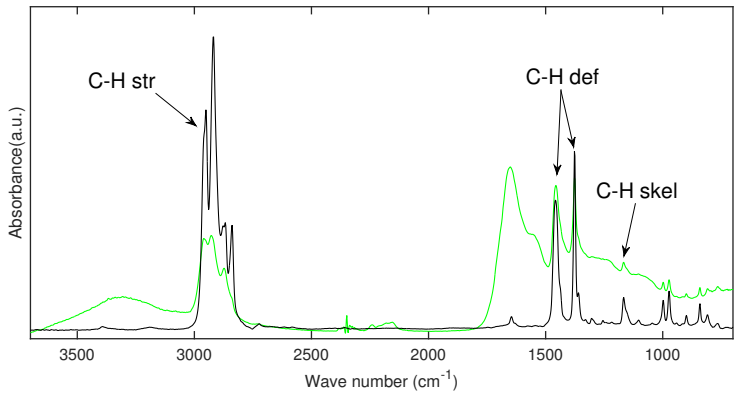

Figure 4.10: FT-IR signal of the PP (substrate) and UHMWPE (backing) (green) and pPEtOx (P_{avg}=35.86 W).

Several peaks of the PP+UHMWPE spectrum are also observed in the signal of the pPEtOx sample. These are indicated with an arrow in figure 4.10. In table 4.4, these peaks are also enlisted with their respective chemical state. In figure 4.11, a spectrum for the different monomers is shown. This figure illustrates that a number of peaks are similar for all monomers, but it indicates also that there are differences: the peak at

1547 cm^{-1} (indicated with the black vertical line) is more pronounced for pPPrOx and pPBuOx. There are also differences in the peak positions at wavenumbers lower than the C-H deformation (C-H def) peak at 1375 cm^{-1} (indicated with the blue vertical line). However, an analysis of the spectra in function of power and monomer did not indicate clear trends in these differences. Therefore, it was also not possible to distinguish the difference in between regions 1, 2 and 3, as defined in section 4.4.

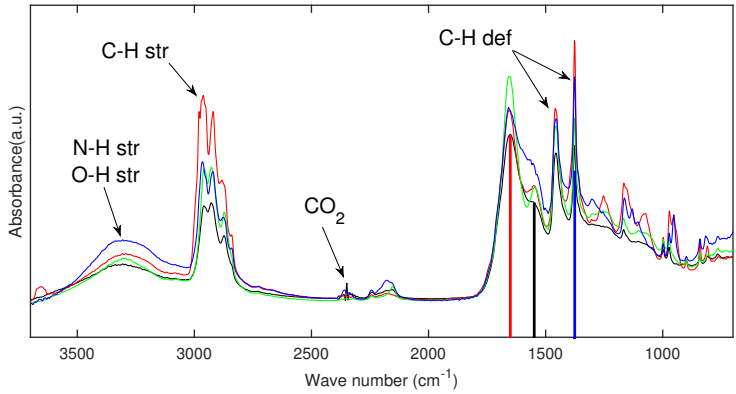

Figure 4.11: FT-IR signal of pPMeOx P_{avg}=34.7 W (blue), pPEtOx P_{avg}=35.9 W (black), pPPrOx P_{avg}=35.9 W (red), pPBuOx P_{avg}=36.2 W (green)

As illustrated in figure 4.11, all coatings have a broad peak between 3500 and 3000 cm^{-1}, which can be assigned to N-H or O-H stretching vibrations. Making a distinction between them is difficult in this case. Several peaks between 3000 and 2800 cm^{-1}can be assigned to C-H stretching vibrations. A detailed description of these peaks is found in table 4.4. All these peaks are related to the PP substrate, the UHMWPE backing and the coating.

Table 4.4: The peaks associated with carbon-hydrogen bonds. All these peaks are related to the PP substrate, the UHMWPE backing and the coating.

Peak location (cm^{-1})	Vibration	Chemical state
2965	C-H stretch	- CH_3 (alihpatic)
2919	C-H stretch	- CH_2 - CH_2 - (acyclic)
2876	C-H stretch	- CH_3 (alihpatic)
2840	C-H stretch	- CH_2 - CH_2 - (acyclic)
1459	C-H deformation (asym)	- CH_3 (alihpatic)
1375	C-H deformation (sym)	- CH_3 (alihpatic)

The broader peak around 2345 cm^{-1} is a consequence of bad CO_2 compensation of the software and is not related to the coating. The small broader peak between 2250 and 2150 cm^{-1} is observed for all different monomers. A detail of this small broad peak is presented in figure 4.12.

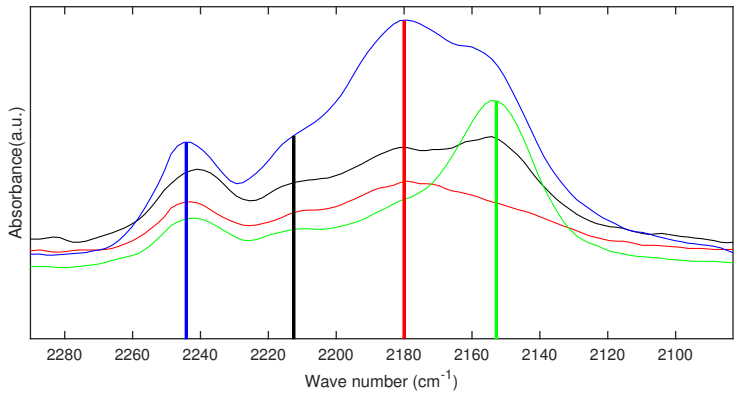

Figure 4.12: Detail of the FT-IR signal of pPMeOx P_{avg}=34.7 W (blue), pPEtOx P_{avg}=35.9 W (black), pPPrOx P_{avg}=35.9 W (red), pPBuOx P_{avg}=36.2 W (green)

There are differences in the shape of this small broad peak for the different monomers, but an analysis in function of power and monomer did not indicate clear trends in these differences. All FTIR-measurements of the coatings resulted in a small broad peak that seemed to be composed of 4 peaks, as indicated in figure 4.12. Assigning these peaks is difficult, because of the unknown plasma process. Possibly, the peaks at 2243

cm^{-1} and 2154 cm^{-1} corresponds to a nitrile (range: 2260-2230 cm^{-1}) and an isonitrile (range: 2175-2130 cm^{-1}) respectively. An additional indication for the presence of the isonitrile, is the disappearance of the respective peak after water incubation, as discussed will be discussed in section 4.5.3. Isonitrile peaks are strong in intensity. The low intensity in the spectra of the plasmOx-coatings, should therefore indicate a low concentration of this group. Further analysis will be needed to confirm the chemical composition corresponding to these peaks, but this lies outside the scope of this thesis.

The peaks at 1656 and 1547 cm^{-1} (respectively the red and black vertical line in figure 4.11) are difficult to assign. The first peak can correspond with a number of different chemical states. A few examples of possibilities are imines (range: 1690-1630 cm^{-1}), iminoethers (this corresponds with the ring structure of a 2-oxazoline; range: 1690-1645 cm^{-1}) or amides (amide I band: 1680-1630 cm^{-1}). The second peak, could correspond with secondary amides (amide II band: 1570-1515 cm^{-1}) for example. Other analysis methods are needed to assign a chemical composition to these peaks.

The peaks at 1459 and 1375 cm^{-1} correspond to C-H deformations. The detailed description is found in table 4.4. The peaks at lower wave numbers than 1375 cm^{-1}, which is indicated with the blue line in figure 4.11, show no consistency in function of power and monomer. Because of the unknown plasma process and the difficult assignment of the most pronounced peaks, no analysis of these peaks is performed.

4.5.2 X-ray photoelectron spectroscopy

As FT-IR could not indicate a difference between the different regimes, XPS is used as an additional technique for the determination of the chemical composition of the coating.

4.5.2.1 Elemental composition

A typical survey scan, as described in section B.4.3, from a plasmOx coating is presented in figure 4.13.

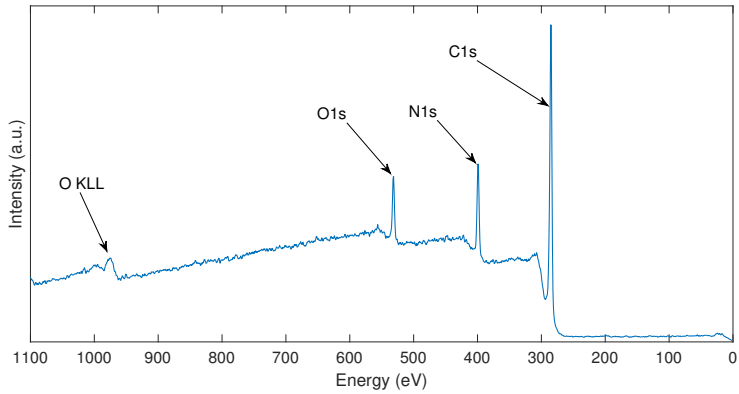

Figure 4.13: A survey scan of pPMeOx at P_{avg}=50.3 W.

This survey scan indicates the presence of C, O and N, which is expected. H is undetectable in XPS, but from FT-IR it is clear that it is present in the coating. From this survey scan, the elemental composition of the coatings is derived. The elemental composition for the plasmOx coatings is expressed in the elemental content. The formula for the example for N is given:

$$Ncontent = \frac{\#_N}{\#_N + \#_O + \#_C} \tag{4.1}$$

$\#_X$ is the amount of atoms of element X in the measured sample. The elemental content is expressed as an atomic concentration (at%), which is the content of C, N or O compared to the total amount of C, N and O. The elemental content of C, N and O in function of the applied power is shown in figures 4.14-4.16. After initial measurements, the choice was made to only assess XPS measurement for coatings in the 'stable' and 'unstable' region. In the 'metastable' region, different WCA are present, indicating a different coating composition. As no WCAs are measured on the XPS-sample to avoid reaction with water, it is unknown which coating composition is present on samples within the 'metastable' region.

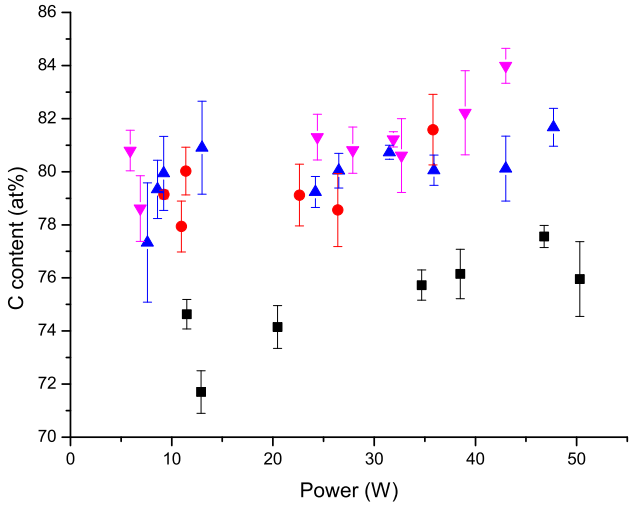

Figure 4.14: The carbon content of the coatings in function of the power. Black: pPMeOx, red: pPEtOx, blue: pPPrOx, purple: pPBuOx

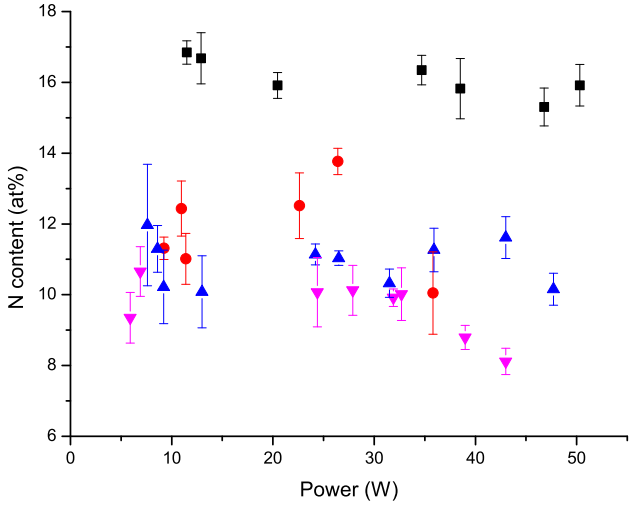

Figure 4.15: The nitrogen content of the coatings in function of the power. Black: pPMeOx, red: pPEtOx, blue: pPPrOx, purple: pPBuOx

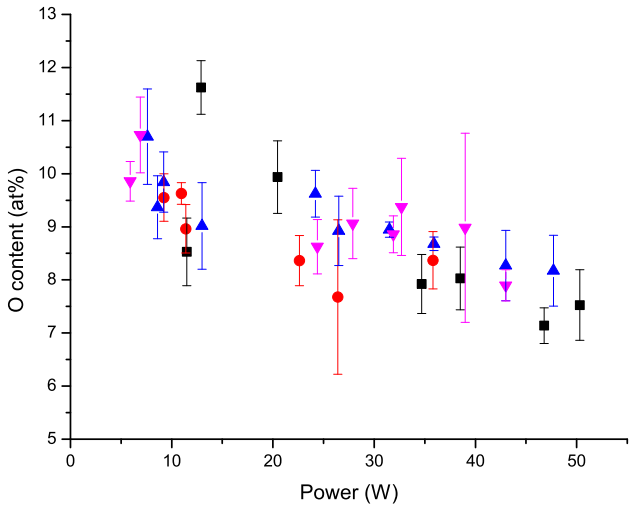

Figure 4.16: The oxygen content of the coatings in function of the power. Black: pPMeOx, red: pPEtOx, blue: pPPrOx, purple: pPBuOx

In figures 4.14-4.16, some trends are visible. To quantify this and give a clear overview, the elemental content of the 'unstable' and 'stable' regimes are averaged. As WCA measurements indicated that the same chemical composition is present in the 'stable' regime, the elemental content should be comparable. As presented in figures 4.14-4.16, this is not completely the case. More XPS-measurements would be needed to confirm if these large deviations are random errors or if there is really a difference in the elemental content for different samples within the stable region. The results for this averaging procedure are shown in table 4.5.

Table 4.5: Overview of the elemental content for the four plasma polymerized monomers. Averages and standard deviations are calculated from all the elemental contents in the corresponding regime. *As there is no 'unstable' region for pPBuOx, values of the 'metastable' region are used.

C content (at%)	pPMeOx	pPEtOx	pPPrOx	pPBuOx
'Stable' region	76.3 ± 1.1	79.8 ± 1.8	80.3 ± 1.1	81.8 ± 1.4
'Unstable' region	73.5 ± 1.5	79.0 ± 1.1	78.3 ± 1.9	79.7 ± 1.5*

N content (at%)	pPMeOx	pPEtOx	pPPrOx	pPBuOx
'Stable' region	15.8 ± 0.7	12.1 ± 1.8	10.7 ± 0.8	9.4 ± 0.9
'Unstable' region	16.5 ± 0.6	11.6 ± 0.9	11.6 ± 1.3	10.0 ± 1.0*

O content (at%)	pPMeOx	pPEtOx	pPPrOx	pPBuOx
'Stable' region	7.7 ± 0.6	8.1 ± 0.9	8.9 ± 0.7	8.8 ± 0.9
'Unstable' region	10.0 ± 1.4	9.4 ± 0.5	10.0 ± 1.0	10.3 ± 0.7*

Despite the variability in the elemental contents, clear trends can be distinguished in table 4.5. For the 'stable' region, the oxygen content does not change significantly, while a decrease in nitrogen content and a corresponding increase in carbon content is noticed. For the 'unstable' region, a significant increase in oxygen content is observed with respect to the 'stable' region. The nitrogen content does not seem to change significantly for 'stable' and 'unstable' regions. The carbon content is significantly lower for pPMeOx at 'unstable' coatings in comparison with the 'stable' coating, as expected by the oxygen content increase. For the other monomers, this change in content is less pronounced.

This may indicate that stability of the coating is obtained by more partitioning of oxygen containing particles. The higher amount of oxygen in the 'unstable' regime can be related to the lower WCAs. In the 'stable' region, the increase of the carbon content can be related to the increasing WCAs in function of a longer aliphatic side chain. A greater increase in carbon content is observed in between pPMeOx and pPEtOx than in between the other monomers. This may be linked to a higher fragmentation of the side chain when this side chain becomes longer.

The elemental contents of the plasmOx-coatings can also be compared with the elemental contents of the monomers shown in table 4.6

Table 4.6: Overview of the theoretically expected elemental contents for the four monomers.

	pPMeOx	pPEtOx	pPrOx	pBuOx
C content (at%)	66.67	71.43	75.0	77.78
N content (at%)	16.67	14.29	12.5	11.11
O content (at%)	16.67	14.29	12.5	11.11

For the 'unstable' region pPMeOx, the nitrogen content is comparable to that of the monomer. For all other monomers, the oxygen and nitrogen content of the plasma polymer are significantly lower than these contents of the monomer. For the 'stable' coating, the nitrogen content of pPMeOx is 94.8% of the nitrogen content of the monomer. For the other 3 monomers, this lies significantly lower at 84.7% for pPEtOx, 86.4% for pPrOx and 85.5% for pPBuOx. As the latter 3 lie close to each other, this might indicate that a similar process is responsible for the partitioning of nitrogen-containing particles in the plasma process for these monomers. Going from pPMeOx to pPBuOx, the carbon and oxygen content of the plasmOx-coatings become more comparable with the values of the monomer. This may be caused by more fragmentation of the side chain when this chain becomes longer. Thereby, the relative amount of oxygen increases. These results give a first implication about the ongoing plasma processes. Further analysis is performed in order to investigate this in more depth.

4.5.2.2 Analysis of high resolution spectra

By studying the high resolution spectra of the coatings, differences in the chemical composition in between monomers and different powers can be assessed. In well-defined structures, deconvolution of the high resolution spectra can give an indication on which chemical states are present. Attempts were made to define peak energy values for deconvolution, based on XPS measurements of reference polymers. This gave however no chemically correct results. Therefore, this section will use the high resolution spectra to make a comparison between 'stable' and 'unstable' coatings and in between the different monomers. First, a visual representation will be presented in figures 4.17-4.18.

By visually comparing the high resolution spectra in the 'stable' region for one monomer, it is observed that there are only very small differences in between the spectra. This is in accordance with the WCA measurement. This is also illustrated in figure 4.17 for pPMeOx,

which is a representative measurement for the other monomers. Visually comparing the spectra between the 'stable' and 'unstable' region for one monomer, indicates that the N1s- and O1s-spectra do not show visible differences. This is also observed for the other monomers. This is illustrated in figure 4.17, where the red dotted line corresponds with spectra of an 'unstable' coating. There is also a broadening of the C1s-peak present for the 'unstable' coating. This is however not representative for all the measurements.

Comparing the high resolution spectra between different monomers at a comparable power in the stable region, indicates that these are similar. This is illustrated in figure 4.18.

Figure 4.18 illustrates that the differences in the O1s-spectra are negligible, while differences in N1s- and C1s-spectra are present. In the N1s-spectrum, a clear shift is observed towards lower peak energies for an increasing aliphatic side chain. This shift is however very small. For the C1s-spectrum, no clear trends are observed, but differences exist in between the monomers. To quantify these differences and obtain a better overview, a peak fit is made for each high resolution spectrum. This enables the search for more detailed trends.

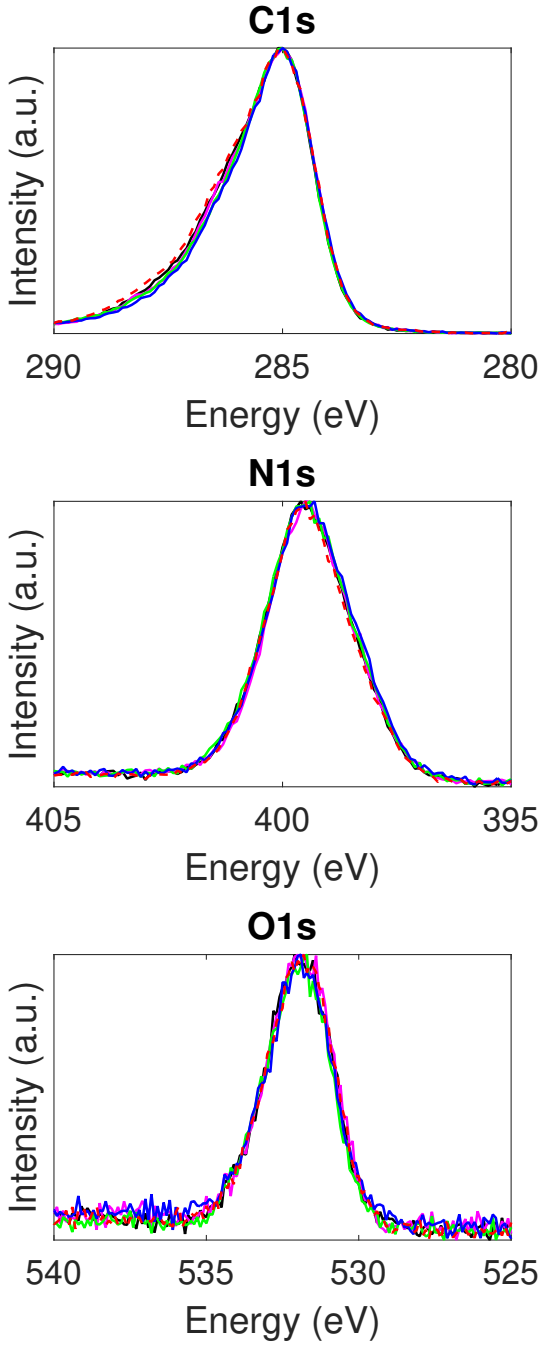

Figure 4.17: C1s, N1s and O1s high resolution spectra for pPMeOx: 50.3 W (blue), 46.8 W (purple), 38.5 W (black), 34.7 W (green) and 20.5 W (red dotted).

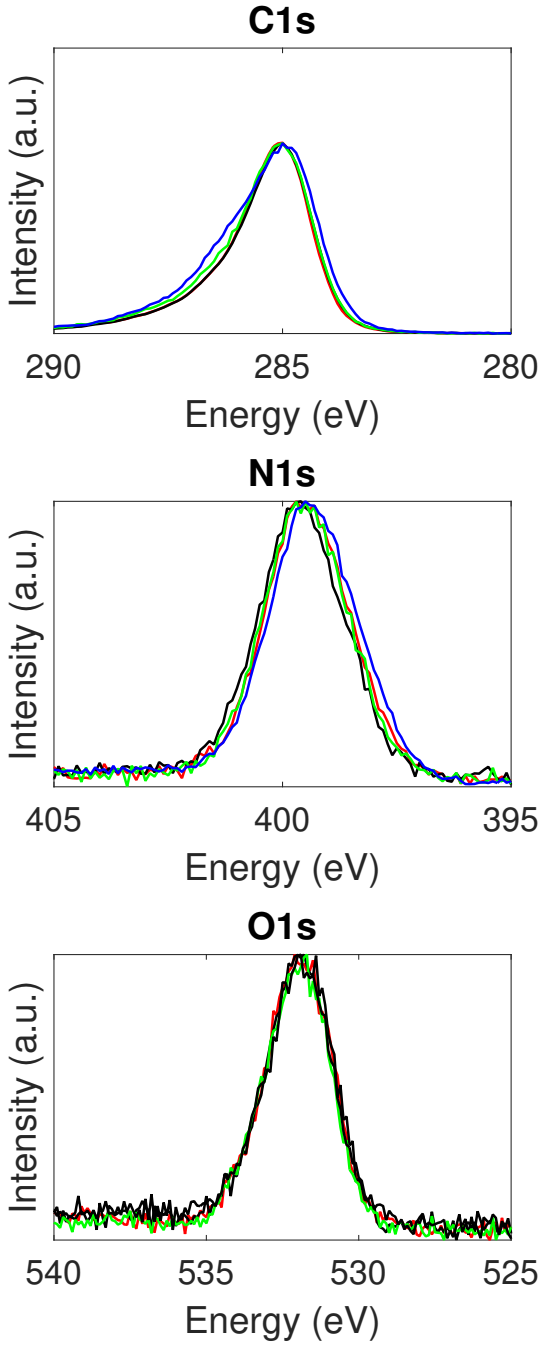

Figure 4.18: C1s, N1s and O1s high resolution spectra for pPMeOx 34.7 W (blue), pPEtOx 35.9 W (red), pPrOx 35.9 W (green) and pPBuOx 32.7 W (black).

C1s

For the C1s-peak, a deconvolution is made with 4 peaks, as described in section B.4.3.

Table 4.7: The areas for each peak 'stable' (green) and 'unstable' (red) region. For both regions, an average is taken of the peak area of all measurements in these region. As there is no 'unstable' region for pPBuOx, values of the 'metastable' region are used.

	pPMeOx	pPEtOx	pPPrOx	pPBuOx
Peak 1 (%)	63.6 ± 1.6	69.6 ± 2.7	70.2 ± 2.4	71.2 ± 2.0
	60.6 ± 3.9	70.3 ± 2.7	69.1 ± 2.8	65.5 ± 2.6
Peak 2 (%)	26.0 ± 1.1	21.0 ± 2.7	20.1 ± 2.6	19.6 ± 1.2
	25.2 ± 5.8	18.9 ± 3.4	19.9 ± 2.3	23.4 ± 1.7
Peak 3 (%)	7.1 ± 1.6	6.6 ± 1.1	7.2 ± 0.9	6.4 ± 0.7
	9.3 ± 3.4	7.8 ± 1.0	8.2 ± 0.8	8.2 ± 0.9
Peak 4 (%)	3.4 ± 0.9	2.8 ± 0.8	2.5 ± 0.6	2.0 ± 0.4
	5.0 ± 2.1	3.0 ± 0.7	2.8 ± 0.7	2.8 ± 0.3

The differences in the areas in between the 'stable' and 'unstable' region are only significant for pPBuOx. There is also no clear trend in the data in between the 'stable' and 'unstable' region. For pPBuOx, a decrease in the area of peak 1 is observed for the 'metastable' coatings, which mostly results in an increase for peak 2 and 3. As peak 1 relates to C-C bonds, this may be an indication that the relative amount of C-C bonds is lower for 'metastable' coatings. [123] In between monomers, there is only a significant difference in between pPMeOx and the other monomers. A lower area for peak 1 is observed for pPMeOx, which relates to a relatively lower amount of C-C bonds for this monomer. This can be expected because of the lower number of carbons in the side chain and it is an affirmation of the observations in figure 4.18. The observation that there were also small differences in between 'stable' and 'unstable' coatings, is not confirmed in table 4.7. This may be because the fitting procedure is not precise enough and that the differences are really small. There are also no significant differences in between the other monomers. This can also be caused by the fitting procedure or it can mean that there are really no differences. This may indicate that a more significant fragmentation of the side chain is occurring for pPPrOx and pPBuOx, resulting in a comparable amount of C-C bonds as in pPEtOx.

N1s

For the N1s-peak, a deconvolution is made with 1 peak. In table 4.8, the peak position and full width at half maximum (FWHM) of the peaks in the 'stable' and 'unstable' region are presented. As WCA and XPS measurements indicate no significant difference in chemical composition in the 'stable' region, the peak position and FWHM are averaged and compared with the averages for the 'unstable' region.

Table 4.8: The peak position (at the top of each column, in eV) and FWHM (at the bottom of each column, in eV) of the fitting for the N1s-spectrum for the 'stable' and 'unstable' region. For both regions, an average is taken of the peak position and FWHM of all measurements in these region. *As there is no 'unstable' region for pPBuOx, values of the 'metastable' region are used.

	N1s	pPMeOx	pPEtOx	pPPrOx	pPBuOx
'Stable'	Peak (eV)	399.38 ± 0.05	399.42 ± 0.06	399.49 ± 0.05	399.51 ± 0.05
region	FWHM (eV)	2.24 ± 0.04	2.22 ± 0.03	2.17 ± 0.03	2.16 ± 0.04
Unstable'	Peak (eV)	399.40 ± 0.05	399.49 ± 0.05	399.52 ± 0.06	399.58 ± 0.10*
region	FWHM (eV)	2.17 ± 0.04	2.15 ± 0.03	2.10 ± 0.03	2.13 ± 0.04*

For 'stable' and 'unstable' region, a very small shift is observed towards higher peak energies for increasing aliphatic side chain length. This shift is equal to the sensitivity of the equipment (0.1 eV). The FWHM seems to be lower for pPPrOx and pPBuOx than for pPMeOx and pPEtOx, but these differences are not significant. Overall, the differences in the N1s-spectra are very small, as illustrated by this peak fit.

O1s

For the O1s-peak, a deconvolution is made with 1 peak. In table 4.8, the peak position and FWHM of the peaks in the 'stable' and 'unstable' region are presented. As WCA and XPS measurements indicate no significant difference in chemical composition in the 'stable' region, the peak position and FWHM are averaged and compared with the averages for the 'unstable' region.

Table 4.9: The peak position (at the top of each column, in eV) and FWHM (at the bottom of each column, in eV) of the fitting for the O1s-spectrum for the 'stable' and 'unstable' region. For both regions, an average is taken of the peak position and FWHM of all measurements in these region. *As there is no 'unstable' region for pPBuOx, values of the 'metastable' region are used.

	O1s	pPMeOx	pPEtOx	pPPrOx	pPBuOx
'Stable'	Peak (eV)	532.01 ± 0.15	532.07 ± 0.14	532.23 ± 0.13	532.26 ± 0.08
region	FWHM (eV)	2.56 ± 0.05	2.59 ± 0.06	2.60 ± 0.06	2.64 ± 0.05
'Unstable'	Peak (eV)	531.87 ± 0.07	531.98 ± 0.07	532.11 ± 0.08	532.22 ± 0.02*
region	FWHM (eV)	2.53 ± 0.07	2.58 ± 0.06	2.57 ± 0.05	2.64 ± 0.07*

For 'stable' and 'unstable' regions, a very small shift is observed towards higher peak energies for increasing aliphatic side chain length. For 'stable' coatings, the peak position lies at a higher energy. These differences are however not significant. This peak fit illustrates that the differences in the O1s-spectra are also very small.

4.5.2.3 Comparison plasmOx with polymers containing tertiary and secondary amides

In the previous section, the differences between the plasmOx-coatings are assessed. It is clear that the differences in the C1s, N1s and O1s-spectra for the different monomers and powers are small, although the elemental composition varies for 'stable' and 'unstable' coatings. As already discussed in section 4.5.2.2, attempts to identify the different chemical structures in the coating did not result in chemically correct results. By comparing the XPS-spectra of the coatings, which are all comparable, with the XPS-spectra of PAOx, the conventional polymerization and plasma polymerization of 2-oxazolines can be compared. Therefore, high resolution spectra are measured for poly-(2-methyl-2-oxazoline) (PMeOx), poly-(2-ethyl-2-oxazoline) (PEtOx), poly-(2-*n*-propyl-2-oxazoline) (PPrOx) and poly-(2-*n*-butyl-2-oxazoline) (PBuOx). These are presented in figure 4.19.

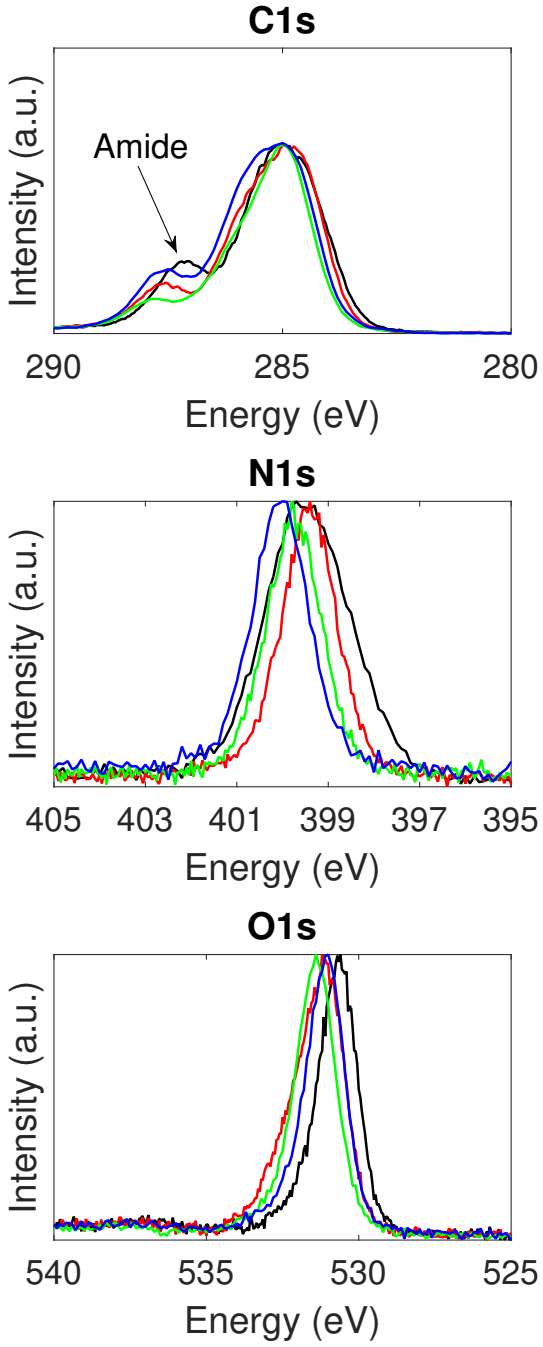

Figure 4.19: High resolution C1s-, N1s- and O1s-spectra from PMeOx (red), PEtOx (black), blue: PPrOx (blue), PBuOx (green).

It is clear that there are differences between the spectra of the different polymers. However, a typical peak is observed in the C1s-spectra that originates from an amide. By observing the elemental contents of C, N and O of these polymers via an XPS survey, it became clear that there were large deviations from the theoretical values. Small amounts of fluor (probably pollution) and sulfur (from the initiator methyl-*p*-toluenesulfonate (MeOTs)) were also measured, but these are not included in the following table:

Table 4.10: Overview of the elemental contents for the four PAOx.

	PMeOx	PEtOx	PPrOx	PBuOx
C content (at%)	73.4±1.1	73.3±0.3	69.5±1.2	75.1±1.2
N content (at%)	10.8±0.4	14.2±0.9	14.5±1.9	7.7±1.2
O content (at%)	15.8±1.3	12.5±0.6	15.4±1.0	14.7±0.4

By comparing these elemental compositions with the expected values of the PAOx, which are the same for the respective monomers as presented in table 4.10, it is observed that only PEtOx and PPrOx have an elemental composition comparable to the expected values. For PMeOx and PBuOx, a higher amount of oxygen in comparison with nitrogen is measured. This may be caused by the presence of pollution of the material. Therefore, a further comparison is made between PEtOx ($\frac{Ccontent}{Ocontent}$ and $\frac{Ccontent}{Ncontent}$ approach the theoretical values more closely than PPrOx) and a plasmOx-coating. To compare the spectra of a plasmOx-coating with a secondary amide too, the spectra of poly-(2-isopropenyl-2-oxazoline) (PIPRO) that is ring-opened with acetic acid (RO-PIPRO, are also included in the comparison. This molecule is shown in figure 4.20.

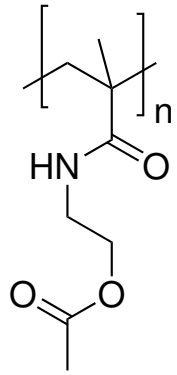

Figure 4.20: Structure of PIPRO that is ring opened with acetic acid.

The elemental contents of this polymer were consistent with the expected values, as illustrated in table 4.11.

Table 4.11: Theoretical and measured elemental contents for RO-PIPRO.

	Survey	Theoretical
C content (at%)	68.4 ± 0.5	66.7
N content (at%)	8.0 ± 0.3	8.3
O content (at%)	23.2 ± 0.3	25

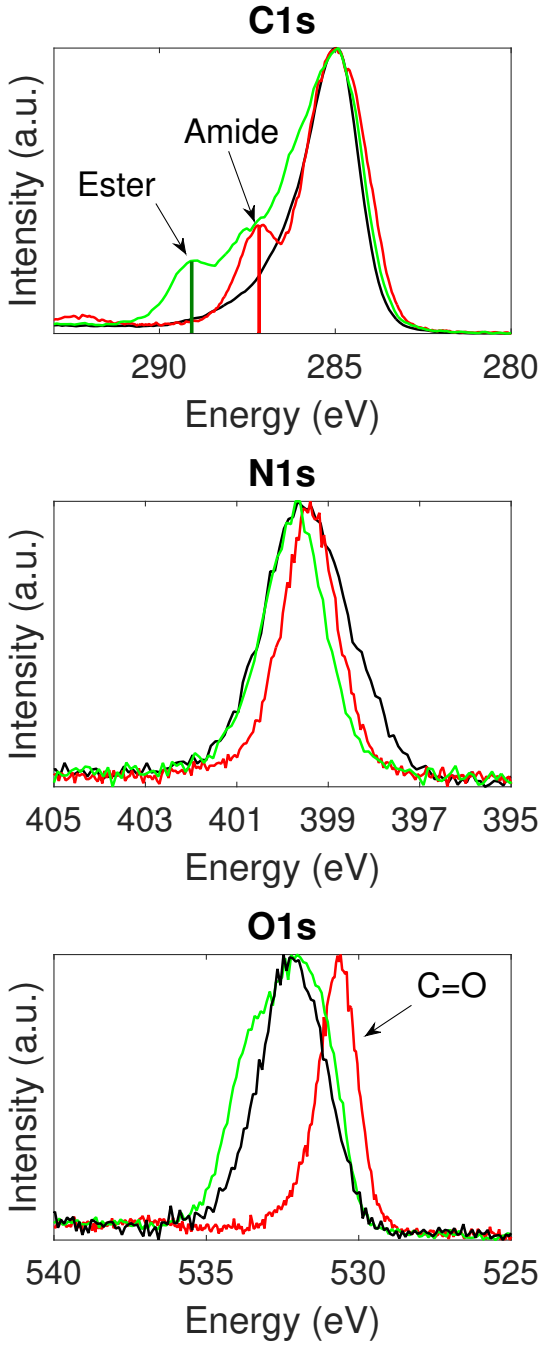

Figure 4.21: High resolution C1s-, N1s- and O1s-spectra from pPEtOx (P_{avg}=35.86 W) (black), PEtOx (red) and ring-opened PIPRO (green).

In figure 4.21, a comparison between the high resolution spectra of a plasmOx-coating and a secondary and tertiary amide-containing polymer is presented. Following things can be observed:

1. C1s: The tertiary amide is clearly visible in the C1s-spectrum. The spectrum of the RO-PIPRO contains an amide signal, and an ester signal at higher energies. The amide signal is however not as clearly pronounced as in the PEtOx. The spectrum of RO-PIPRO is broader than the spectrum of pPEtOx. The spectrum of pPEtOx lacks the presence of such a pronounced amide content.

2. N1s: This peak varies for the RO-PIPRO and PEtOx, indicating that there is a small difference in XPS signal for secondary and tertiary amides. The peak for pPEtOx is broader than the other peaks, indicating the presence of multiple chemical environments in which nitrogen is found in the coating.

3. O1s: This peak is well-defined for PEtOx, while this is not the case for RO-PIPRO. This is caused by multiple chemical environments in which oxygen can be found (ester and amide). A different peak energy will be related to the secondary amide, in comparison with the tertiary amide, as the RO-PIPRO-peak has a small overlap with the PEtOx-peak. The pPEtOx is shifted towards lower energies with respect to the energy associated with the tertiary amide. This relates to a shift towards more single-bounded oxygen. As there is an overlap with the RO-PIPRO-peak, double bounded oxygen may still be present in the coating.

This comparison gives an indication that other processes are involved in the plasma polymerization than in the conventional polymerization. This can be observed in the C1s-spectrum of the coatings, where no pronounced amide peak is present. An extensive formation of tertiary amides can also be excluded on the basis of the O1s-spectrum. This does not mean that no secondary or tertiary amides are present in the coating, but it is clear that these structures will not be the main component of the coating.

4.5.3 Chemical composition after water incubation

In order to obtain more information on the chemical composition of the coating, the samples that were water incubated are also examined with FT-IR and XPS.

4.5.3.1 Fourier transform infrared spectroscopy

Figure 4.22 illustrates the differences in the FT-IR spectra after 3 and 7 days of water incubation.

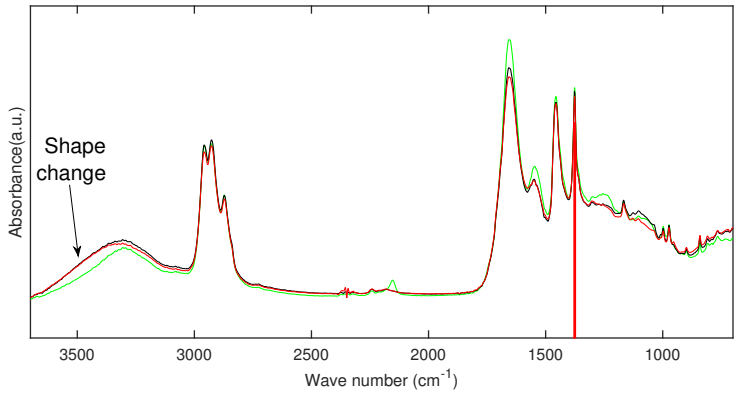

Figure 4.22: FTIR spectrum of pPBuOx (P_{avg}=36.2 W) at 0 (green), 3 (black) and 7 (red) days of water incubation.

As observed, there are not much changes in the spectra of water incubated plasmOx-coatings. For all coatings, a change in the shape in the broad peak (N-H and O-H stretch) between 3500 and 3000 cm^{-1} is observed. Overall, a broadening of this peak at the higher wavenumbers is obtained. As the O-H stretch typically lies at higher wavenumbers than the N-H stretch, this may indicate that relative to the amount of N-H functionalities, more O-H functionalities are present in the coating after water incubation. This may be caused by reaction of the coating with water or by residual water in the coating that is not evaporated after vacuum incubation. Furthermore, the only major difference is the disappearance of the peak at 2154 cm^{-1}, as illustrated in figure 4.23. This peak is not always as pronounced as in the presented figure, but for every coating in which the peak was pronounced, the peak disappeared after water incubation. This is an indication that this peak originates from isonitriles, as isonitriles undergo acid catalyzed hydrolysis (deionized water is slightly acidic). [124] Small differences are also observed at wavenumbers lower than 1375 cm^{-1}. For other coatings, sometimes a more pronounced difference was present in between the measurements after water incubation. There is however no consistency in these differences and because of the unknown plasma process, it is difficult to assign these peaks.

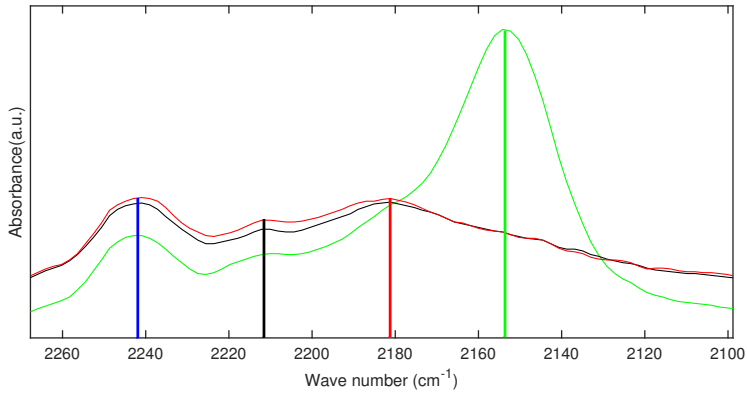

Figure 4.23: Detail of FTIR spectrum of pPBuOx (P_{avg}=36.2 W) at 0 (green), 3 (black) and 7 (red) days of water incubation.

4.5.3.2 X-ray photoelectron spectroscopy

Elemental composition

By performing survey measurements of the samples that were incubated in water, the elemental composition of the top layer that contacted with the water can be derived. These results are shown in figure 4.24-4.26.

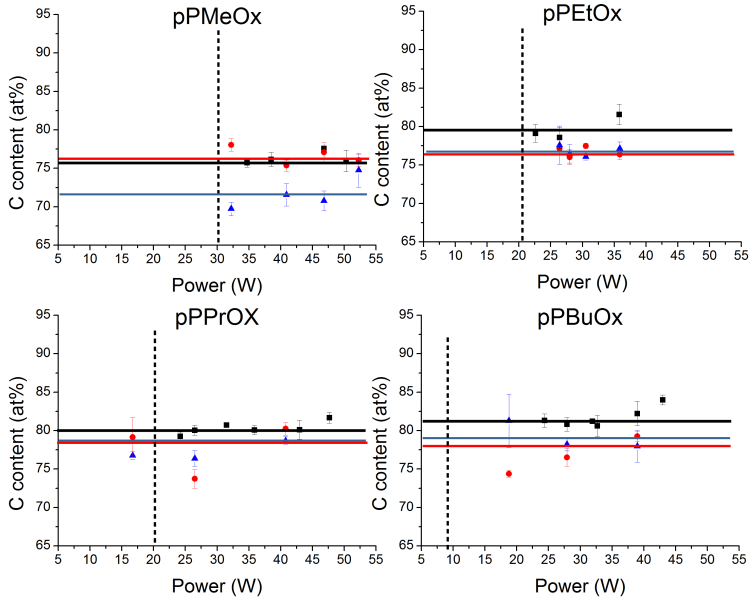

Figure 4.24: C content for 0 days (black), 3 days (red) and 7 days (blue) of water incubation for the different monomers. The colored lines indicate the average for the days of water incubation. The dotted black line indicates the boundary for 'stable' coatings for each monomer.

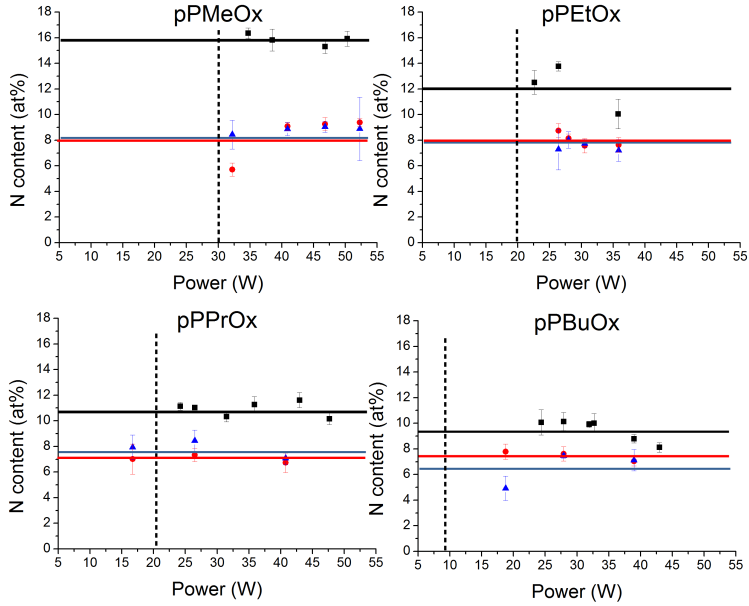

Figure 4.25: N content for 0 days (black), 3 days (red) and 7 days (blue) of water incubation for the different monomers. The colored lines indicate the average for the days of water incubation. The dotted black line indicates the boundary for 'stable' coatings for each monomer.

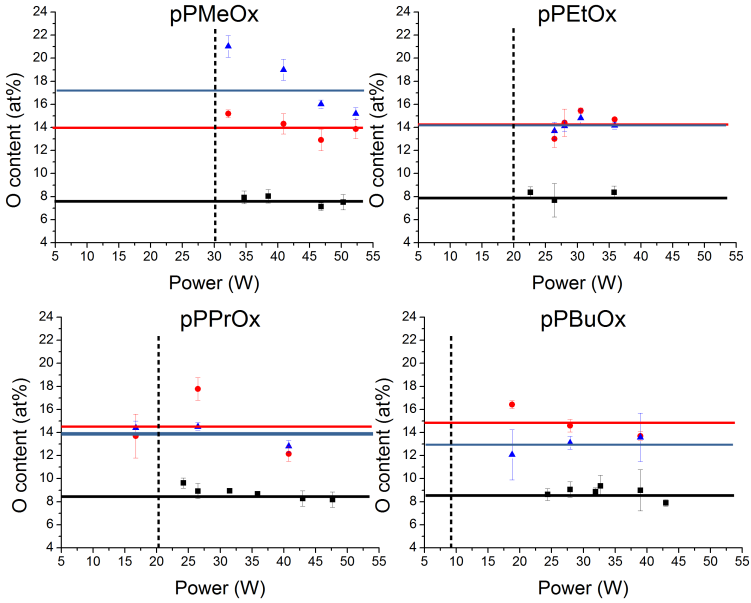

Figure 4.26: O content for 0 days (black), 3 days (red) and 7 days (blue) of water incubation for the different monomers. The colored lines indicate the average for the days of water incubation. The dotted black line indicates the boundary for 'stable' coatings for each monomer.

Figures 4.24-4.26 illustrate that there are significant deviations in between the C, N and O content for one monomer in the stable region after water incubation. However, by taking the average of these values, which is indicated by the full lines in figures 4.24-4.26, clear trends are visible. The choice is made to work within the 'stable' region, in order to evaluate the reaction between the water and the coating as much as possible. For pPPrOx, 1 measurement in the 'metastable' region is taken to have 3 data points. The averages in figure 4.24 illustrate that there is a small decrease in C content for most of the conditions. Only for pPMeOx after 0 and 3 days of water incubation, the same average C content is obtained. The N content decreases for all monomers, as illustrated in figure 4.25. The average content after 3 and 7 days is comparable for all monomers. The largest deviation is observed for pPBuOx, which is caused by the lower measurement at 18.8 W. The decrease seems to smaller for an increasing aliphatic side chain length. The O content increases for all monomers, as illustrated in figure 4.26. For pPMeOPx and pPBuOx, a larger difference in between the average values after 3 and 7 days of water incubation is observed than for pPEtOx and pPPrOx. Based

on the large deviations in between measurements, it is difficult to see trends in function of the monomers and functions. It is however clear that a significant increase in O content and a corresponding decrease of C and N content is observed. This is probably caused by a reaction of N-containing groups with water. These groups could for example be imines or isonitriles. The presence of isonitriles is also indicated in section 4.5.3.1, while the presence of imines is also indicated in section 4.5.4.

Analysis of high resolution spectra

Figure 4.27 presents the high resolution spectra for pPMeOx (P_{avg}=46.8 W) before and after water incubation. No significant differences are observed for the C1s-spectrum. This is also observed for most of the other conditions. However, deviations are present for some measurements: for pPMeOx (P_{avg}=32.3 after seven days of water incubation, a broadening of the peak is observed at higher energies, while for pPBuOx (P_{avg}=13.8 W) after 7 days of incubation, a decreased intensity at higher energies is observed. For the N1s-spectra, a clear shift is observed for the N1s-spectra towards higher energies after water incubation, which is representative for the other measurements. There is no difference in between the spectra for 3 and 7 days of water incubation. This shift may be caused by the aforementioned reaction of N-containing groups with water. The O1s-spectrum after 3 days of water incubation is comparable with the spectrum after 0 days of water incubation, while a shift is observed for the spectra of 7 days towards higher energies. This shift is representative for the other pPMeOx samples, but it is not observed for the other monomers. This might correlate with the greater increase in oxygen content for pPMeOx in comparison with the other monomers. For these monomers, small variations are observed for this peak, but there was no clear trend.

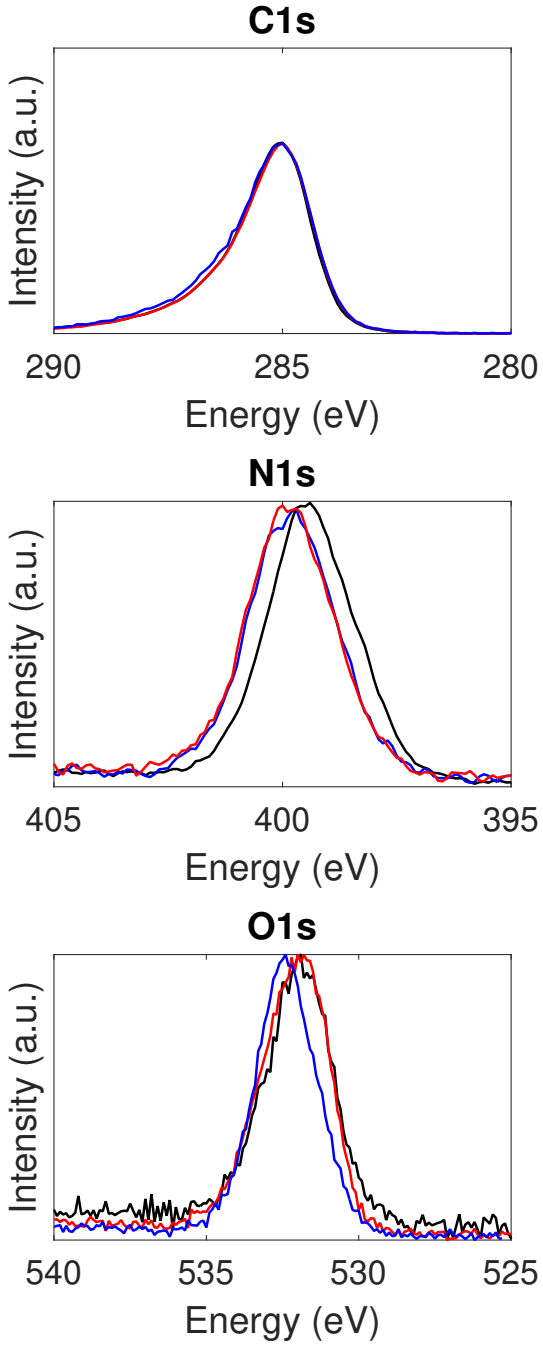

Figure 4.27: High resolution C1s-, N1s- and O1s-spectra from pPMeOx (P_{avg}=46.8 W) for 0 days (black), 3 days (red) and 7 days (blue) of water incubation.

4.5.4 NMR as an additional analysis technique

Because of the difficulties with determining the chemical composition of the coatings, an additional analysis technique is tested at the end of this thesis. The coatings are dissolved in $CDCl_3$ as described in B.4.4 and ^{1}H- and ^{13}C-NMR-spectra are measured. A result is presented in figure 4.28 and 4.29. Other measurements had a lower signal, because of less coating dissolution, but similar peaks were observed.

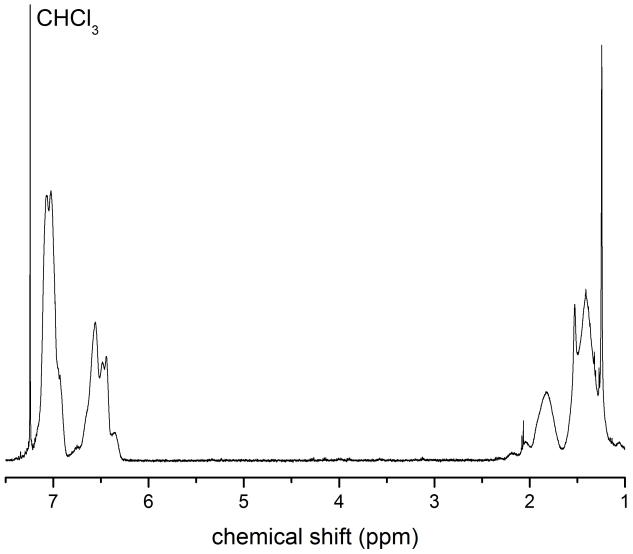

Figure 4.28: ^{1}H-NMR spectrum of pPPrOx (P_{avg}=30.5 W).

^{1}H-NMR (400 MHz, $CDCl_3$): δ=7.23–6.85 (m, 5H), 6.80–6.28 (m, 3H), 2.26–1.65 (m, 2H), 1.64–1.12 (m, 6H), 0.99–0.71 (m, 1H).

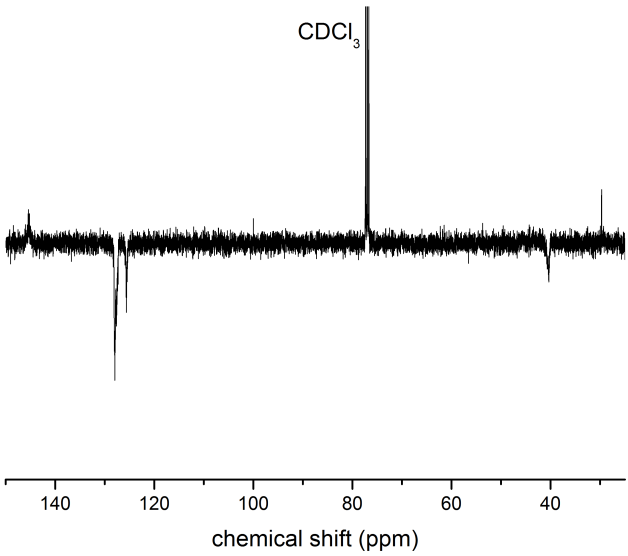

Figure 4.29: ^{13}C-NMR spectrum of pPPrOx P_{avg}=30.5 W

^{13}C-NMR (75 MHz, $CDCl_3$): δ=146-144.5 (C quaternary), 128.2–127.2 (CH), 125.8-125.4 (CH), 40.8–40.1 (CH/CH_3), 30.8-29.0 (CH_2).

These measurements are remarkable: the plasma process can be expected to have a random character, but only a limited amount of different peaks is observed, indicating the presence of a number of well defined processes. By carbon-proton coupling analysis of these measurements, it is observed that one proton of the peak at 7.23–6.85 ppm is linked to the carbon peak at 128.2–127.2 ppm, while another proton of this peak is linked to the carbon peak at 125.8-125.4 ppm. One proton of the peak at 6.80–6.28 ppm is also coupled to the carbon peak at 128.2–127.2 ppm. The broad peak in the ^{1}H-NMR-spectrum in between 2-1.65 ppm is coupled to the carbon peak at 40.8–40.1 ppm. The carbon peak at 30.8-29.0 ppm is linked to the proton signal at 1.3-1.25 ppm. The ^{1}H-NMR-spectrum of the plasmOx-coating is compared with the spectra of conventionally polymerized PrOx and the monomer.

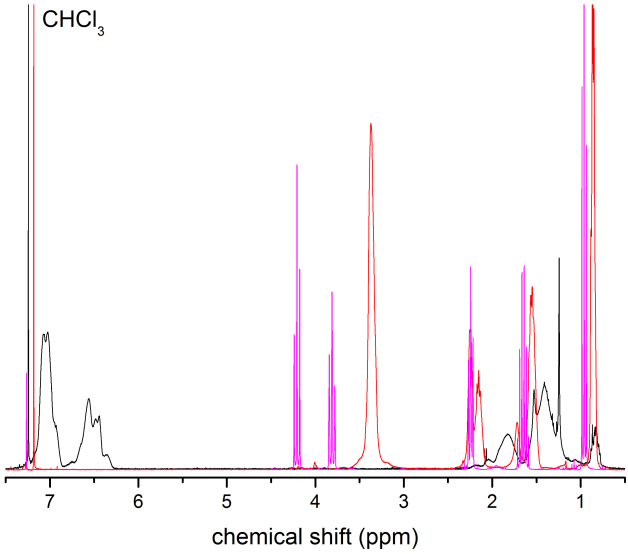

Figure 4.30: ^{1}H-NMR spectrum of pPPrOx P_{avg}=30.5 W (black), PPrOx (red) and PrOx (purple).

It is clear that the peaks around 7.0 and 6.5 ppm, which correspond to the coating, are not found in the monomer or polymer. The peak at 3.37 ppm of PPrOx, corresponds to the protons of the carbon adjacent to the nitrogen of the amide. This excludes the presence of tertiary amides in a large amount. This also excludes the presence of secondary amides in a large amount, as the carbon adjacent to the nitrogen will also have a similar chemical shift. The absence of the peaks typical to the oxazoline, exclude the presence of closed oxazoline-rings in high amounts in the coating.

The peaks below 2 ppm for the plasmOx-coating relate to different protons in aliphatic bonds. Associating a chemical structure is difficult because of the unknown plasma process. It is also difficult to draw conclusions based on one NMR-measurement. Likely, the peak at 6.80–6.28 ppm in the ^{1}H-NMR is related with the proton bounded to the carbon in an imine. This also corresponds with the ^{13}C-NMR. The peak at 7.23–6.85 ppm is more difficult to designate. A possible chemical structure that corresponds with this peak is an oxazole. This can also explain the fluorescence that was observed from a pPEtOx coating, by a co-worker in the Supramolecular Chemistry group, as illustrated in

figure 4.31. Further research is however needed to confirm this.

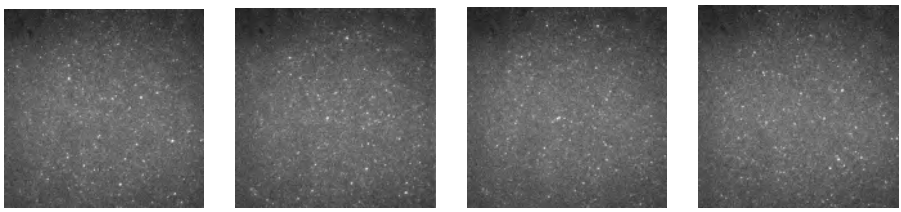

Figure 4.31: 4 images of the fluorescence of a pPEtOx coating. A 488-nm line from a diode laser is used for excitation. (100mW, SpectraPhysics, Irvine, California).

4.6 Deposition speed

4.6.1 Optimization of the measurement

The deposition rate of the different monomers gives additional information on the regime in which the plasma operates, as described in section 3.1.2.3. A comparison in between the deposition rate of the different monomers can also give information on the involved plasma processes. Thicknesses are measured for 'stable' coatings, as this is the most interesting area to describe the deposition speed. The measurement method is described in B.6. Different kind of steps are measured: figures 4.32-4.34 illustrate the three different steps that are observed.

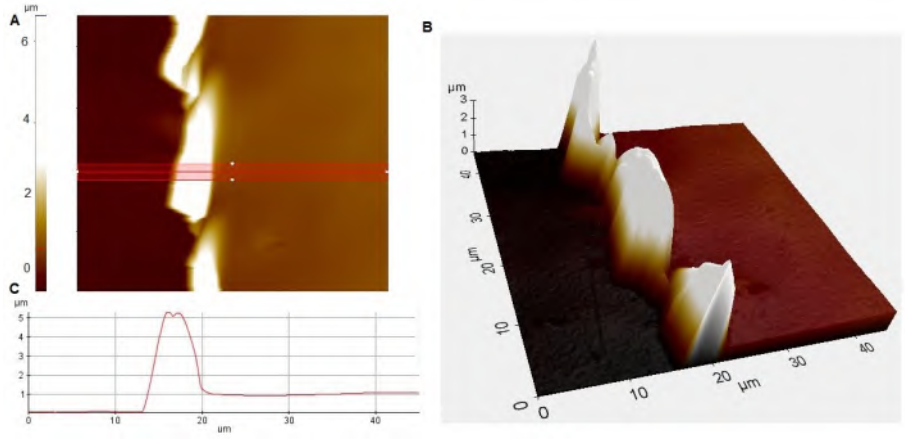

Figure 4.32: Step 1: AFM image of the step of bare substrate to coating. This image indicates a good measurement point: a stable coating thickness is obtained within the image after the step. A: 2D representation, B: 3D representation, C: line profile of the red segment in figure A.

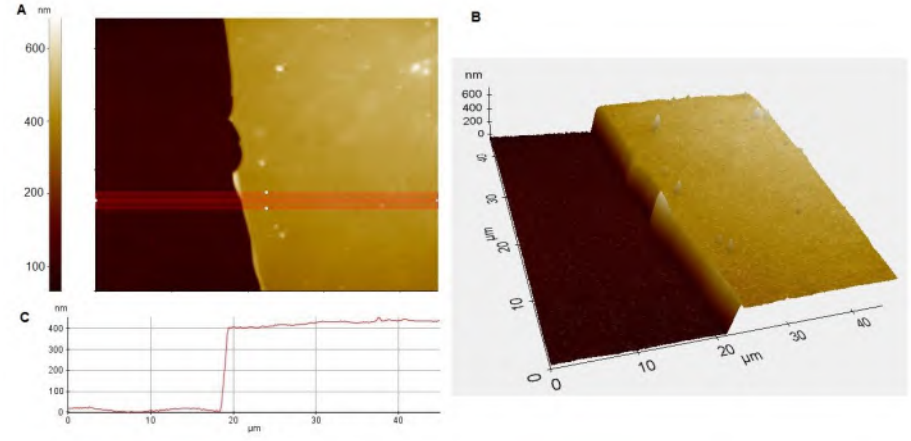

Figure 4.33: Step 2: AFM image of the step of bare substrate to coating. This image indicates a good measurement point: a stable coating thickness is obtained within the image after the step. A: 2D representation, B: 3D representation, C: line profile of the red segment in figure A.

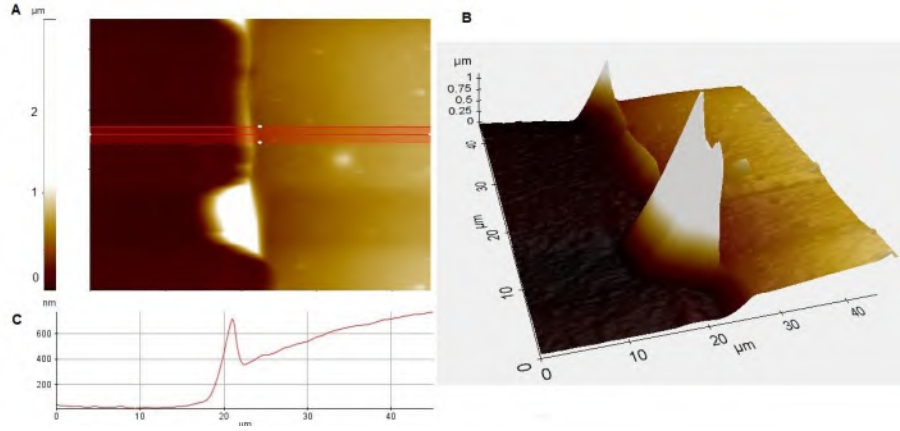

Figure 4.34: Step 3: AFM image of the step of bare substrate to coating. This image indicates a bad measurement point: the coating thickness varies over the total image after the step. A: 2D representation, B: 3D representation, C: line profile of the red segment in figure A.

The first two kind of steps indicate a stable coating thickness. This is also clearly illustrated in the line profiles in figure 4.32.C and 4.33.C. In the line profile of figure 4.34.C, it can be observed that the thickness of the coating changes significantly over the image. Indicating the thickness of the coating in this kind of measurements is therefore difficult. These measurements are therefore rejected for the analysis of the deposition speed.

The first measurements indicated two other important factors:

1. A large deviation is observed in between the measurement point at the same location on the sample. An example is a measurement along 1 cm on the right side of the sample at the top: thicknesses in the range of 144 nm to 336 nm are measured and an average of 263 nm with a standard deviation of 69 nm (pPMeOx P_{avg}= 29.2, 5 minutes of deposition, 10 measurement points). To be able to make a distinction in between the monomers, the choice was made to measure the thickness at longer deposition times (up to 20 min).

2. By using longer deposition times, a significant difference in between thicknesses at different locations on the sample is obtained. An example is the measurement on the right side of the sample at the top and the bottom of the same sample (pPEtOx P_{avg}= 31 W, 20 minutes of deposition): a thickness of 802 ± 90 nm is obtained

at the top, while a thickness of 455 ± 79 nm is measured at the bottom. This can be explained because the suction point of the pump is placed at the top right corner of the reactor, which is also visualized in figure B.4.

Going to longer deposition times had consequences: the heating of the electrode causes loosening between the tape and sample, leading to tape residues that remain on the sample after tape removal. These residues are also visible in figures 4.32-4.34. At most places of the sample, measurements are therefore difficult. The only place where all measurements could be performed was along the upper 1 cm of the right side of the sample. The measured thickness on this location is however not representative for the whole sample because of item 2 in the above-mentioned enumeration.

4.6.2 Results

From all measurement along the upper 1 cm of the right side of the sample, a significant amount has a step as illustrated in figure 4.34, which is named 'step 3' hereafter. The measurements with a thickness variation as illustrated in figure 4.32 or 4.33 ('step 1' and ' step 2'), indicated similar thicknesses of the coatings for the same condition. Step 2 is however less observed at higher deposition times. It is not observed for any deposition of 20 min.

As a thickness measurement for step 3, these measurement are not included in the results. The large presence of these kind of steps, indicate that the measurements presented hereafter are not representative for the real thickness of the coating at this location of the sample. The thickness measurement for the other steps are however performed, to investigate if there is a clear trend. These results are presented in table 4.12. All measurements are performed in the stable region, except for the pPMeOx at 24.7 W. Therefore, only one measurement is performed immediately after deposition. For pPBuOx at 29.8 W, measurements are performed at deviating time points, because of problems with the set-up.

A number of different observations can be performed for this measurement. Firstly, these measurements also have a large standard deviation for almost all measurements. This was already observed for previous measurements. Secondly, there is no clear trend in thickness increase for longer deposition times for a number of different conditions. For pPPrOx at 29.3 W, the thickness at 20 minutes is significantly lower

Table 4.12: Thicknesses (in nm) at different deposition times for the different monomers.

pPMeOx	5 min	10 min	20 min
29.2 ± 0.7 W	263 ± 69 nm	436 ± 119 nm	974 ± 164 nm
24.7 W			932 ± 126 nm

pPEtOx	10 min	15 min	20 min
27.1 ± 2.5 W	334 ± 98 nm	376 ± 108 nm	785.8 ± 85 nm
20.6 ± 0.1 W	457 ± 95 nm	648 ± 166 nm	663 ± 152 nm

pPPrOx	10 min	15 min	20 min
29.3 ± 1.1 W	130 ± 15 nm	623 ± 131 nm	252 ± 82 nm
20.9 ± 0.5 W	477 ± 82 nm	635 ± 76 nm	653 ± 133 nm

pPBuOx	7 min	10 min	13 min	15 min	20 min
29.8 ± 1.8 W	345 ± 89 nm	461 ± 124 nm	586 ± 158 nm		
19.2 ± 0.9 W		401 ± 126 nm		648 ± 166 nm	812 ± 187 nm

than for 15 min of deposition. For pPEtOx at 20.6 W and pPPrOx at 20.9 W, the thickness at 15 and 20 minutes is comparable. For pPEtOx at 27.1 W, the thickness at 10 and 15 minutes is comparable. Thirdly, an attempt to make a linear fit on the data gave only a reasonable result for 3 conditions. For the other measurements, a low R^2-value was obtained, or an unrealistic value for b (b>280 nm or b<-180 nm), with ax+b the linear fit. The reasonable fits are:

1. pPMeOx 29.2 W: thickness T in function of time t: T=48.3 $\frac{nm}{min}$. t - 6.1 nm. R^2=0.9905.
2. pPBuOx 19.2 W: T = 40.2 $\frac{nm}{min}$. t + 61.7 nm. R^2= 0.9995.
3. pPBuOx 29.8 W: T = 41.0 $\frac{nm}{min}$. t + 44.2 nm. R^2= 0.8337.

It is however difficult to draw any quantitative conclusions out of this data, because of the large variations in the data. It is clear that there are large variations in thicknesses for the same condition, which is probably caused by the high Ar flow (7 slm). This can cause the flow to become more turbulent, which will result in a less homogeneous deposition of the coating. It is also clear that there are large variations in deposition in between measurements. Repeated measurements would be needed to confirm if the measurements presented here are caused by random processes or by systematic differences in deposition speeds for different

measurements. It is also possible that the restriction to step 2 and 3, introduces the error: for example, 10 measurement points for pPPrOx at 29.3 W, 20 min of deposition, with step 2 and 3, result in a lower thickness than the for 15 min of deposition. It could however be that a higher deposition overall is present after 20 min than after 15 min, but that it could not be measured, because of the limited range of the AFM image.

4.7 Anti-fouling capacity of the coating

For the assessment of the non-fouling capacity of the coating, bacterial and cell tests were performed. For each monomer, samples were made at three different powers for both tests, as described in section B.7. All powers were chosen so that the coatings had WCAs corresponding to the 'stable' regime. This is chosen as such to assess the non-fouling capacity of the coating itself as much as possible and avoid the interference of coating that gets loose. Therefore, the coating is also incubated 21h in water before the tests, to remove the most loosely bound parts of the coating.

4.7.1 Cell tests

The results for the life/dead staining and proliferation tests of human foreskin fibroblasts (HFF) are presented in figures 4.36-4.39. The life/dead images for the bare PP substrate are presented in figure 4.35.

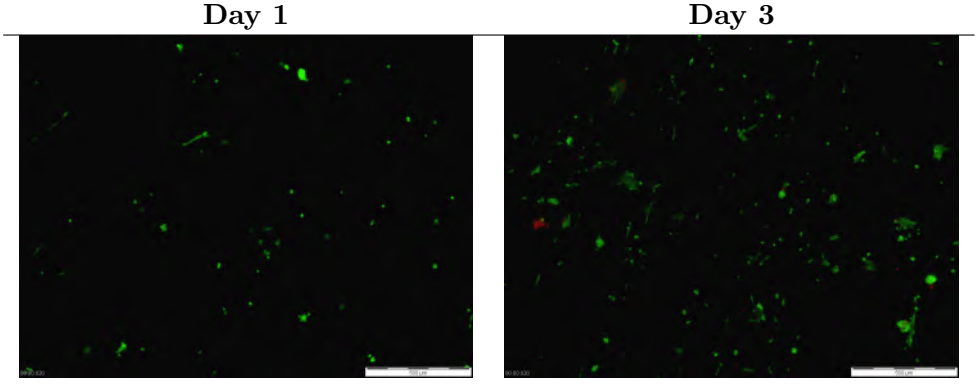

Figure 4.35: Life/dead staining of HFF for bare PP at 1 and 3 days. Scale bars in the right bottom corner of each image indicate 500 μm.

The first thing that stands out, is the fact that all coatings have more cells attached to the surface than for bare PP. There is also a higher cell viability for all the coatings in comparison with the bare PP substrate, as shown in figures 4.40 and 4.41. pPBuOx (P_{avg}=25.1 W) even has a cell viability that lies at 93% of the cell viability of a tissue culture plate. This indicates that HFF have a higher affinity for the coating than for PP. As such, there is no anti-fouling effect of the coating towards HFF. The cell viability results are however interesting for tissue regeneration purposes. Prolonged measurements would be needed to confirm this, but this is a promising result in comparison with other plasma coatings. [125]

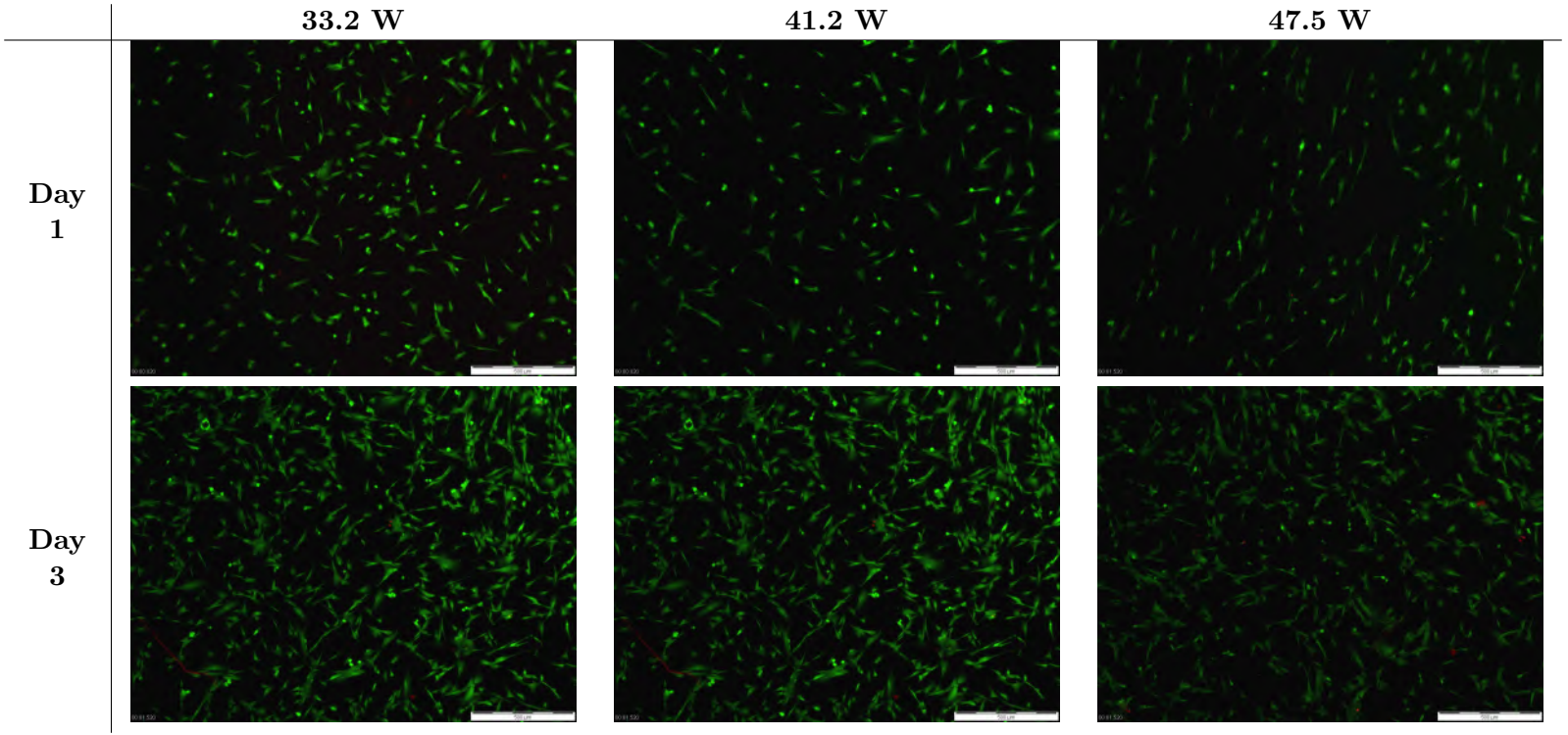

Figure 4.36: Life/dead staining of HFF for pPMeOx (1 and 3 days) at three different powers. Scale bars in the right bottom corner of each image indicate 500 μm.

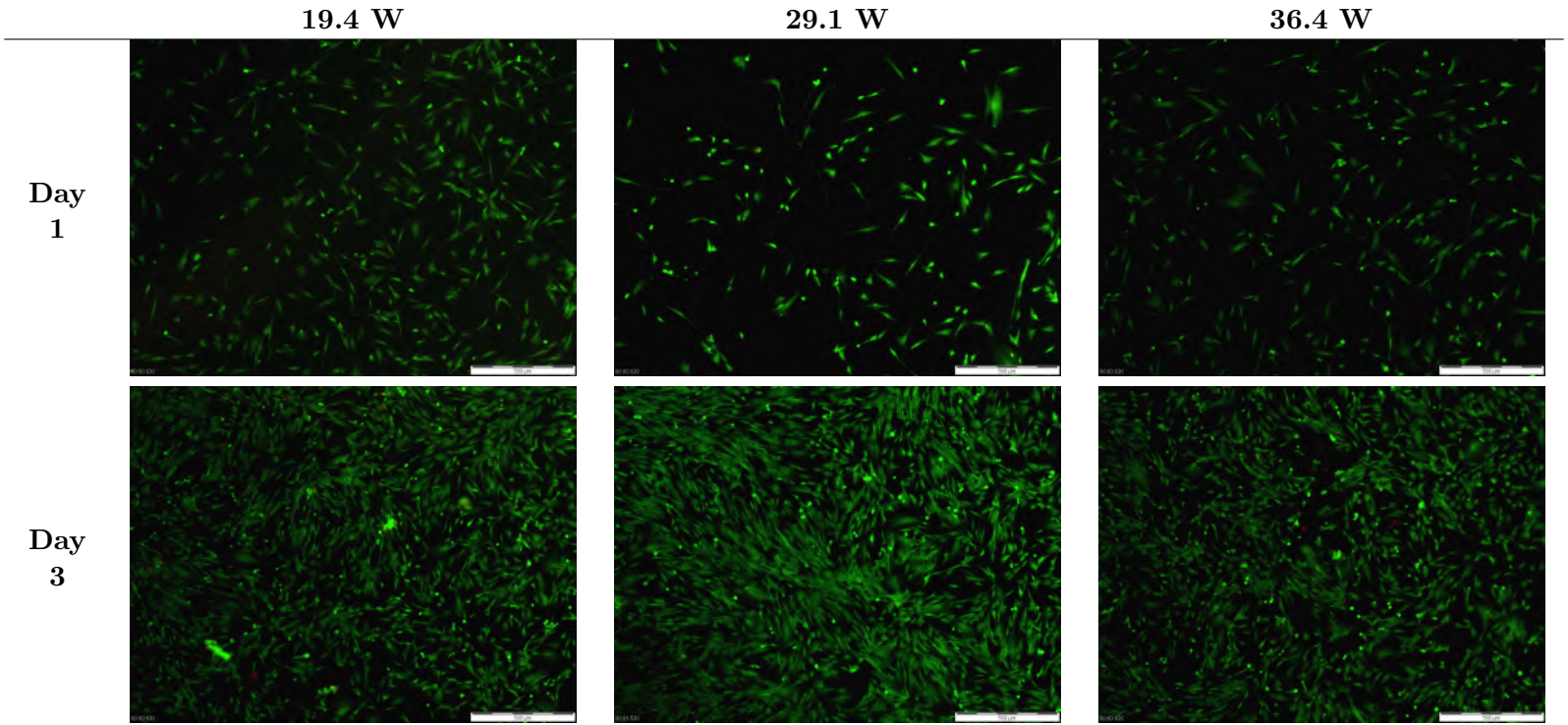

Figure 4.37: Life/dead staining of HFF for pPEtOx (1 and 3 days) at three different powers. Scale bars in the right bottom corner of each image indicate 500 μm.

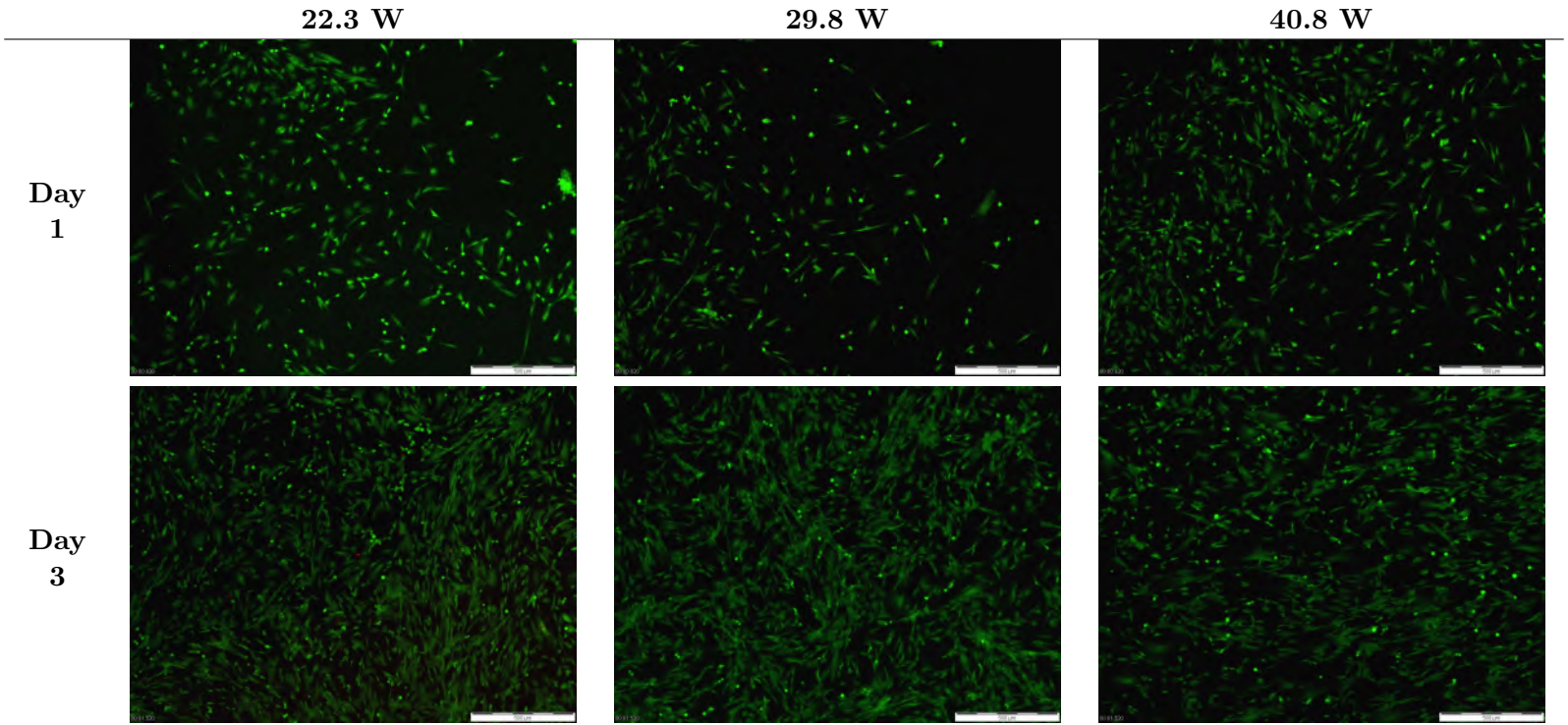

Figure 4.38: Life/dead staining of HFF for pPPrOx (1 and 3 days) at three different powers. Scale bars in the right bottom corner of each image indicate 500 μm.

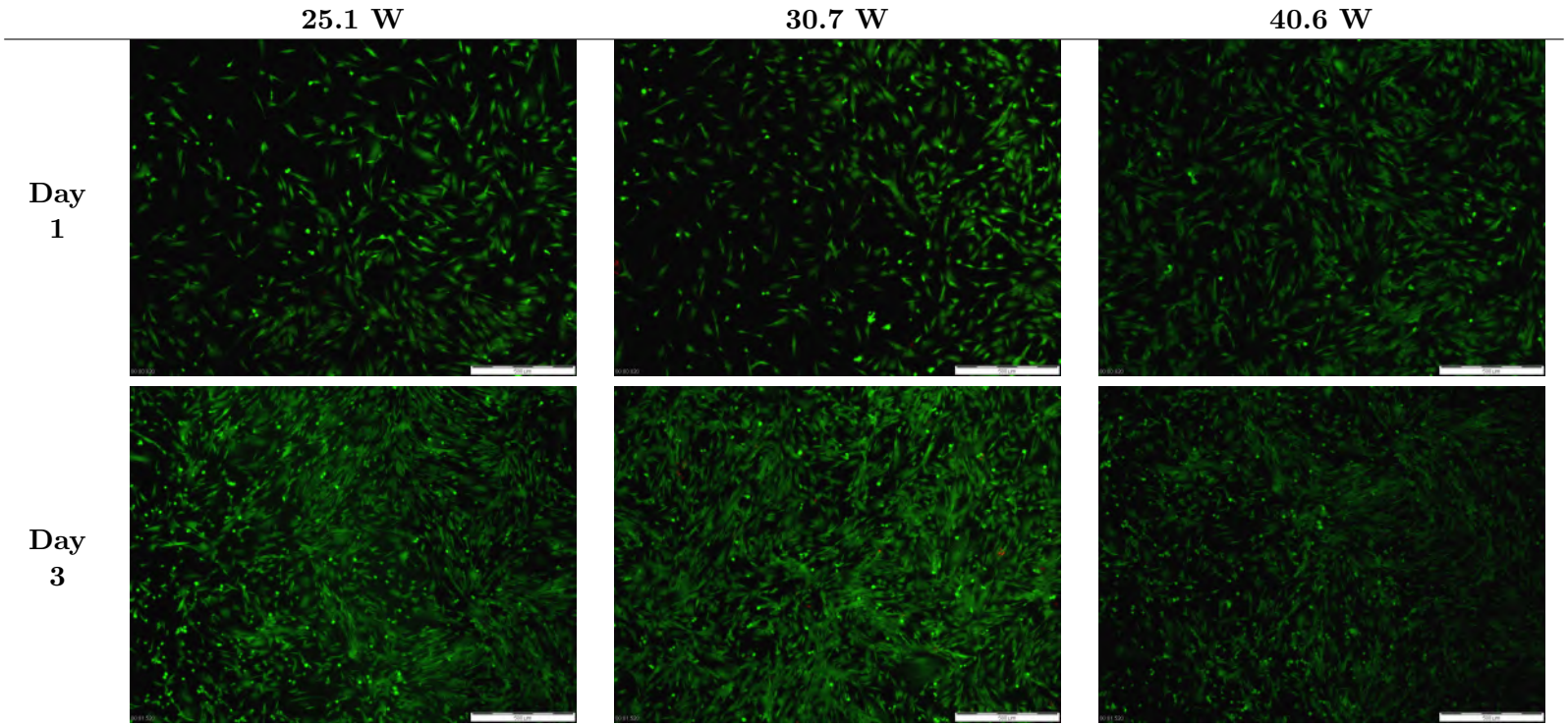

Figure 4.39: Life/dead staining of HFF for pPBuOx (1 and 3 days) at three different powers. Scale bars in the right bottom corner of each image indicate 500 μm.

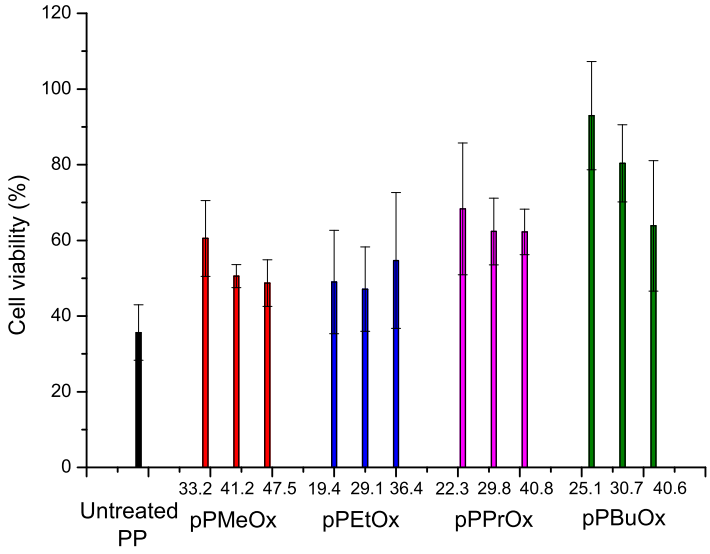

Figure 4.40: Results of the MTT assay for 1 day of cell culture. The cell viability is normalized to a tissue culture plate and expressed in percentage. For each monomer, the powers are placed under the columns (in W) and arranged in ascending order.

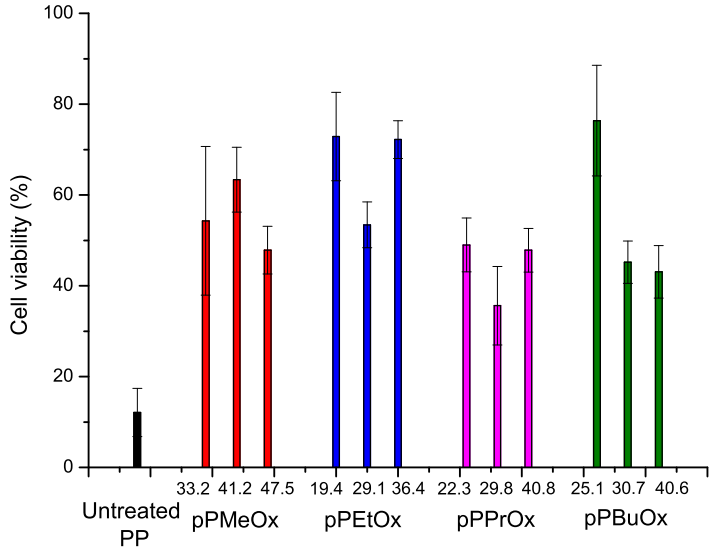

Figure 4.41: Results of the MTT assay for 3 days of cell culture. The cell viability is normalized to a tissue culture plate and expressed in percentage. For each monomer, the powers are placed under the columns (in W) and arranged in ascending order.

After 1 day of cell culture on the plasmOx-coatings, a trend is visible in between the different monomers and powers. The MTT-assay indicates a higher cell viability for pPBuOx and pPPrOx in comparison with pPMeOx and pPEtOx. For pPMeOx, pPPrOx and pPBuOx, a trend towards higher cell viability at lower powers is observed. Although these differences are not statistically significant, these trends are also observed in the images of the life/dead staining. In between monomers, a trend towards a better cell morphology and attachment is observed at lower powers. Also in between the monomers, a trend towards better cell morphology and attachment is observed in function of a growing alihpatic side chain.

After 3 days of cell culture on the plasmOx-coatings, the differences in between the coatings have become smaller. With respect to the tissue culture plate, the cell viability of pPPrOx and pPBuOx (except at 25.1 W) decreased, while this increased for pPMeOx and pPEtOx. In the life/dead staining, significant differences in cell morphology in between the coatings are no longer observed. In terms of cell attachment, there seems to be a small trend in cell density: a higher cell density is observed

for lower powers for the same monomer and for a growing aliphatic side chain.

4.7.2 Bacterial adhesion tests

A second test to assess the anti-fouling behavior of the coatings, was a bacterial adhesion test as described in section B.7.1. *Staphylococcus Aureus* and *Pseudomonas Aeruginosa* were the used microorganisms. First tests for pPEtOx, with a substrate coated at one side, indicated a very large standard deviation, making comparison between the different conditions difficult. Therefore, the next samples are measured with samples with coating at both sides, as discussed in section B.7.1. Figure 4.42 presents the results for all tests. For *S. Aureus*, there is a higher standard deviation than for *P. Aeruginosa*. Even for *P. Aeruginosa*, there is no significant change in bacterial adhesion for the two microorganisms, which may be an indication that the bacteria are not penetrating in the superglue that attaches two samples.

For *S. Aureus* attachment, a decrease in bacterial attachment is observed for pPBuOx at 25.1 and 30.7 W. This is however not significant due to the large standard deviation of the control and for the measurements itself. For *P. Aeruginosa*, no significant decreases in bacterial attachment are observed. These results indicate that no significant anti-fouling effect is present for the synthesized plasmOx-coatings.

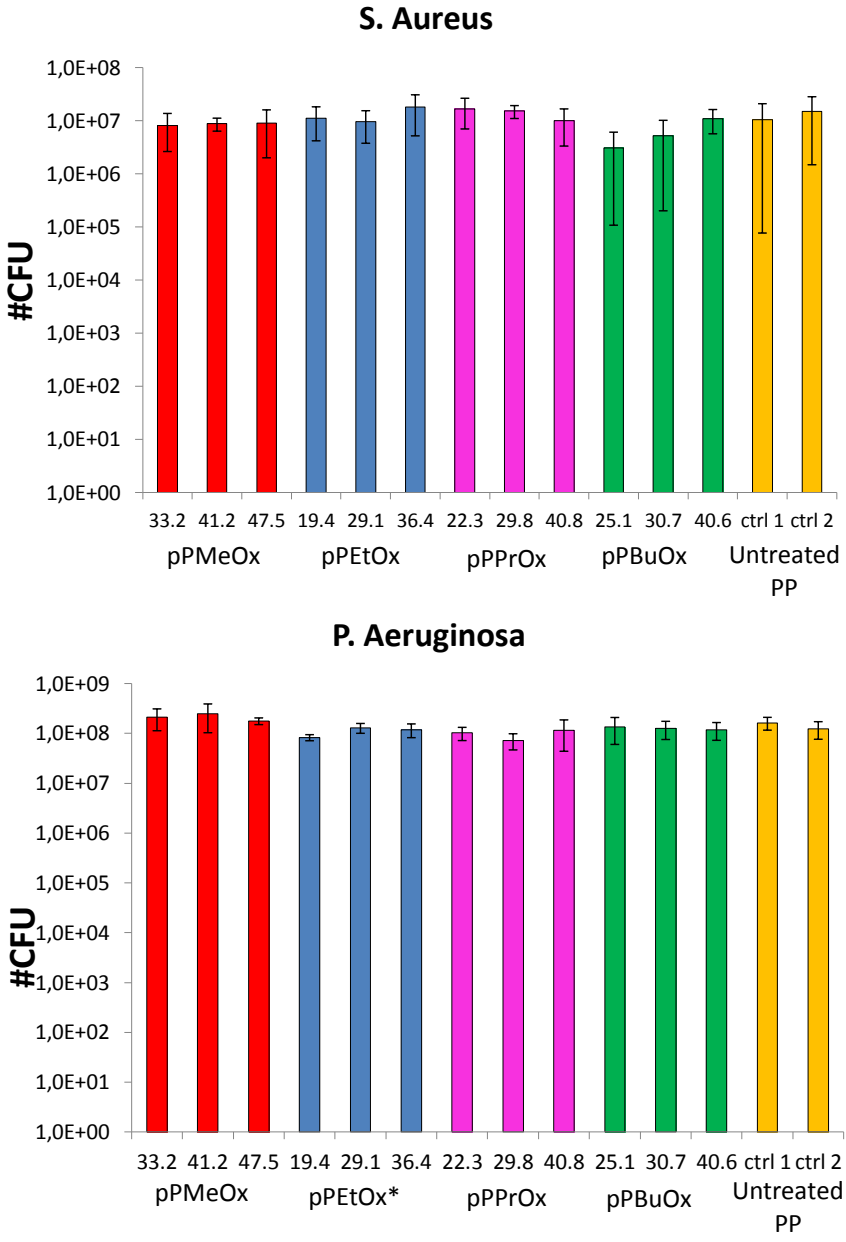

Figure 4.42: The numbers of colony forming units (CFU) for each monomer and power. Ctrl 1 is untreated PP that is glued in the same way as the samples. Ctrl2 is a sample of untreated PP that has the same size as the other samples. *pPEtOx was tested with coating on one side.

Chapter 5

Plasma polymerization of methyl ester-containing 2-oxazoline

In this chapter, the plasma polymerization of a methyl ester-containing 2-oxazoline is examined. The monomer used therefore is methyl 3-(2-oxazoline-2-yl) propanoate (C_2-MestOx). This monomer contains an ester group in the side chain on the 2-position. The aim of this chapter is to investigate the possibility of introducing the ester functionality in plasmOx-coatings.

5.1 Monomer synthesis

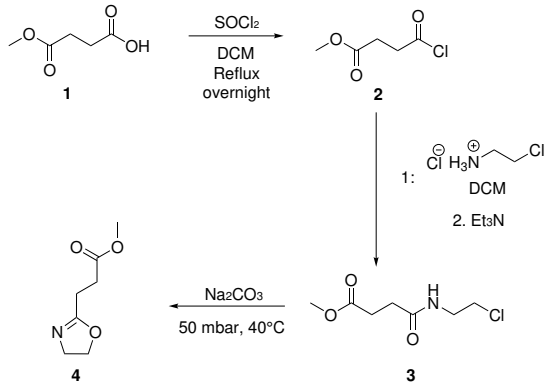

Figure 5.1: Synthesis of C_2-MestOx.

The synthesis of C_2-MestOx (4) starts from 4-methoxy-4-oxobutanoic acid (1), which reacts with thionyl chloride to form the corresponding acid chloride (2). 4-methoxy-4-oxobutanoic acid was obtained by ring opening of succinic anhydride. This reaction was performed by someone else in the group and the excess of 4-methoxy-4-oxobutanoic acid was used for the synthesis of C_2-MestOx in this thesis. The reaction is shown in figure 5.2.

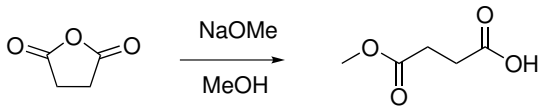

Figure 5.2: Synthesis of 4-methoxy-4-oxobutanoic acid.

In the next step, 2-chloroethylamino hydrochloride was added to the acid chloride that is dissolved in dry dichloromethane (DCM). Then, dry triethylamine (TEA) was added drop-wise. The water and organic phase of the resulting mixture were separated. The organic phase was dried with $MgSO_4$ and all volatiles were removed. As a last step, ring closure of the C_2-MestOx-precursor (3) was performed by addition of anhydrous sodium carbonate in a rotavapor set at 40°C and 50 mbar. The weaker carbonate base was added to avoid saponification of the ester. [126] The reaction mixture was filtered over celite and thereafter, the formed C_2-MestOx (4) was purified by fractional distillation. A second distillation over BaO was performed to dry the product. ^{1}H-NMR indicated that further purification was needed and this step was distributed within the Supramolecular Chemistry group because of the parallel program with the plasma polymerization process. A yield of 16% was obtained after the second distillation. This low yield was caused by a spill during the separation of water and organic phase after synthesis of product (3). For a complete description of the monomer synthesis, the reader is referred to appendix A.

5.2 Electrical characterization

The same pulse is applied as for pPMeOx, pPPrOx and pPBuOx. A detail of the discharge voltage and the resulting current during the 'on'-period is presented in figure 5.3. The voltage has a sinusoidal form, while the discharge current is a superposition of a sinusoidal waveform and several small current peaks. This indicates that the DBD set-up is operating as a pseudo-glow discharge. This was also the case for the

other monomers. This is desirable, as it leads to homogeneous plasma treatment of the sample. [122] This is representative for all applied voltages.

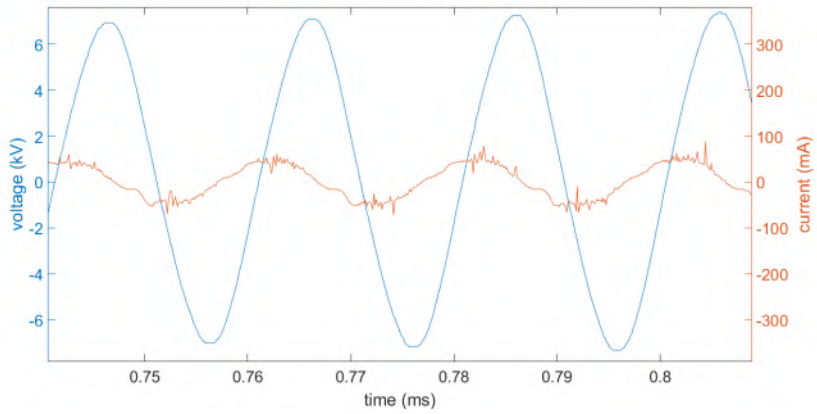

Figure 5.3: Detail of discharge voltage and current waveforms during 'on'-period.(P_{avg}=37.1 W)

5.3 Water contact angle measurements

WCA measurement of the pPC_2-MestOx as a function of discharge power are represented in figure 5.4.

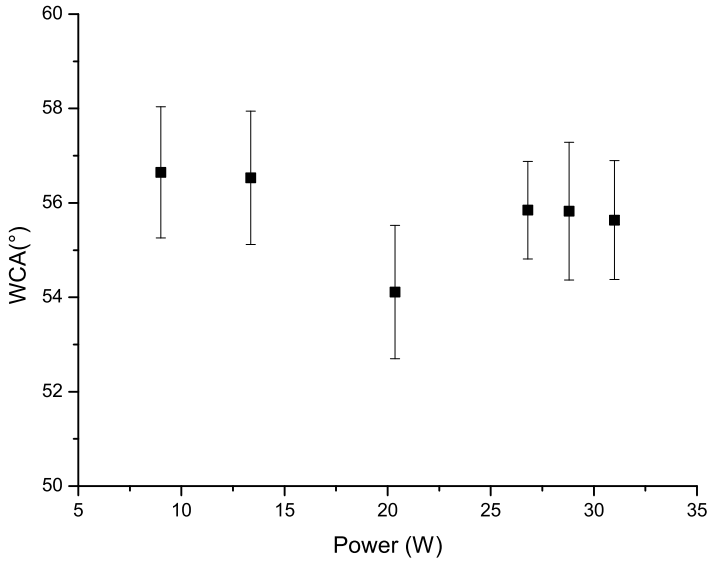

Figure 5.4: WCA of pPC_2-MestOx as a function of discharge power.

The WCA at 20.4 W is diverging minimally from the other WCAs. This was the first measurement. The other measurements yielded comparable WCA over a range of 9 W to 31.7 W. The WCAs indicate a wettability of the pPC_2-MestOx-coating comparable with the wettability of pPPrOx.

5.4 Coating stability

The stability assessment is represented in figure 5.5.

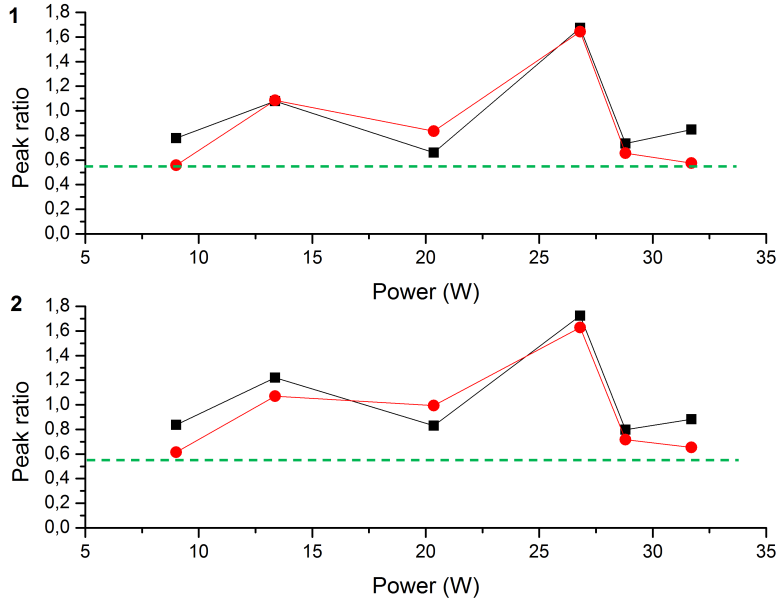

Figure 5.5: Ratio of the area of characteristic coating peak (scaled to substrate peak) for 3 (black) and 7 (red) days on the characteristic coating peak (scaled to substrate peak) for 0 days. Areas are calculated with integration method 1 in figure 1 and method 2 in figure 2. See section B.5 for explanation of the methods. The green dotted line of the previous chapter is given as an indication.

Both integration methods indicate 'stable' coatings, as described in the previous chapter. 'Stable' refers to a coating that still has a considerable FT-IR signal at the specific coating peak. The boundary value of the peak ratio is chosen at 0.55 in the previous chapter.

5.5 Chemical composition

Comparing the chemical composition of the pPC_2-MestOx with the other plasmOx-coatings, can make it possible to relate the differences to the methyl ester-functionality in the side group.

5.5.1 FT-IR

Figure 5.6 illustrates the differences and resemblances in between the FT-IR spectra of pPC_2-MestOx and pPPrOx, which is comparable for

the other monomers. The FT-IR spectrum of pPC_2-MestOx at 26.8 W is representative for the coatings at other powers.

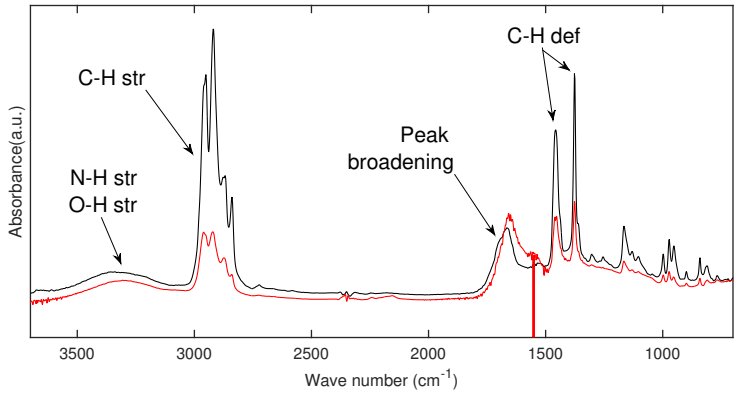

Figure 5.6: Comparison between FT-IR spectra of pPC_2-MestOx (P_{avg}=26.8 W) (black) and pPPrOx (P_{avg}=26.5 W) (red).

For pPC_2-MestOx, there is also a broad peak between 3500 and 3000 cm^{-1}, which can be assigned to N-H or O-H stretching vibrations, just like for the other plasmOx-coatings. The peaks between 3000 and 2800 cm^{-1} can be assigned to C-H stretching vibrations and are related to the PP substrate, the UHMWPE backing and the coating. The small broader peaks between 2250 and 2150 cm^{-1} are absent for pPC_2-MestOx. The broad peak at 1656 cm^{-1} is broadened towards higher wavenumbers, which is an indication of the presence of ester (1750-1735 cm^{-1}) and/or carboxylic acid groups (1780-1710 cm^{-1}). The peak at 1547 cm^{-1} (red vertical line) is also present in the pPC_2-MestOx-coating, but is shifted to a lower wavenumber. The peaks at 1459 and 1375 cm^{-1} correspond to C-H deformations, which are related to the PP substrate, the UHMWPE backing and the coating. The peaks below 1375 cm^{-1} are the peaks that are observed in the other plasmOx-coatings, which have no consistency in function of power. These are left unassigned in the previous chapter and therefore, this is also the case in this chapter.

5.5.2 XPS

5.5.2.1 Elemental composition

The survey scans for pPC_2-MestOx looked comparable to the survey scans of the monomers in chapter 4. This indicates the presence of C, N

and O, as expected. The elemental contents of C, N and O are derived as described in section 4.5.2.1 and these are shown in function of the applied power in figures 5.7-5.9.

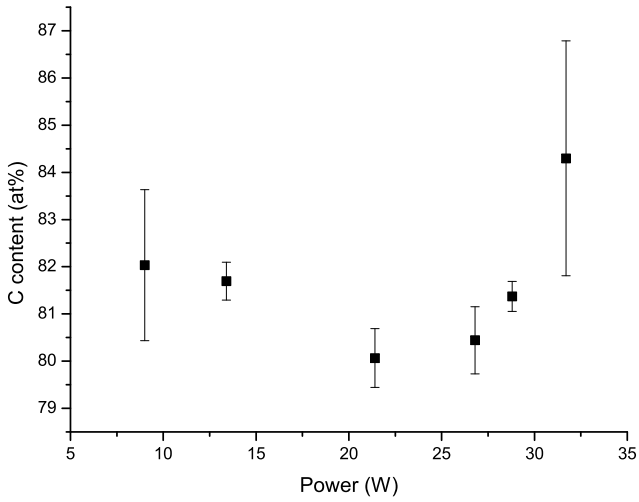

Figure 5.7: The carbon content of the coatings in function of the power for pPC_2-MestOx.

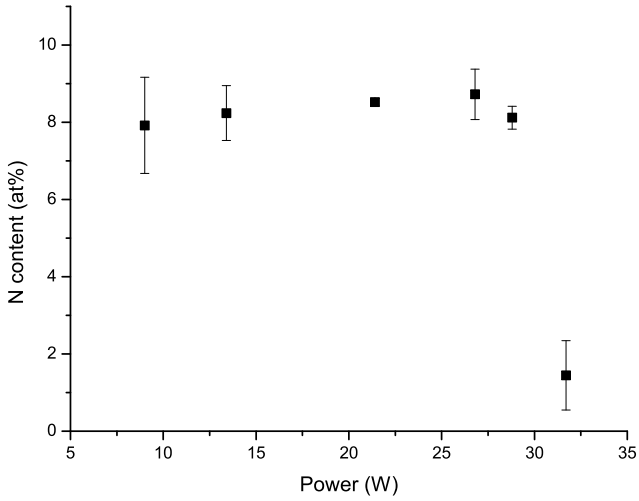

Figure 5.8: The nitrogen content of the coatings in function of the power for pPC_2-MestOx.

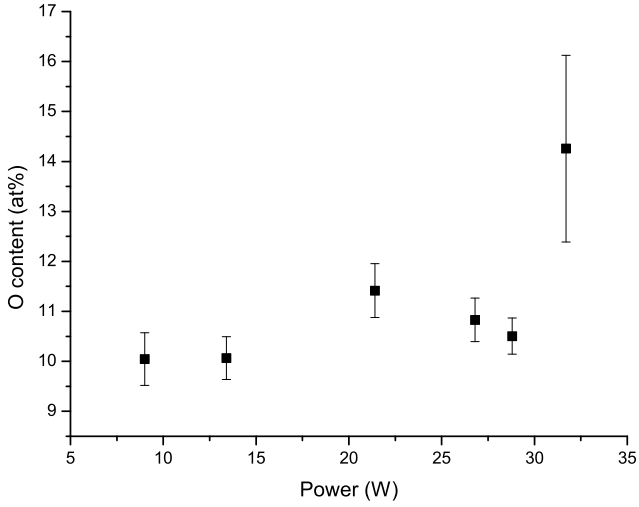

Figure 5.9: The oxygen content of the coatings in function of the power for pPC_2-MestOx.

These elemental concentrations show one deviating value at 31.7 W.

Further research would be needed to confirm whether this is an unrepresentative measurement for the sample. The other measurements, indicate a quite constant nitrogen content, while the oxygen and carbon contents vary coherently. This also corresponds with the WCA. For lower powers, the WCAs are a bit higher, just like the carbon content and for higher powers, this observation is the opposite. This elemental composition is compared with the elemental composition of the monomer and of pPPrOx (with a comparable wettability) in table 5.1. Therefore, the average is calculated over all the elemental contents, except the measurement at 31.7 W, although the values are not completely constant.

Table 5.1: Overview of the elemental contents of pPC_2-MestOx, pPPrOx ('stable' region) and the C_2-MestOx monomer. Averages and standard deviations are calculated from all the elemental contents.

	pPC_2-Mestox	pPPrOx	C_2-Mestox (monomer)
C content (at%)	81.1 ± 0.8	80.4 ± 0.8	63.6
N content (at%)	8.3 ± 0.3	10.8 ± 0.6	9.1
O content (at%)	10.6 ± 0.6	8.8 ± 0.5	27.3

For pPC_2-MestOx, the oxygen content is higher than for pPPrOx, while the nitrogen content is lower and the carbon content is comparable. This is expected, because C_2-MestOx has a higher oxygen content. However, the comparison with the monomer indicates a large amount of partition of oxygen-containing particles. This is probably caused by a fragmentation of the side chain.

5.5.2.2 Analysis of high resolution spectra

High resolution spectra are also obtained for pPC_2-MestOx. A result for one condition is presented in figure 5.10 and compared with two other plasmOx-coatings.

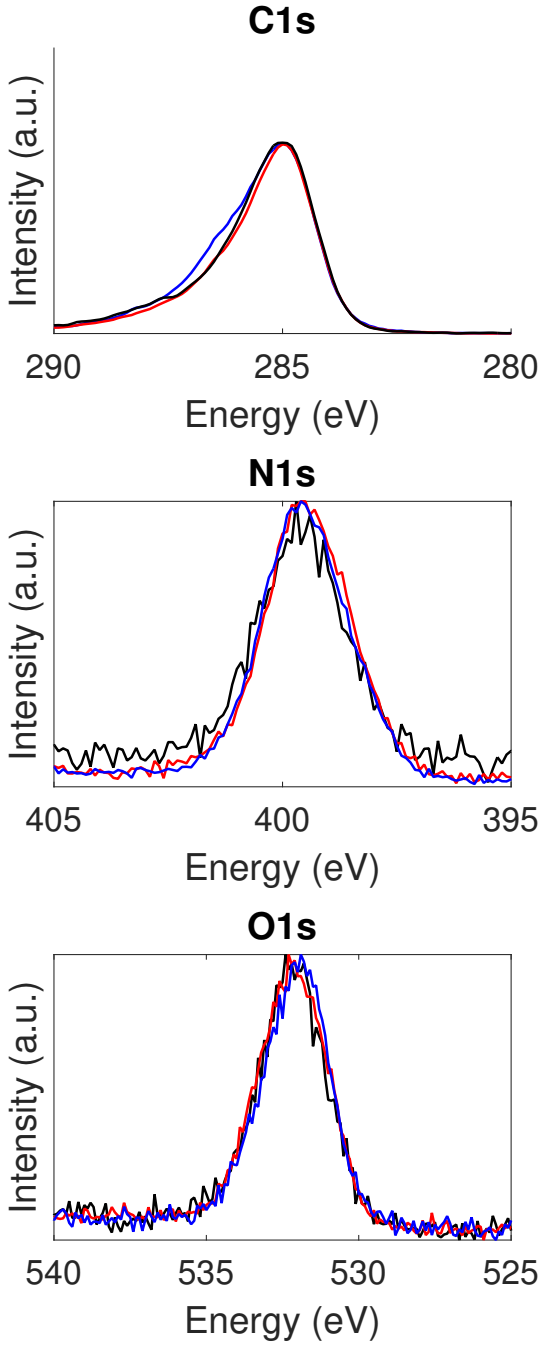

Figure 5.10: High resolution C1s-, N1s- and O1s-spectra from pPMeOx (P_{avg}=34.7 W) (blue), pPPrOx (P_{avg}=26.5 W) (red) and pPC_2-MestOx (P_{avg}=26.8 W) (black).

All spectra show no significant differences with the other plasmOx-coatings. In the C1s-spectrum, a small increase in intensity is observed at higher energies in comparison with pPPrOx. These are the energies related to esters, but this difference is not significant if this spectrum is compared to the spectrum of pPMeOx. In the N1s-spectrum, a small shift and change in FWHM can be observed. In the O1s-spectrum, no difference is observed between pPPrOx and pPC_2-MestOx. These observations are representative for the other measurements.

5.6 Monomer compatibility with the system

The second day after the monomer was inserted in the set-up, no monomer was flowing when the valve was opened. Opening the set-up made clear that the monomer was solidified. Therefore, no further measurements could be performed, which also explains the lack of data. The valve in the controlled evaporation and mixing (CEM) system was also blocked by the solidified monomer. The infrared measurements resulted in very small peaks characteristic to the coating in comparison with the peaks related to the PP substrate and UHMWPE backing. This may be caused by a reduced mass flow of the monomer, which can originate from obstructions due to the solidification. However, it may also be possible that the high boiling point (56°C at 0.3 mbar for the destillation) could have influenced the mass flow. This could also explain the high resolution XPS-spectra that were comparable to the other monomers: due to a lower flow, a high amount of fragmentation of the side chain resulted in similar coatings of a plasma containing just the 2-oxazoline ring with a aliphatic side chain. By introducing a bubbler system for the evaporation of the monomer, a set-up could be designed that can be compatible with the C_2-MestOx.

Chapter 6

Conclusion and outlook

In this thesis, the plasma polymerization of several 2-oxazolines was examined. pPC_2-MestOx was not compatible with the system, while pPMeOx, pPEtOx, pPPrOx and pPBuOx were successfully plasma polymerized. For these monomers, 'stable' coatings were obtained. 'Stable' refers to a coating that still has a considerable FT-IR signal at the specific coating peak (at least a peak ratio of 0.55) after seven days of incubation in deionized water and not to a coating that does not lose any of its thickness. A link was observed between the stability and the WCAs of the coating. For the increasing aliphatic side chain of the 2-oxazoline, a decreased wettability was observed via WCA measurements. This can be related to an increase in carbon content in the coating, which was confirmed with XPS. A shift of the boundary for which the coatings became 'stable' at the right side of the reactor is also observed for an increasing aliphatic side chain. Deposition speed measurements indicated a large variation in coating thickness, which can be explained by the high Ar flow that is used for plasma polymerization. Based on WCA and XPS, it is observed that all coatings have a relatively similar chemical composition in the total 'stable' region. For the 'unstable' region, more oxygen is present in the coating, but the XPS high resolution spectra did not show major differences in between the 'stable' and 'unstable' regime.

The main goal of this thesis was to synthesize anti-fouling coatings. However, cell proliferation and bacterial adhesion tests confirm that the coatings have no significant anti-fouling behavior. This can be explained because of the chemical composition of the plasmOx-coating, which is different from conventional PAOx. FT-IR and XPS have proven to be insufficient to efficiently characterize the coating composition and

therefore, no conclusion could be made within this thesis on the chemical composition of the coating. However, XPS data strongly indicates that the coating is not mainly composed of amides, in contrast to PAOx. NMR can be an additional technique to examine the chemical composition. An initial measurement resulted in a spectrum with peaks that are difficult to assign. Further analysis is needed to identify the chemical composition of the coating.

The lack of anti-fouling character differs from previously reported plasmOx-coatings. These studies postulated an anti-fouling effect of the coatings. It is however not clear if this effect is originating from the coating itself or from coating detachment. These reports also use a different technique for bacterial adhesion evaluation: by measuring the reduction of the surface coverage by the bacteria, an anti-fouling assessment is made. With this technique, they observed a maximal reduction to 33.6% of surface coverage by *S. epidermidis*. With the technique used in this thesis, this would not result in a significant bacterial adhesion reduction, because of the large standard deviations in the presented measurements. It is possible that a different chemical composition of the coating can explain these anti-fouling results. Only one publication inserted analyzable XPS-spectra. [89] The C1s-spectrum within this publication has a higher variation in function of the YF. A trend is observed from a comparable C1s-spectrum at high YF, to a C1s-spectrum that looks more like the spectrum of RO-PIPRO, as presented in figure 4.21, for lower YF. There is however no clear amide peak in the C1s-spectrum of the reported coatings. NMR can be a good technique to confirm if these coatings have a different chemical composition.

Continuation of this research can firstly focus on identifying the chemical structure of the coating. For the different monomers, several NMR-measurements can be performed with a good concentration of the coating in the solvent. Also other techniques can be used to determine the chemical composition, like Raman-Infrared. Also the coating thickness can be studied with other techniques, as AFM has proven to be a technique that did not work for the deposition in this thesis. Other techniques can be explored, like ellipsometry or profilometry. It can also be interesting to design a cooled electrode set-up, which could enable working at lower carrier gas flow rates. It can be studied if this results in more homogeneous coating thicknesses. AFM could then be used to assess the deposition speed for different monomers, or other techniques can also be employed. This would also enable a more quantitative stability assessment, by measuring the thickness decrease after water or PBS incubation. Once the chemical composition is derived, the reactivity of

the coating could be further explored. Also other 2-oxazoline monomers are interesting candidates for plasma polymerization. 2-isopropenyl-2-oxazoline can be for example tested to see if oxazoline ring retention can be obtained if a double bond is present in the side chain.

As the coating demonstrated good cell interaction, further research can also focus on the possibilities for tissue regeneration purposes. It can be studied if there are cell types that favor proliferation on plasmOx-coatings or if plasmOx-coatings evoke specific stem cell differentiation. With respect to the synthesis of anti-fouling coatings, it would also be interesting to test other monomers in order to obtain pseudo-mimetic coatings. Interesting monomers for this purpose are monomers that already contain a tertiary amide and preferably, a vinyl-bond. This may be a better option for plasma polymerization of anti-fouling coatings than 2-oxazolines.

Appendices

Appendix A

Monomer synthesis

A.1 Materials

The used solvents were of high-performance liquid chromatography (HPLC) grade and include: dichloromethane (DCM, $\geq$ 99.8%, Sigma-Aldrich), acetonitrile (ACN, $\geq$99.9%, Sigma-Aldrich) *N,N*-dimethylacetamide (DMA, $\geq$99.9%, Sigma-Aldrich) and triethylamine (TEA, $\geq$99.5%, Sigma-Aldrich). Chloroform-D ($CDCl_3$, $\geq$ 99.8%) was purchased from Euriso-top. Dry DCM, TEA and ACN were obtained from a custom made JW Meyer solvent purification system and dried over aluminum oxide columns.

Water used is MilliQ water prepared with a resistivity less than 18.2 MΩ x cm using an Arium 611 from Sartorius with the Sartopore 2 150 (0.45 + 0.2 μm poresize) cartridge filter.

The following chemicals were used as received: butyronitrile ($\geq$99%, Sigma-Aldrich), valeronitrile ($\geq$99%, Sigma-Aldrich), ethanolamine ($\geq$99%, TCI), zinc acetate dihydrate ($\geq$98%, Sigma Aldrich), barium oxide (BaO, 90%, Acros Organics), magnesium sulfate ($MgSO_4$, anhydrous, 97%, Acros Organics), thionyl chloride ($SOCl_2$, $\geq$99%, Sigma-Aldrich), 2-chloroethylamine hydrochloride (98%, Acros Organics), sodium carbonate (Na_2CO_3, anhydrous, 99.95%, Sigma-Aldrich), methyl-*p*-toluenesulfonate (MeOTs, 98%, Sigma-Aldrich), 2-ethyl-2-oxazoline ($\geq$99,8%, Polymer Chemistry Innovations), 2-methyl-2-oxazoline (98%, Chemical point), 4-methoxy-4-oxobutanoic (synthesized by Luis-Miguel García).

A.2 Characterization

A.2.1 Proton and carbon nuclear magnetic resonance

Nuclei of many elemental isotopes have a characteristic spin. The spinning charge of the nuclei of isotopes like ^{1}H and ^{13}C, generate a magnetic field and a magnetic moment proportional to the spin. By applying an external magnetic field, two spin states exist: a low energy state where the magnetic moment is aligned with the external field and a high energy state where the magnetic moment is opposed to the external field. The energy difference in between these states is proportional to the magnetic moment of the nucleus and the applied magnetic field. The applied magnetic field is strong (in the order of 1-20 Tesla) in order to increase this energy difference in between low and high energy state.

Irradiating the sample with photons with this exact energy difference, the resonance frequency, causes a transition from the low energy state to the high energy state of the nuclei. In chemical compounds, electrons will move in response to the external magnetic field. This generates a secondary field that shields the nuclei of interest of the applied field. This also increases the resonance frequency. Different chemical environments will therefore result in different resonance frequencies. By applying a short radio frequency pulse that is a superposition of all frequencies of interest, all nuclei are excited at their resonance frequency. The nuclei then relax to their low energy state by emission of radio frequency radiation at their resonance frequency. This resulting signal contains information on the chemical environment of the nuclei of interest. This shift in resonance frequency is represented by the unit 'chemical shift', which is expressed in parts per million (ppm). This unit is defined with respect to a reference signal, usually that of tetramethylsilane (TMS), as indicated in equation A.1. [127], [128]

$$\delta_{ppm} = \frac{\nu - \nu_{TMS}}{\nu_{TMS}} \tag{A.1}$$

Proton nuclear magnetic resonance (^{1}H-NMR) spectra of all intermediates and monomers were recorded on a Bruker Avance 300 MHz Ultrashield spectrometer or a Bruker Avance II 400 MHz spectrometer operating at room temperature. 5-10 mg of the analyte is dissolved in 0.7 mL of $CDCl_3$. All chemical shifts δ are given relative to the solvent peak of deuterated chloroform at 7.26 ppm for ^{1}H-NMR and 77.23 ppm for ^{13}C-NMR.

A.2.2 Size exclusion chromatography

Size exclusion chromatography (SEC) typically employs chemically modified inorganic silicas or polymeric porous beads packed into a column. This is the stationary phase. The polymer of interest is dissolved in a solvent and then, the solvent is pushed through the column by a pump. This mobile phase can flow between the beads and in and out of the pores in the beads, carrying the polymer molecules with it. The polymer occupies a certain volume in the solvent, depending on its molecular weight the kind of polymer and the solvent: polar polymers will occupy a larger volume in polar solvents than in apolar solvents and vice versa. This volume is called the hydrodynamic volume. If the hydrodynamic volume of the polymer chain in the solvent is much larger than the biggest pores in the beads, they cannot enter the pores and so are carried straight past by the mobile phase. If this volume is a little smaller than the biggest pores, they can enter the larger, but not the smaller pores. If this volume is smaller than the smallest pores in the beads, they can enter any of the pores. Polymers with a small hydrodynamic radius will therefore enter many pores in the beads and therefore leave the column slowly. For polymers with a large hydrodynamic volume, it will take less time to leave the column. Hereby, a separation is made in between small and larger molecules. To link the retention time of the polymer molecule to its molecular weight, a calibration with standard polymers of known weight is performed. [129]

SEC was performed on an Agilent 1260-series HPLC system equipped with a 1260 online degasser, a 1260 ISO-pump, a 1260 automatic liquid sampler (ALS), a thermostatted column compartment (TCC) at 50°C equipped with two PLgel 5 µm mixed-D columns and a precolumn in series, a 1260 diode array detector (DAD) and a 1260 refractive index detector (RID). The used eluent was DMA containing 50mM of LiCl at a flow rate of 0.500 mL/min. The spectra were analysed using the Agilent Chemstation software with the GPC add on. Molar mass values and dispersity index values were calculated against poly(methyl methacrylate) (PMMA) standards from PSS.

A.2.3 Gas chromatography

Gas chromatography (GC) is a chemical analysis technique for the separation of chemical components in a sample. The sample is therefore injected into a heated injection port, where it is volatilized. A carrier gas, which is called the mobile phase, is supplied to the inlet, carrying

the sample into a column, which is a long and narrow tube that is called the stationary phase. The sample is separated inside the column because each component will interact differently with the stationary phase. Behind the column, a detector generates an electronic signal, measuring the amount of each compound in the sample. [130]

Samples were measured with GC to determine the monomer conversion from the ratio of the integrals from the monomer and the reaction solvent. GC was performed on an Agilent 7890A system equipped with a VWR Carrier-160 hydrogen generator and an Agilent HP-5 column of 30 m length and 0.320 mm diameter. A flame ionization detector (FID) detector was used and the inlet was set to 250°C with a split injection of ratio 25:1. Hydrogen was used as carrier gas at a flow rate of 2 mL/min. The oven temperature was increased with 20°C/min from 50°C to 120°C, followed by a ramp of 50°C/min to 300°C.

A.2.4 Liquid chromatography mass spectrometry

Liquid chromatography-mass spectrometry (LC-MS) combines liquid chromatography (LC) and mass spectrometry. In LC, an analyte is dissolved and the solvent is pushed through a column that contains particles, the stationary phase. Comparable to GC, each component of the analyte will react differently with the stationary phase, leading to a separation of the components in the analyte. Behind the column, a detector generates an electronic signal, measuring the amount of each compound in the sample. After the column, a mass spectrometer is placed. The liquid needs to be transformed in ions. Therefore, different strategies exist. A common strategy is the use of an electrospray ionization (ESI) system. In this system, the liquid is brought into a metal capillary that is at a potential of several kilovolts relative to the surrounding chamber walls. Thereby, charge will be deposited on the surface of the emerging liquid, resulting in coulomb repulsion forces that result in a dispersion of the liquid in a fine spray. Ions emitted from charged droplets are then transferred into the vacuum chamber of a mass spectrometer. [131] There, the ions are separated based on their mass-to-charge ratio, by applying electric and/or magnetic fields. [132]

LC-MS analysis was performed on an Agilent 1100 HPLC with a quaternary pump and UV-DAD detection, coupled to an Agilent G1956B MSD. Ionization of the samples was achieved through an ESI ionization source. A Phenomenex - Kinetex C18 (5 μm 150 x 4.6 mm) column was used and a flowrate of 1.5 mL/min at 35°C and an injection volume of 15 μL. Solvent A was 5 mM NH_4OAc in H_2O whereas solvent B was

ACN. These solvents were used in a gradient in 6 minutes. Gradients of 0-100, 75-100 and 90-100 were used, always ending in 100% of B. The mass-range was 80-1000. The positive and negative ions are measured separately.

A.3 Methods and results

A.3.1 Synthesis of 2-*n*-propyl-2-oxazoline

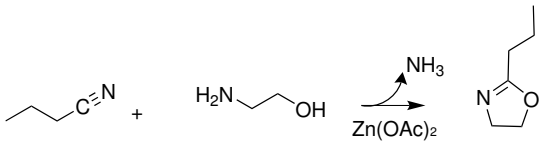

Figure A.1: Synthesis of 2-*n*-propyl-2-oxazoline via the Witte Seeliger method.

Butyronitrile (500 mL; 5.744 mol; 1 eq.) and ethanolamine (381.38 mL; 6.319 mol; 1.1 eq.) were mixed together and zincacetate (25.218 g; 0.1149 mol; 0.02 eq.) was added in catalytic amounts. The mixture was heated to 130°C for 3 days and stirred at 850 rotation per minute (rpm). A reflux condenser was put on top of the 2L round bottom flask to permit the mixture to reflux. The system was flushed with argon but afterwards, it was important to leave the reflux condenser open to the air, to allow the formed ammonia to escape. Ammonia will act as a nucleophile during the polymerization and therefore, it is important to get rid of all the ammonia. Due to oxidation of ethanolamine at high temperatures, a color change of the solution was observed from yellow to red and finally to black. GC was used to monitor the reaction.

After the reaction, two fractional distillations were performed. The first fractional distillation was performed to obtain the product from the residual mixture. The second distillation was performed to remove water (by adding BaO) and ammonia (by adding ninhydrine), as these nucleophiles interfere with the CROP. Ninhydrine is a chemical that is used to detect ammonia and primary and secondary amines, because reaction with these compounds lead to a deep blue color. The formed products from this reaction have a high molecular weight, giving them a high boiling point. This enables isolation of 2-*n*-propyl-2-oxazoline. Both fractional distillations were performed at 15 mbar and 45°C and

the first 20 mL are discarded. The product was obtained as a colorless liquid (354.05 g, 54% yield).

Chemical formula: $C_6H_{11}NO$

Molecular weight: 113.16 g/mol

^{1}H-NMR (300 MHz, $CDCl_3$): δ=4.14 (d, 2H, O-C**H$_2$**), 3.72 (d, 2H, N-C**H$_2$**), 2.24 (t, 2H, C-C**H$_2$**), 1.55 (sextet, 2H, C-CH_2-C**H$_2$**), 0.96 (t, 3H, CH_3).

LC-MS: Retention 4.32 min. (m/z: 114 ($[M+H^+]^+$)

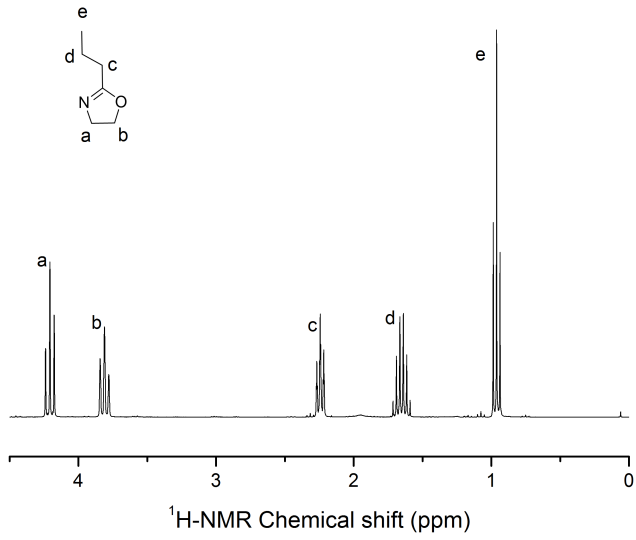

Figure A.2: ^{1}H-NMR spectrum of 2-*n*-propyl-2-oxazoline.

A test polymerization was performed. Therefore, 2 mL of a 4.0 M solution of the monomer (0.905 mL; 8 mmol; 1 eq.) in acetonitrile was prepared in a 5 mL microwave vial. Methyl tosylate (MeOTs) (0.012 mL; 0.08 mmol; 0.01 eq.) was added as an initiator to obtain a degree of polymerization around 100. This operation was carried out in the glove-box to prevent moisture contamination. The polymerization mixture was placed in the auto sampler of the Biotage microwave and was left to react at 140°C for 1099s to have approximately 99% of monomer conversion. A SEC measurement resulted in a polydispersity index (PDI) that indicated the presence of nucleophilic residues in the product.

Due to the parallel program with the plasma polymerization process, a further purification step was distributed within the Supramolecular chemistry group.

A.3.2 Synthesis of 2-*n*-butyl-2-oxazoline

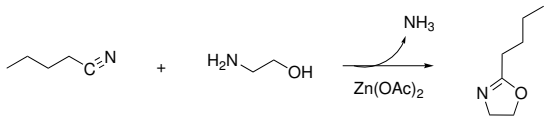

Figure A.3: Synthesis of 2-*n*-butyl-2-oxazoline via the Witte Seeliger method.

Valeronitrile (150 mL; 1.44 mol; 1 eq), ethanolamine (106 mL; 1.76 mol; 1.2 eq) and zinc acetate dihydrate (6.776 g; 30.87 mmol; 0.02 eq) were stirred at 130°C for 45 hours under reflux. The reaction was followed by GC until all valeronitrile had been consumed. After the reaction was allowed to cool down to room temperature, dichloromethane (300 mL) was added and the mixture was extracted with brine twice. The aqueous phases were extracted with small amounts of dichloromethane, after which the combined organic phases were dried over anhydrous magnesium sulfate, filtered, and the solvent was removed under rotary evaporation. Further purification was performed by distillation under reduced pressure at 70°C. A yield of 52% was obtained.

Chemical formula: $C_7H_{13}NO$

Molecular weight: 127.19 g/mol

^{1}H-NMR (300 MHz, $CDCl_3$): δ=4.05 (m, 2H, O-C**H$_2$**), 3.64 (m, 2H, N-C**H$_2$**), 2.24 (t, 2H, C-C**H$_2$**), 1.46 (m, 2H, CH_2-C**H$_2$**-CH_2), 1.20 (m, 2H, CH_2-C**H$_2$**-CH_3), 0.87 (t, 3H, CH_3).

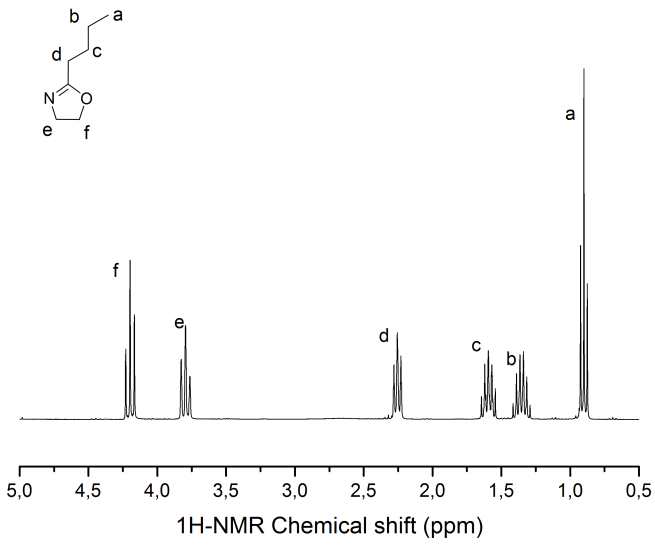

Figure A.4: ^{1}H-NMR spectrum of 2-*n*-butyl-2-oxazoline.

A.3.3 Synthesis of methyl 3-(2-oxazoline-2-yl) propanoate

Synthesis of methyl succinyl chloride

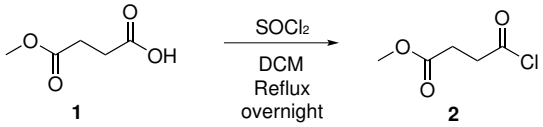

Figure A.5: Synthesis of methyl succinyl chloride.

Thionyl chloride (145.049 mL; 1.99706 mol; 2 eq.) was added dropwise to a solution of 4-methoxy-4-oxobutanoic acid (1) (131.62 g; 0.99853 mol; 1 eq.) in dichloromethane (750 mL) at 0°C. After the addition, the reaction was left to equilibrate to room temperature and was refluxed overnight to remove all volatiles. The resulting product was used in the following step without further workup.

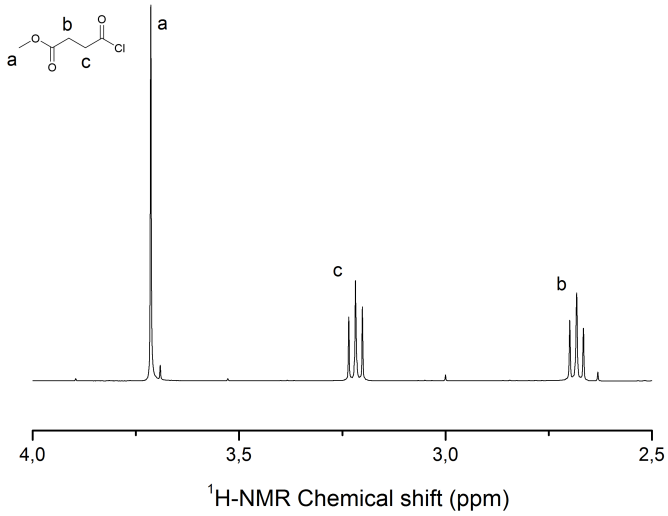

Figure A.6: ^{1}H-NMR spectrum of product (2).

Chemical formula: $C_5H_7ClO_3$

Molecular weight: 150.56 g/mol

^{1}H-NMR (400 MHz, $CDCl_3$): δ=3.71 (s, 3H, C**H$_3$**-O), 3.22 (t, 2H, C**H$_2$**-COOCl), 2.68 (t, 2H, C-C**H$_2$**-COOMe).

Synthesis of methyl 4-((2-chloroethyl)amino)-4-oxobutanoate

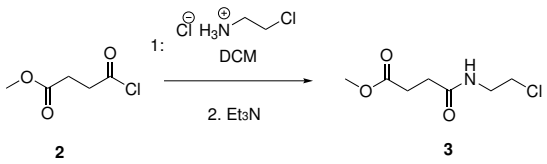

Figure A.7: Synthesis of methyl 4-((2-chloroethyl)amino)-4-oxobutanoate.

The crude of the previous reaction was divided into two equal batches. Each batch of the acid chloride (2) (2 x (75.17 g; 0.4993 mol, 1 eq.)) was dissolved in dry DCM (2 x 850 mL) under an inert atmosphere. Then, 2-chloroethylamino hydrochloride was added at 0°C (2 x (63.705 g;

0.5492 mol; 1.1eq.). Thereafter, triethylamine (2 x (175 mL; 1.2547 mol; 2.51 eq.)) was added dropwise to the mixture at 0°C and subsequently brought to room temperature. Constant stirring was necessary to prevent the formed triethylamine salt from precipitating. After stirring overnight, water was added to each batch and the layers were separated. The water phase was washed with DCM (3 x 250 mL) and after that, the organic phase was washed with water (2 x 250 mL) and with brine (250 mL). During this process, a part of one batch was spilled, which resulted in a lower yield. Subsequently, both batches were dried with $MgSO_4$ and all volatiles were evaporated on the rotavapor, giving a brown oil (136.4 g). Both batches were merged and this is used without further purification in the next step.

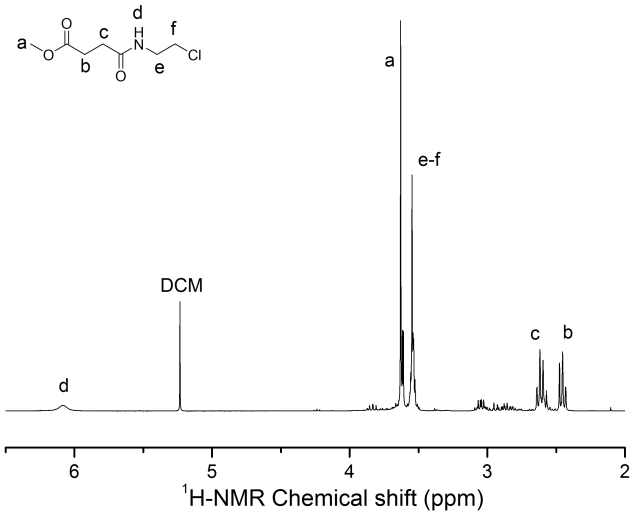

Figure A.8: ^{1}H-NMR spectrum of product (3).

Chemical formula: $C_7H_{12}ClNO_3$

Molecular weight: 193.6285 g/mol

^{1}H-NMR (300 MHz, $CDCl_3$): δ=6.14 (s, 1H, CON**H**), 3.69 (s, 3H, C**H$_3$**-O), 3.60 (m, 4H, C**H$_2$**-C**H$_2$**-Cl), 2.66 (q, 2H, C**H$_2$**-CONH), 2.55 (m, 2H, C**H$_2$**-COOMe).

Synthesis of methyl 3-(2-oxazoline-2-yl) propanoate

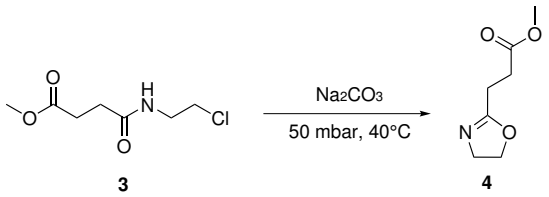

Figure A.9: Synthesis of methyl 3-(2-oxazoline-2-yl) propanoate.

Anhydrous sodium carbonate (70.93 g; 0.6692 mol; 0.95 eq.) was added to the precursor (3) (136.4 g; 0.7044 mol; 1 eq.) and the flask was mounted on the rotavapor (40°C, 50 mbar). After 4 days, DCM (200 mL) was added and the reaction mixture was filtered over celite. Thereafter, all volatiles were removed on the rotavapor and the crude product was purified through fractional distillation (70°C, 1.5 mbar) and the first 2 mL were discarded. This yielded the desired methyl 3-(2-oxazoline-2-yl) propanoate (C_2-MestOx) as a colorless liquid. A second fractional distillation was performed over BaO (56°C, 0.3 mbar), but ^{1}H-NMR indicated that the product was not dry and that further purification was needed. Due to the parallel program with the plasma polymerization process, this step was distributed within the Supramolecular Chemistry group. 25.514 g of the product was obtained, giving a yield of 16% yield.

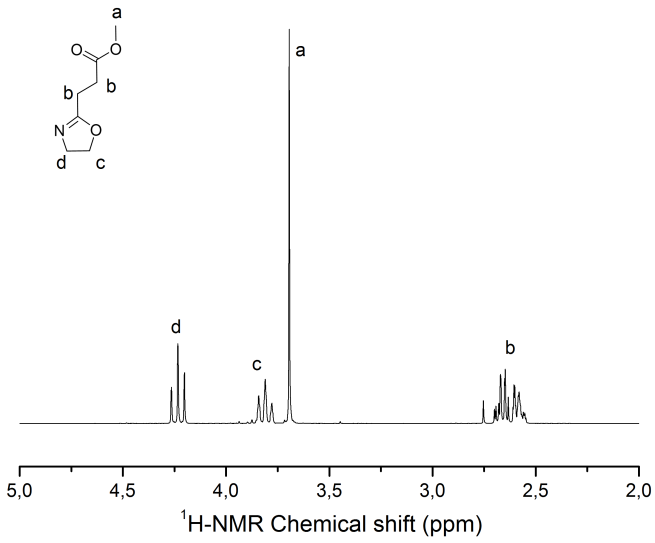

Figure A.10: ^{1}H-NMR spectrum of C_2-MestOx after one fractional distillation.

Chemical formula: $C_7H_{11}NO_3$

Molecular weight: 157.1676 g/mol

^{1}H-NMR (300 MHz, $CDCl_3$): δ=4.07 (t, 2H, N-CH_2-C**H_2**-O), 3.76 (t, 2H, N-C**H_2**-CH_2-O), 3.69 (s, 3H, O-C**H_3**), 2.62 (m, 2H, C-CH_2-C**H_2**-CO), 2.58(m, 2H, C-**H_2**-CH_2-CO).

LC-MS: Retention 3.77 min. (m/z: 114 ($[M+H^+]^+$))

Appendix B

Plasma polymerization: materials and methods

B.1 Materials

The monomers were obtained as described above. Argon (Ar) (Alphagaz 1) was purchased from Air Liquide and used as supplied. A roll of polypropylene (PP) (thickness: 0.05 mm, biaxially oriented) and a roll of ultra-high-molecular-weight polyethylene (UHMWPE) (thickness: 0.25mm) was ordered from Goodfellow Cambridge UK . Samples of different sizes, depending on the purpose, were cut out for treatment and used without any pre-treatment.

B.2 Plasma methods

The plasma activation and polymerization were performed in a dielectric barrier discharge reactor (DBD), which is schematically shown in figure B.1. The gas discharge was generated between the lower copper electrode ($\varnothing$ $\bar{4}$8 mm) that was covered with ceramic layer of 3.3 mm and the upper woven stainless steel electrode as shown in figure B.1. The gap between the electrodes was 8 mm. The gas was fed to the perforated upper electrode via a single inlet and passed quartz wool before entering the plasma reactor. This electrode was grounded through a resistor R (50 Ω). The lower electrode was connected to high frequency (50 kHz) AC power source. A pulsed voltage was applied to the lower electrode by using a 10 MHz pulse generator.

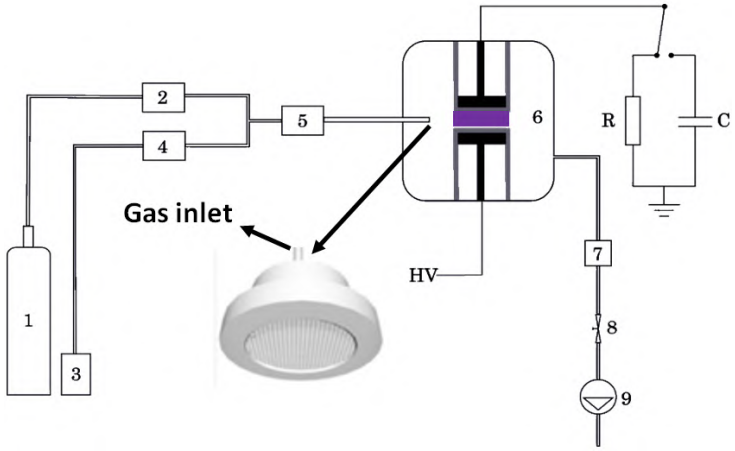

Figure B.1: Schematic representation of the used delectric barrier discharge set-up. 1) Ar bottle, 2) Bronkhorst El-Flow mass flow controller, 3)monomer container, 4) Bronkhorst CORI-FLOW meter, 5) Controlled evaporation and mixing (CEM) system, 6) Plasma reactor, 7) Manometer, 8) Pressure valve and 9) Pumping unit.

The PP sample was placed on the ceramic layer covering the lower electrode and fixed at all sides with tape. Firstly, the reactor was pumped down to <0.5 mbar using a rotary vane pump. Secondly, the reactor was filled with Ar by using the Bronkhorst El-Flow mass flow controller at 3 standard liter per minute (slm). After reaching a pressure of 0.5 bar, this pressure was maintained and the system was flushed with Ar at 3 slm for 3 min. This purging step and the previous pumping step were performed to obtain a reproducible gas composition in the plasma reactor. Thirdly, the Ar flow was reduced to 1 slm and the system pressure was lowered to 0.05 bar. The plasma was turned on for 30 seconds at a power of 3.85±0.5 W. The purpose of this plasma activation step was to incorporate radicals on the substrate surface for covalent bonding of the plasma coating. Fourthly, the Ar flow was increased to 7 slm and the system pressure was brought back to 0.5 bar. The monomer flow was then put to 0.2 g/h by using a Bronkhorst CORI-FLOW mass flow controler. The monomer was evaporated and mixed with the Ar flow in the controlled evaporation and mixing system. Before turning the plasma on at the same monomer flow rate, the monomer gas and Ar flow in the reactor for 2 minutes in order to obtain an equilibrium between in- and out-flow of the gas. The treatment time was kept constant at 5 min and the applied power was varied. Only for deposition speed measurements, the treatment time was changed.

After plasma treatment, the monomer and Ar flow were stopped and the reactor was pumped down to <0.5 mbar before letting ambient air enter the system and removing the sample.

B.3 Electrical characterization

To electrically characterize the DBD, the applied high voltage and the resultant discharge current of the plasma reactor were measured. The high voltage applied to the lower copper electrode was measured using a 1000:1 high voltage probe (Tektronix P6015A). The discharge current was measured by measuring the voltage across a 50 Ω resistor connected in series with the reactor to the ground. Via Ohm's law, the discharge current was calculated. The obtained waveforms were recorded using a digital oscilloscope (Picoscope 3204A) and were visualized and analyzed using the included software (Picoscope 6).[133]

To calculate the discharge power, an integration of the instantaneous power p(t) was performed over a number of periods n, as indicated in formula (B.1).

$$P_{avg} = \int_0^{nT} p(t)dt = \int_0^{nT} v(t).i(t)dt \tag{B.1}$$

As the discharge current and voltage waveforms were discrete datasets, the trapezoidal rule was used as discrete integration method. This method is graphically illustrated in figure B.2.

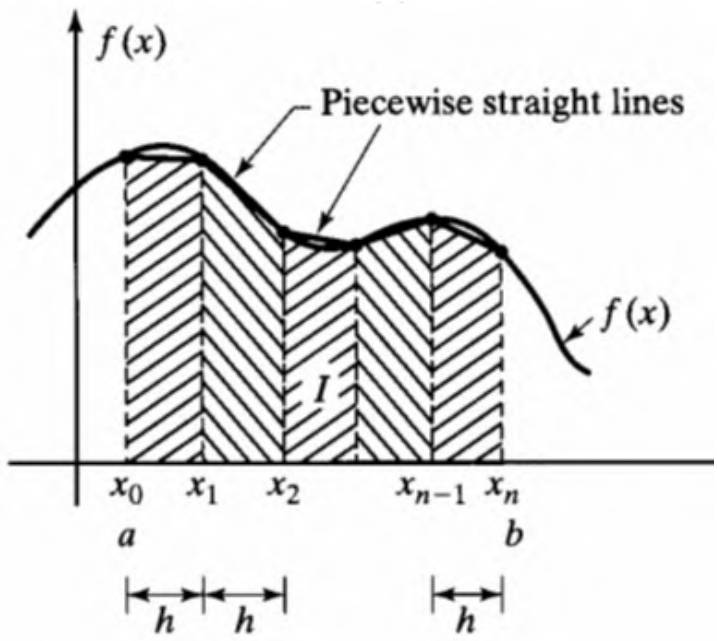

Figure B.2: The integral $= \int_a^b f(x)dx$ can be approximated by the sum of the areas of the trapeziods indicated by the diagonal stripes.[134]

By using the trapezoidal rule, the integral can be approximated by the following expression [134]:

$$\int_a^b f(x)dx = \frac{h}{2}.(f(x_0) + f(x_n) + 2.\sum_{i=1}^{n-1} f_i) \tag{B.2}$$

A Matlab ® code was written in which the boundaries of the integration are set manually. Then, this expression was used to calculate the average discharge power. An integration over 19 ± 1 periods for the pulsed power was performed.

For the assessment of the difference in duty cycle for the different monomers, 4 recorded waveforms for each monomer were selected and 2 measurements of 'on'- and 'off' periods per waveform were taken. The waveforms were selected to have a calculated average power in between 40 W and 20 W, in order to clearly distinguish the 'on'- and 'off'-periods.

B.4 Surface characterization methods

Different characterization methods have been used in this thesis. In this section, all different characterization methods are described. In the following sections, their specific purpose is explained.

B.4.1 Water contact angle measurement

Contact angle measurements quantify the wettability of a surface by a liquid. As shown in figure B.3, the contact angle is formed between the solid/liquid interface and the liquid/vapor interface. [135] In this thesis, deionized water was used as liquid ($< 1\mu S/cm^3$). Then, hydrophilic surfaces will have water contact angles lower that 90°, while hydrophobic surfaces have water contact angles higher than 90°.

Static water contact angles were measured for the plasma treated samples. This is a measurement of the contact angle shortly after its formation, when the solid, liquid and gas phase are in equilibrium. The plasma treated sample was transferred to the measurement device (Krüss Easy Drop system (Krüss Gmbh, Germany)) immediately after treatment. The water contact angles were made by drops with a volume of 2 μL. All contact angles were measured within 10 minutes after the plasma treatment.

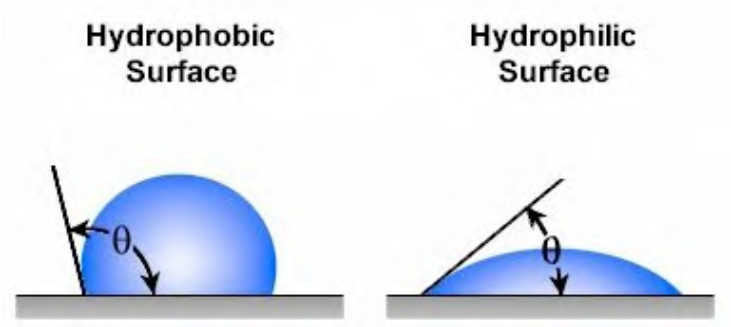

Figure B.3: Illustration of WCA measurement on a hydrophilic and hydrophobic surface. [135]

By initial measurements, it was observed that a large difference exists between water contact angles on the left and right side of the sample. In figure B.4, the sample on the electrode was divided in 9 equal parts of 1x1 cm^2. Based on this division, the WCA over the total sample were compared. At least two WCA measurements were performed in each

area for the demonstration of the changing water contact angle over the total surface.

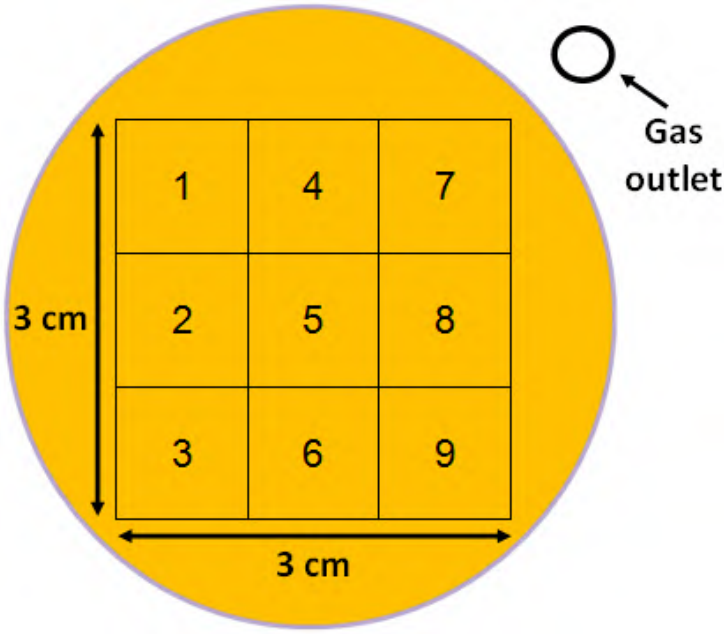

Figure B.4: Division of the sample surface in 9 equal parts.

Based on these observations, the WCA for different monomers and powers are compared for areas 7, 8 and 9. At least 8 WCAs were measured in these areas. No WCAs were measured on the XPS sample that was also taken on this side of the sample.

B.4.2 Fourier transform infrared spectroscopy

Fourier transform infrared spectroscopy (FT-IR) uses infrared light to analyze chemical structures. Sending radiation with different frequencies through a sample will result in absorption and transmission of certain light frequencies. Light will be absorbed when its frequency matches with vibrational frequencies of the molecules in the sample. So, the absorbed and transmitted light gives information on the molecular structures in the sample. As opposed to dispersive infrared spectroscopy which sequentially scans each frequency, FT-IR uses beams containing multiple frequencies. These beams are produced by an interferometer, which is a configuration of mirrors that splits radiation beams and recombines them after introducing a path difference in between this

beams. The resulting beam will depend on the interference of the different beams. [136] By changing the mirror configuration, different radiation beams are produced. The intensity of the transmitted beam is measured and related to the mirror configuration. This signal is then Fourier transformed to a resulting absorbance or transmittance spectrum in function of wavenumber or frequency.

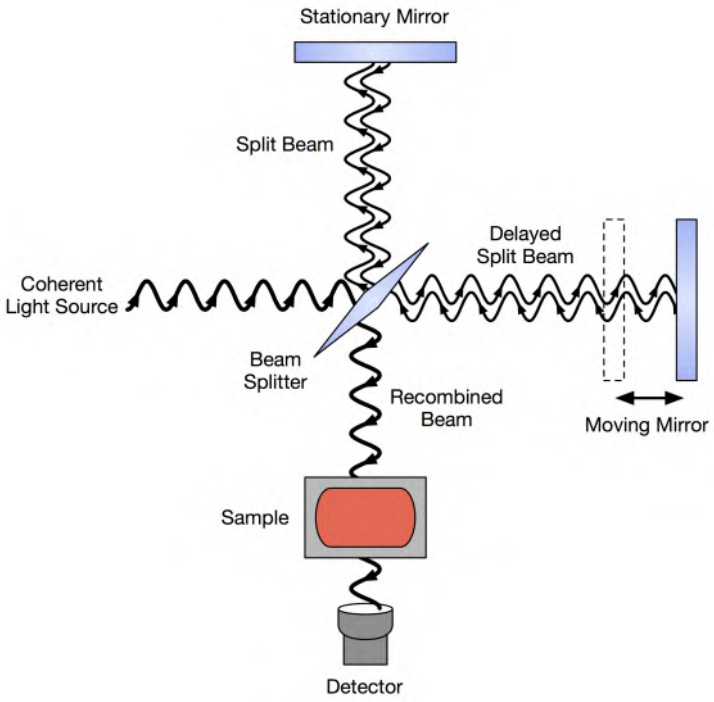

Figure B.5: Scheme of an interferometer. [137]

The used measurement equipment was a Bruker Tensor 27 spectrometer, with a liquid N_2 cooled MCT detector. Visualization of the spectra was performed with the included software (OPUS 7.0). Before each series of measurements, the sample holder was cleaned with isopropanol and a background signal was recorded to compensate for the environment. The software automatically performs this compensation. Between each measurement, the sample holder was also cleaned. For each measurement, 64 scans are made. The scan region was 4000-700 cm^{-1} with a resolution of 4 cm^{-1}. Each sample was supported with 0.25 mm of UHMWPE, in order to avoid piercing the sample. The book 'Infrared and Raman characteristic group Frequencies' was used for peak determination. [138]

B.4.3 X-ray photoelectron spectroscopy

X-ray photoelectron spectroscopy (XPS) is an established method for determining elemental composition and the chemical state of solid surfaces and thin films. [139] X-ray photons are focused on a sample, exciting electrons from the valence or core levels of the atoms into a vacuum. A high vacuum ($< 10^{-11}$ bar) is required to prevent interaction with background gas and contamination of the specimen surface. The kinetic energy of the excited electron, named photoelectron, is a measure of the electronic structure of the atom that interacted with the X-ray photon. In expression B.3, the kinetic energy E_{kin} of the photoelectron is expressed as the energy of the photon $\hbar.\omega$, the work function of the material Φ_w and the binding energy with respect to the fermi level E_b.

$$E_{kin} = \hbar.\omega - \Phi_w - E_b \tag{B.3}$$

This is also illustrated in figure B.6.

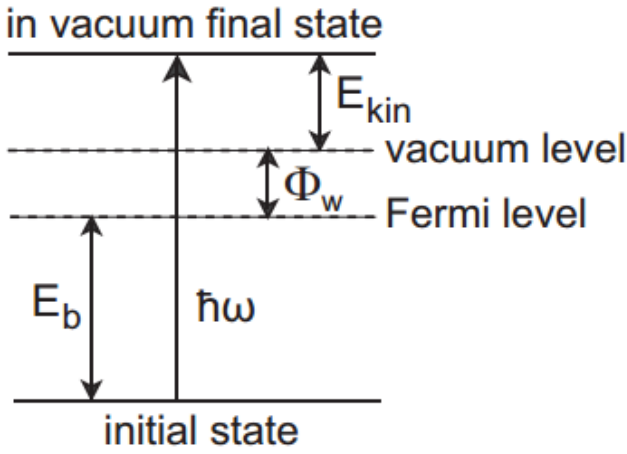

Figure B.6: Energy diagram for the photoelectron excitation. [139]

By using a monochromatic X-ray beam and measuring the kinetic energy of the photoelectron, the binding energy of the electrons in the irradiated atom can be calculated. This permits identification of this atom and provides information concerning its chemical state. Each electron orbital of an atom will have a characteristic binding energy. Presence of

photoelectrons with specific energies therefore relate to specific elements in the irradiated sample. The exact value of the binding energy depends also on the chemical environment of the atoms. Different environments result in small binding energy shifts, usually between a fraction of an eV and a few eV, which are called chemical shifts. These shifts can be used to distinguish between different chemical bonds of the atom.

To analyze the energy of the released photoelectrons, they are focused onto the entrance slit of an electrostatic analyzer by an electromagnetic lens system. Then, they pass through an hemispherical electron energy analyzer, as shown in figure B.7. This system consists of two concentrically arranged metallic hemispheres, whereto a potential difference is applied. [139] Only photoelectrons with a well-defined kinetic energy are able to complete their path through these hemispheres. With an electron multiplier, the amount of emitted photoelectrons of a certain energy is measured. This is converted to a signal in function of binding energy: by changes in the electromagnetic lens system, a spectrum is obtained with peaks that relate to the chemical composition of the sample. This spectrum only relates to the top layer of the sample (5-10 nm), as photoelectrons originating from deeper layers lose energy through collisions with the sample surface.

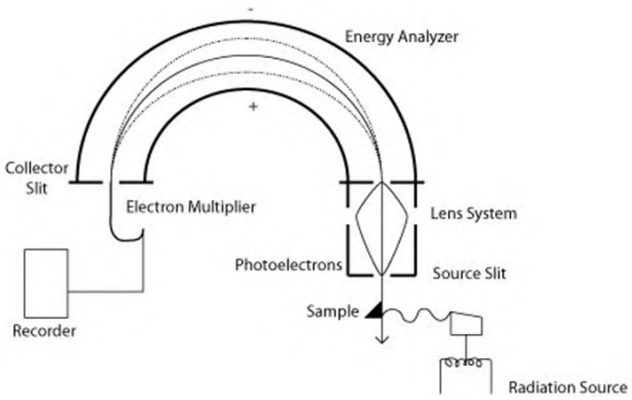

Figure B.7: Scheme of an XPS set-up.[140]

In this thesis, a PHI 5000 Versaprobe II spectrometer XPS was used for the surface analysis of the samples. This equipment uses a monochromatic Al K_α X-ray source ($\hbar.\omega$ = 1486.6 eV) operating at 23.3 W. A vacuum of at least 10^{-11} bar was obtained for all measurements. The hemispherical analyzer was positioned at an angle of 45° with respect to the normal of the sample surface. For each sample, at least 4 measurement points were taken on the sample.

For each point, a survey scan was measured. This is an XPS spectrum with a wide energy range, in order to determine the elemental composition of the sample. The area under the energy peaks is proportional to the relative amount of the element within the analyzed point of the sample surface. The region for this scan ranged from 0-1100 eV with a pass energy of 187.85 eV and an eV-step of 0.8 eV. The elemental composition was determined by using Multipak software, which automatically corrects for the different sensitivity of the atoms towards the photo-electron emission. 0.314 and 58.632 (C1s), 0.499 and 93.279 (N1s), 0.733 and 137.170 (O1s) are respectively the relative and corrected relative sensitivity factors.

For the same point, individual high resolution spectra were measured for C1s, O1s and N1s energies. These spectra can be used for analyzing the different bonds the atom has formed in the sample. The ranges for these scans went $\pm$ 10 eV around the area of interest with a pass energy of 23.5 eV and an eV-step of 0.1 eV. Samples were taken in between area 7 and 8 of the sample, as shown in figure B.4. No WCA were measured on the piece that is used for XPS. For deconvolution of the C1s-peak, the following peak positions were chosen: 285 eV, 286.1 eV, 287.4 eV and 288.4 eV. A maximal deviation of 0.3 eV was allowed in both directions. The FWHM of the deconvolution peaks is limited in the range of 1.3-1.5 eV. These restrictions were based on the FWHM of the peak at 285 eV (carbon-carbon binding). For the deconvolution of N1s and O1s, one peak was fitted to the spectrum. Chi-squared values were analyzed to conclude only good fittings in the analysis.

B.4.4 Proton and carbon nuclear magnetic resonance

The principle of nuclear magnetic resonance is explained in section A.2. To use this technique as a characterization technique for the deposited coating, the same process as described in section B.2 is followed, but the activation step is not performed. Thereby, a more loosely attached coating as obtained. The right side of the sample, areas 7, 8 and 9 in figure B.4, are cut in small pieces. The pieces are brought in 1 mL of $CDCL_3$ and measured on a Bruker Avance II 500 MHz spectrometer at room temperature. After at least 4 days, the polypropylene pieces are removed and the plasma polymer in solution is analyzed.

B.5 Stability of coating

To assess the stability of the coatings, 3 samples of approximately 0.7 x 1 cm^2 were cut out of the areas 7, 8 and 9 (as shown in figure B.4) after WCA measurements were performed on the sample. One sample was not incubated in deionized water, while the other samples were incubated in deionized water for respectively three and seven days. An FT-IR measurement was performed on each sample as described in section B.4.2.

The absorbance of the infrared light at a certain wavelength traversing a medium is proportional to the concentration and length of the medium. [141] The absorbance spectrum is therefore a measure of the thickness of the media that the infrared light traverses. By taking the ratio of the area of an absorbance peak that is typical to the coating and an absorbance peak from the substrate and the supporting UHMWPE, a measure of the thickness of the coating is obtained. By comparing this ratio, the stability of the coating can be evaluated.

Two integration methods were used to asses the area under the absorbance peaks.

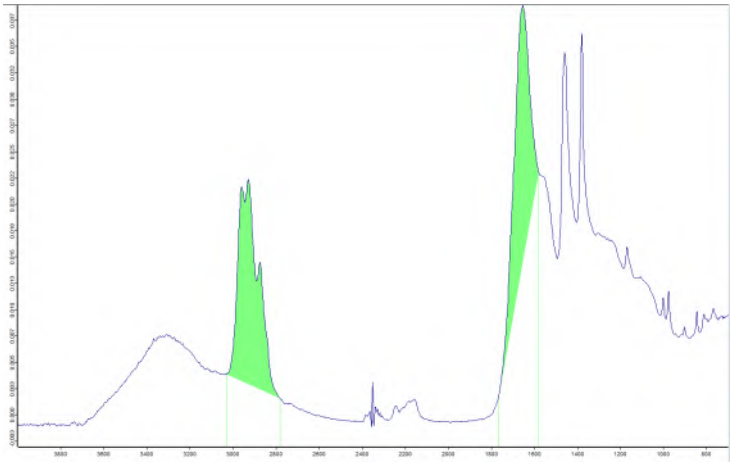

Figure B.8: Illustration of integration method 1.

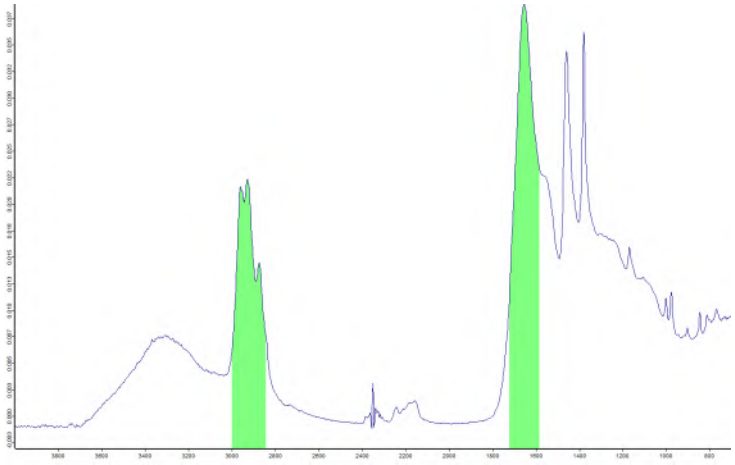

Figure B.9: Illustration of integration method 2.

To give an indication of the peak ratios and the corresponding FT-IR spectra, two examples are included. Figures B.10-B.11 give examples of peak ratios equal to ±1.3, ±1, ±0.8 and ±0.6. Examples of peak ratios equal to ±0.55, ±0.35 and ±0.15 are included in section 4.4. Together, these examples can be used as a reference to relate peak ratios to the corresponding FT-IR spectra.

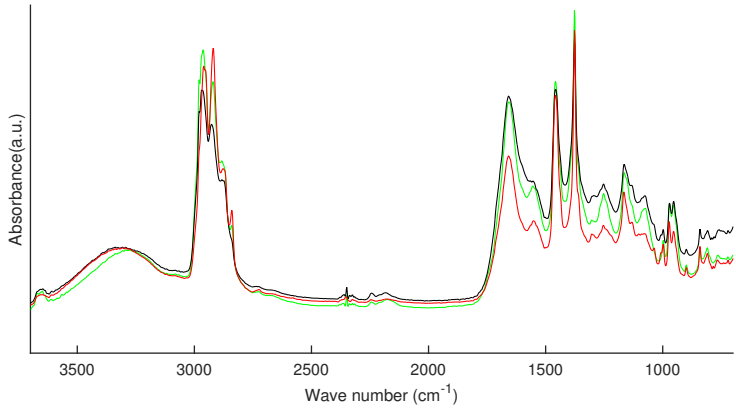

Figure B.10: Example of a FT-IR spectrum for 0 (green), 3 (black) and 7 (red) days for pPPrOx (P_{avg}=18 W). For 3 days of water incubation, peak ratios of 1.30 (method 1) and 1.30 (method 2) are obtained. For 7 days of water incubation, peak ratios of 0.82 (method 1) and 0.79 (method 2) are obtained.

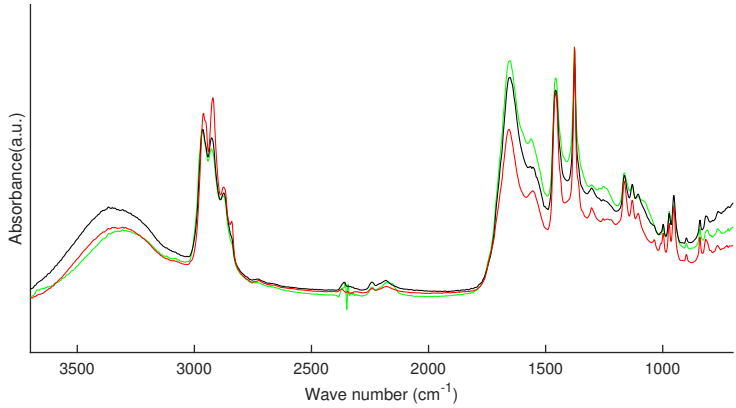

Figure B.11: Example of a FT-IR spectrum for 0 (green), 3 (black) and 7 (red) days for pPEtOx (P_{avg}=28 W). For 3 days of water incubation, peak ratios of 1.00 (method 1) and 0.90 (method 2) are obtained. For 7 days of water incubation, peak ratios of 0.65 (method 1) and 0.62 (method 2) are obtained.

B.6 Atomic force microscopy: deposition speed measurement

Atomic force microscopy is a technique to visualize surfaces. The principle is shown in figure B.12.A: a small tip is attached to a cantilever-type spring and deflections of the cantilever are measured with a laser and a segmented photodiode. The laser beam is reflected off the rear side of the cantilever. The intensity that each segment of the diode receives is a measure of the deflection of the cantilever. There are a number of different operation modes, as also indicated in figure B.12.

1. In contact mode, the tip is moved across the sample with a separation in the order of Å. The force exerted by the sample on the tip is kept constant by moving the cantilever or sample in a feedback loop. This movement is a measure of the height differences on the sample. Movement of the tip over the sample produces an image of the surface topography. This mode works at very small separations, to have a net repulsive force on the tip.[142] This mode can compromise the integrity of the sample surface, especially for soft surfaces.

2. In non-contact mode, the tip is oscillating with an amplitude of smaller than 10 nm, at or just above its resonance frequency. [143]

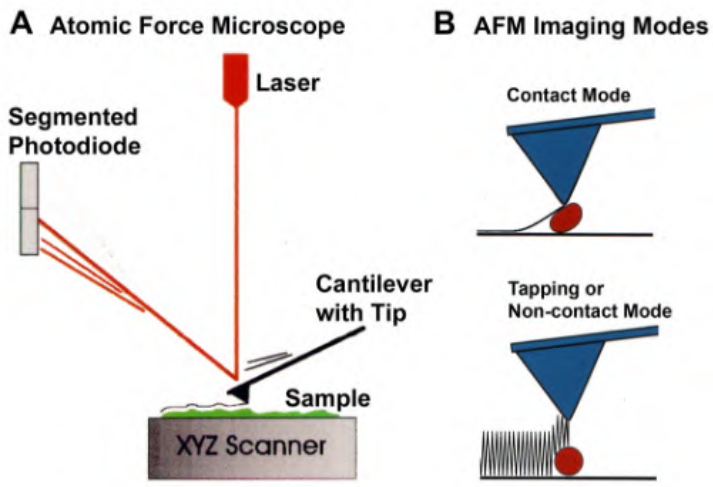

Figure B.12: A: Illustration of the working principle of an AFM. B: Illustration of the imaging modes of an AFM. [144]

If the cantilever is oscillating at its resonance frequency, another force of the surface will result in a slight change in resonance frequency. The original frequency is maintained by changing the average sample-to-tip distance with feedback loops. So, a similar image of the surface can be obtained. If the cantilever is oscillating just above the resonance frequency, then the amplitude of the oscillation is kept constant by a feedback loop.

3. In tapping mode, the tip is oscillating at or near its resonant frequency and it is made to strike the surface on each oscillation.[143] The oscillation amplitude is much larger than in non-contact mode, ranging from 20 to 100 nm. A feedback system adjusts for the change in oscillation amplitude by the contact with the surface, by adjusting the height of the tip. So, a constant amplitude is maintained. The variation in height generates a topographic image of the surface. [143]

AFM was used in this thesis for deposition speed measurements. All measurements were performed by an XE-70 atomic force microscope (Park Systems), used in non-contact mode with a silicon cantilever (Nanosensors^{TM} PPP-NCHR). Initial measurements were performed along the side of the sample: by removing the tape of each side, the thickness could be measured by measuring the step height with AFM. Scans of 45 x 45 μm^2 were performed randomly along this side of the

sample, so that the height step of the coating was in the middle of the scan image.

To quantify the difference in deposition speed of the monomers, a 3x3 cm^2 sample was placed in the plasma reactor. For each monomer, the thickness for the following treatment times and powers was measured as indicated in table B.1:

Table B.1: Treatment times and powers for deposition speed measurements.

	Power (W)	Treatment times (min)
pPMeOx	29.2 ± 0.7	5, 10, 20
	24.7	20
pPEtOx	27.1 ± 2.5	10, 15, 20
	20.6 ± 0.1	10, 15, 20
pPPrOx	29.3 ± 1.0	10, 15, 20
	20.9 ± 0.5	10, 15, 20
pPBuOx	29.8 ± 1.8	10, 15, 20
	19.2 ± 0.9	10, 15, 20

For prolonged measurements, the heating of the electrode caused loosening between the tape and sample, leading to tape residues that remained on the sample after tape removal. This made it difficult to measure everywhere on the sample. Therefore, the thickness was always measured along the upper 1 cm of the right side of the sample. Therefore, at least 10 scans of 45 x 45 μm^2 were performed randomly along this side of the sample, so that the height step of the coating was in the middle of the scan image. XEP software was used for analysis. To measure the thickness, a line profile was taken over the coating step, then, the non-coated side was leveled so that it was flat and at last, an average height difference was determined between the coated and non-coated part of the image. For each reported measurement, at least 10 measurement points of at least 4 samples were measured.

B.7 Non-fouling capacity of the coating

The samples that were made for the non-fouling capacity tests have a size of approximately 3.5 x 3.5 cm^2. The samples were cleaned with ethanol and dried with dry air before placement in the plasma reactor. The same process as described in B.2 was performed to deposit the

plasma coatings. For each monomer in chapter 4, samples were made at three different powers. To assess the power, the same method as discussed in section B.3 was used. To make all the samples for the anti-fouling tests for one power, multiple runs with the plasma reactor were required. The power for each condition was obtained by averaging all power measurements for each run. This is shown in table B.2. Also the standard deviations are included.

Table B.2: Powers for each monomer for anti-fouling capacity measurements.

pPMeOx	pPEtOx	pPrOx	pBuOx
33.2 $\pm$ 1.7 W	19.4 $\pm$ 0.7 W	22.3 $\pm$ 0.6 W	25.1 $\pm$ 1.0 W
41.2 $\pm$ 0.8 W	29.1 $\pm$ 0.7 W	29.8 $\pm$ 1.0 W	30.7 $\pm$ 1.1 W
47.5 $\pm$ 1.3 W	36.4 $\pm$ 0.5 W	40.8 $\pm$ 0.3 W	40.6 $\pm$ 0.6 W

To assess the stability of the coating, water contact angle measurements were performed over the whole sample. The part of the sample with water contact angles corresponding to 'stable' coatings is isolated and incubated for 21 hours at room temperature to remove loosely bond coating particles.

B.7.1 Anti-fouling capacity of the coating

B.7.1.1 Cell tests

For the cell tests, the remainder of the samples (with good WCA and after incubation) were cut in parts of approximately 0.9 x 0.9 cm^2. These samples were placed in a 24-well plate and fixated with a rubber ring of 11 mm inner diameter.

Cell culture

The samples were sterilized by exposure to UV light (λ = 254 nm) for 30 min. Human foreskin fibroblasts (HFF) were seeded onto samples in a 24-well plate at a density of 10.000 cells/1000 μL of medium per each. Cell culturing was performed using a Dulbecco's Modified Eagle's medium (DMEM) glutamax medium (Gibco Invitrogen) with 15% fetal calf serum (Gibco Invitrogen), 2 mM L-glutamine (Sigma-Aldrich), 10 U/mL penicillin, 10 mg/mL streptomycin and 100 mM sodium-pyruvate (all from Gibco Invitrogen). The cultures were incubated at 37°C under 5% CO_2 for 1 and 3 days (time required for human foreskin fibroblasts to adhere and proliferate on surfaces). Cell proliferation and viability

was measured for 1 and 3 days and tissue culture polystyrene (TCPS) was collected as a positive control.

Live and dead immune microscopy

Live/dead cell staining was used to evaluate cell viability. After 1 and 3 day of seeding, the cells were incubated in 2 μL (1 mg/mL) of calcein-AM and 2 μL (1mg/mL) propidium iodide in 1 mL of phosphate-buffered saline (PBS) for 10 min at room temperature, rinsed twice with PBS solution and then imaged with a fluorescence microscope (Olympus; IX 81) with appropriate filters.

Cell proliferation

Cell response to the samples was assessed by cell proliferation and viability (mitochondrial activity). Cell viability was measured after 1 and 3 day of HFF culture by replacing the culture medium by 0.5 mL (0.5 mg/mL) 3-[4,5-dimethylthiazol-2-yl]-2,5-diphenyl tetrazolium bromide (MTT) reagent. The samples were incubated at 37°C for 4 h in MTT solution. Mitochondrial dehydrogenase enzymes of viable cells reduced the tetrazolium ring to purple formazan crystals. The formazan crystals were dissolved in a lysis buffer (1% Triton-X100 in isopropanol/ 0.04 N HCl) for 30 min, then 200 μL of this solution was transferred to a 96-well plate and the optical density (OD) was measured at 580 nm using a spectrophotometer (BioTek; USA). Background absorbance at 750 nm was subtracted from the measured absorbance. For each day, 3 samples were used.

B.7.1.2 Bacterial adhesion tests

For the bacterial adhesion tests, the remainder of the samples (with good contact angle and after incubation) were cut in parts of approximately 1 x 2 cm^2. Two samples were glued together with superglue (Loctite 406+770) and the samples were pressed together. Loctite 406 is a glue based on ethyl-cyanoacrylate, which shows mainly a bactericidal effect towards gram positive bacteria. [145] After 48 hours, the sample was cut in 2 parts of 0.6 x 0.6 cm^2. For each condition, 4 glued samples were tested for each microorganism. For pPEtOx, the samples were not glued together. These samples were therefore coated only at one side. Also 4 samples were tested for each microorganism.

Before the assay, all samples were sterilized by a 30 minutes UV exposure. The microorganisms were grown on Tryptic Soy Agar (TSA) (Oxoid, Drongen, Belgium) (*P. aeruginosa* and *S. aureus*) under aerobic conditions at 37°C. Using a sterile forceps, the samples were placed in the wells of a 24-well microtiter plate and subsequently 1 mL of the cell suspension, containing approx. 10^4 colony forming units (CFU)/mL was added. The plates were incubated for 4 h at 37 °C. Following incubation, the samples were transferred to 10 mL 0.9% (w/v) NaCl and subjected to three cycles of 30 s vortex mixing and 30 s sonication. Tenfold serial dilutions were made in 0.9% (w/v) NaCl and the number of CFU was determined by plate counting. To this end, one mL of each dilution was plated on TSA and the plates were incubated at 37°C for 48 h.

Bibliography

[1] U.S. Food and drug administration. Implants and Prosthetics. http://www.fda.gov/MedicalDevices/ProductsandMedical Procedures/ImplantsandProsthetics/. Date of last access: 2017-02-02, 2015.

[2] Allen; Baxter. The Eleven Most Implanted Medical Devices In America, 2011.

[3] Transparancy market Research. Implantable Medical Devices Market - Global Industry Analysis, Size, Share, Growth, Trends, and Forecast, 2016 - 2024, 2016.

[4] W J Hu, J W Eaton, T P Ugarova, and L P Tang. Molecular basis of biomaterial-mediated foreign body reactions. *Blood*, 98(4):1231–1238, 2001.

[5] M. Khan, K. Osman, G. Green, and F. S. Haddad. The epidemiology of failure in total knee arthroplasty: avoiding your next revision. *The bone & joint journal*, 98-B(1):105–112, 2016.

[6] Steven Kurtz, Kevin Ong, Edmund Lau, Fionna Mowat, and Michael Halpern. Projections of primary and revision hip and knee arthroplasty in the United States from 2005 to 2030. *The Journal of bone and joint surgery. American volume*, 89:780–785, 2007.

[7] Murray J. Penner, Sulaiman A. Almousa, and Lee Kolla. Aseptic loosening. In *Total Ankle Replacement: An Operative Manual*, pages 116–122. 2014.

[8] Kevin J. Bozic, Steven M. Kurtz, Edmund Lau, Kevin Ong, Vanessa Chiu, Thomas P. Vail, Harry E. Rubash, and Daniel J. Berry. The epidemiology of revision total knee arthroplasty in

the united states. *Clinical Orthopaedics and Related Research*, 468(1):45–51, 2010.

[9] David F. Williams. On the mechanisms of biocompatibility. *Biomaterials*, 29(20):2941–2953, 2008.

[10] Ahyeon Koh, Scott P. Nichols, and Mark H. Schoenfisch. Glucose Sensor Membranes for Mitigating the Foreign Body Response. *Journal of Diabetes Science and Technology*, 5(5):1052–1059, 2011.

[11] David F. Williams. There is no such thing as a biocompatible material. *Biomaterials*, 35(38):10009–10014, 2014.

[12] James M. Anderson. Biological Responses to Materials. *Annu. Rev. Mater. Res.*, 31:81–110, 2001.

[13] James M. Anderson, Analiz Rodriguez, and David T. Chang. Foreign body reaction to biomaterials. *Seminars in Immunology*, 20(2):86–100, 2008.

[14] M Paulsson. Basement membrane proteins: structure, assembly, and cellular interactions. *Critical reviews in biochemistry and molecular biology*, 27(1-2):93–127, 1992.

[15] G Daniel Boon. An Overview of Hemostasis. *Toxicologic pathology*, 21:170–179, 1993.

[16] U Amara, D Rittirsch, M Flierl, U Bruckner, A Klos, F Gebhard, J D Lambris, and M Huber-Lang. Interaction between the coagulation and complement system. *Advances in Experimental Medicine and Biology*, 632(Davis 2004):71–79, 2008.

[17] José Rivera, María Luisa Lozano, Leyre Navarro-núñez, and Vicente Vicente. Platelet receptors and signaling in the dynamics of thrombus formation. *Haematologica*, 94(Figure 1):700–711, 2009.

[18] I. H. Jaffer, J. C. Fredenburgh, J. Hirsh, and J. I. Weitz. Medical device-induced thrombosis: What causes it and how can we prevent it? *Journal of Thrombosis and Haemostasis*, 13(S1):S72–S81, 2015.

[19] L Vroman, A. L. Adams, G. C. Fischer, and P. C. Munoz. Interaction of high molecular weight kininogen, Factor XII and fibrinogen in plasma at interfaces. *Blood Journal*, 55(1):156–159, 1980.

[20] P. N. Nesargikar, B. Spiller, and R. Chavez. The complement system: history, pathways, cascade and inhibitors. *European Journal of Microbiology & Immunology*, 2(2):103–111, 2012.

[21] Richard O. Hynes. Integrins: Bidirectional, allosteric signaling machines. *Cell*, 110(6):673–687, 2002.

[22] G Berton and Lowell CA. Integrin signalling in neutrophils and macrophages. *Cell Signal*, 11(9):621–35, 1999.

[23] Paul Martin and S. Joseph Leibovich. Inflammatory cells during wound repair: The good, the bad and the ugly. *Trends in Cell Biology*, 15(11):599–607, 2005.

[24] Domenico Ribatti and Enrico Crivellato. "Sprouting angiogenesis", a reappraisal. *Developmental Biology*, 372(2):157–165, 2012.

[25] Shibnath Ghatak, Edward V. Maytin, Judith A. MacK, Vincent C. Hascall, Ilia Atanelishvili, Ricardo Moreno Rodriguez, Roger R. Markwald, and Suniti Misra. Roles of Proteoglycans and Glycosaminoglycans in Wound Healing and Fibrosis. *International Journal of Cell Biology*, pages 1–20, 2015.

[26] M; Félétou. Multiple Functions of the Endothelial Cells. In *The Endothelium: Part 1: Multiple Functions of the Endothelial Cells—Focus on Endothelium-Derived Vasoactive Mediators.*, chapter 2. 2011.

[27] Thomas F. Lüscher, Jan Steffel, Franz R. Eberli, Michael Joner, Gaku Nakazawa, Felix C. Tanner, and Renu Virmani. Drug-eluting stent and coronary thrombosis: Biological mechanisms and clinical implications. *Circulation*, 115(8):1051–1058, 2007.

[28] JW Costerton, L Montanaro, and CR Arciola. Biofilm in implant infections: Its production and regulation. *International journal of artificial organs*, 28(11):1062–1068, 2005.

[29] Venkatesan Nandakumar, Samuel Chittaranjan, Valikappathalil Mathew Kurian, and Mukesh Doble. Characteristics of bacterial biofilm associated with implant material in clinical practice. *Polymer Journal*, 45(2):137–152, 2013.

[30] A Simon Lynch and Gregory T Robertson. Bacterial and Fungal Biofilm Infections. *Annual Review of Medicine*, 59(1):415–428, 2008.

[31] David M Higgins, Randall J Basaraba, April C Hohnbaum, Eric J Lee, David W Grainger, and Mercedes Gonzalez-Juarrero. Localized immunosuppressive environment in the foreign body response to implanted biomaterials. *The American journal of pathology*, 175(1):161–170, 2009.

[32] J. M. Schierholz and J. Beuth. Implant infections: A haven for opportunistic bacteria. *Journal of Hospital Infection*, 49(2):87–93, 2001.

[33] Brain Waggoner, Ben; Speer. Bacteria: Life History and Ecology. http://www.ucmp.berkeley.edu/bacteria/bacterialh.html. Date of last access: 20/12/2016.

[34] Kenneth Todar. The Normal Bacterial Flora of Humans. http://www.textbookofbacteriology.net/normalflora_3.html. Date of last access: 12/11/2016, 2008.

[35] Suganthan Veerachamy, Tejasri Yarlagadda, Geetha Manivasagam, and Prasad Kdv Yarlagadda. Bacterial adherence and biofilm formation on medical implants: a review. *Proceedings of the Institution of Mechanical Engineers. Part H, Journal of engineering in medicine*, 228(10):1083–99, 2014.

[36] Stephen J McConoughey, Rob Howlin, Jeff F Granger, Maurice M Manring, Jason H Calhoun, Mark Shirtliff, Sandeep Kathju, and Paul Stoodley. Biofilms in periprosthetic orthopedic infections. *Future microbiology*, 9(8):987–1007, 2014.

[37] M. Katsikogianni and Y. F. Missirlis. Concise review of mechanisms of bacterial adhesion to biomaterials and of techniques used in estimating bacteria-material interactions. *European Cells and Materials*, 8:37–57, 2004.

[38] B. Gottenbos, H. J. Busscher, H. C. Van Der Mei, and P. Nieuwenhuis. Pathogenesis and prevention of biomaterial centered infections. *Journal of Materials Science: Materials in Medicine*, 13(8):717–722, 2002.

[39] Carla Renata Arciola, Davide Campoccia, Garth D Ehrlich, and Lucio Montanaro. Biofilm-based Healthcare-associated Infections. *Advances in Experimental Medicine and Biology*, 1:29–46, 2015.

[40] Jessica L Lister and Alexander R Horswill. Staphylococcus aureus biofilms: recent developments in biofilm dispersal. *Frontiers in cellular and infection microbiology*, 4(December):178, 2014.

[41] G S Baillie and L J Douglas. Matrix polymers of Candida biofilms and their possible role in biofilm resistance to antifungal agents. *The Journal of Antimicrobial Chemotherapy*, 46(3):397–403, 2000.

[42] E. Costerton, J; Stewart, P: Greenberg. Bacterial biofilms: a common cause of persistent infections. *Science*, 284:1318–1322, 1999.

[43] G; Habash, M; Reid. Microbial biofilms: their devel- opment and significance for medical device-related infections. *J Clin Pharmacol*, 39(9):887–898, 1999.

[44] Li Chen and Yu-mei Wen. The role of bacterial biofilm in persistent infections and control strategies. *International Journal of Oral Science*, 3(2):66–73, 2011.

[45] Yde ; Engelsma, Pieter; Buma, and Arthur; Van Noort. Septic failure is not a septic loosening: A case report of a failed shoulder prosthesis. *International Journal of Shoulder Surgery*, 6(4):121–125, 2012.

[46] Thien Fah C Mah and George A. O'Toole. Mechanisms of biofilm resistance to antimicrobial agents. *Trends in Microbiology*, 9(1):34–39, 2001.

[47] Hong Wu, Claus Moser, Heng-Zhuang Wang, Niels Høiby, and Zhi-Jun Song. Strategies for combating bacterial biofilm infections. *International Journal of Oral Science*, 7(July 2014):1–7, 2015.

[48] Tim Tolker-Nielsen. Pseudomonas aeruginosa biofilm infections: From molecular biofilm biology to new treatment possibilities. *Apmis*, 122(s138):1–51, 2014.

[49] A Rotern. Effect Implant Material Properties on the Performance of a hip joint replacement. *Journal of Medical Engineering & Technology*, 18(6):208–217, 1994.

[50] Ahmed M Ballo, Omar Omar, Wei Xia, and Anders Palmquist. Dental Implant Surfaces - Physicochemical Properties, Biological Performance, and Trends. *Implant Dentistry - A rapidly Evolving Practice*, pages 19–57, 2001.

[51] K. Bazaka, M. V. Jacob, W. Chrzanowski, and K. Ostrikov. Anti-bacterial surfaces: natural agents, mechanisms of action, and plasma surface modification. *RSC Advances*, 5(60):48739–48759, 2015.

[52] Eric Alexander Lewallen, Scott M Riester, Carolina A Bonin, Hilal Maradit Kremers, Amel Dudakovic, Sanjeev Kakar, Robert C Cohen, Jennifer J Westendorf, David G Lewallen, and Andre J van Wijnen. Biological strategies for improved osseointegration and osteoinduction of porous metal orthopedic implants. *Tissue engineering. Part B, Reviews*, 21(2):218–30, 2015.

[53] Amanda W Bridges and Andrés J García. Anti-inflammatory polymeric coatings for implantable biomaterials and devices. *Journal of diabetes science and technology*, 2(6):984–94, 2008.

[54] Settimio; Pacelli, Vijayan; Manoharan, and Anna ; Desalvo. Tailoring biomaterial surface properties to modulate host- implant interactions: implication in cardiovascular and bone therapy. *Journal of Materials Chemistry. B, Materials for Biology and Medicine*, 150(4):1586–1599, 2016.

[55] Bill G X Zhang, Damian E. Myers, Gordon G. Wallace, Milan Brandt, and Peter F M Choong. Bioactive coatings for orthopaedic implants-recent trends in development of implant coatings. *International Journal of Molecular Sciences*, 15(7):11878–11921, 2014.

[56] Shuichi Eto, Shunsuke Kawano, Shinsuke Someya, Hiroshi Miyamoto, Motoki Sonohata, and Masaaki Mawatari. First Clinical Experience With Thermal-Sprayed Silver Oxide-Containing Hydroxyapatite Coating Implant. *Journal of Arthroplasty*, 31(7):1498–1503, 2016.

[57] Jiri Gallo, Martin Holinka, and Calin S Moucha. *Antibacterial Surface Treatment for Orthopaedic Implants*. 2014.

[58] M Cloutier, D Mantovani, and F Rosei. Antibacterial Coatings : Challenges , Perspectives , and Opportunities. *Trends in Biotechnology*, pages 1–16, 2015.

[59] M; Shen, Y; Pan, MS; Wagner, KD; Hauch, DG; Castne, BD; Ratner, and TA; Horbett. Inhibition of monocyte adhesion and fibrinogen adsorption on glow discharge plasma deposited tetraethylene glycol dimethyl ether. *Journal of Biomaterials Science, Polymer Edition*, 12(9):961–78, 2001.

[60] Lei Zhang, Zhiqiang Cao, Tao Bai, Louisa Carr, Jean-Rene Ella-Menye, Colleen Irvin, Buddy D Ratner, and Shaoyi Jiang. Zwitterionic hydrogels implanted in mice resist the foreign-body reaction. *Nature biotechnology*, 31(6):553–6, 2013.

[61] Robert G Chapman, Emanuele Ostuni, Michael N Liang, Gloria Meluleni, Enoch Kim, Lin Yan, Gerald Pier, H Shaw Warren, and George M Whitesides. Polymeric Thin Films That Resist the Adsorption of Proteins and the Adhesion of Bacteria. *Langmuir*, 17(4):1225–1233, 2001.

[62] G. Ene, A. Garcia Raso, A. Gonzalez-Dominguez Weber, A. Hidalgo-Vega, and P. Llamas. Cost of vitamin K antagonist anticoagulant treatment in patients with metallic prosthetic valve in mitral position. *SAGE Open Medicine*, 4(0), 2016.

[63] Robert W Emery, Christopher C Krogh, Kit V Arom, Ann M Emery, Kathy Benyo-Albrecht, Lyle D Joyce, and Demetre M Nicoloff. The St. Jude Medical cardiac valve prosthesis: a 25-year experience with single valve replacement. *The Annals of thoracic surgery*, 79(3):776–82; discussion 782–3, 2005.

[64] Michael J. Paidas, D. H W Ku, B. Davis, C. J. Lockwood, and Y. S. Arkel. Soluble monocyte cluster domain 163, a new global marker of anti-inflammatory response, is elevated in the first trimester of pregnancy [2]. *Journal of Thrombosis and Haemostasis*, 2(6):1009–1010, 2004.

[65] Indrani Banerjee, Ravindra C. Pangule, and Ravi S. Kane. Antifouling coatings: Recent developments in the design of surfaces that prevent fouling by proteins, bacteria, and marine organisms. *Advanced Materials*, 23(6):690–718, 2011.

[66] Davide Campoccia, Lucio Montanaro, and Carla Renata. Biomaterials A review of the biomaterials technologies for infection-resistant surfaces. *Biomaterials*, 34(34):8533–8554, 2013.

[67] R. R. ; Maddikeri, S. ; Tosatti, M.; Schuler, M.; Chessari, S.; Textor, R. G.; Richards, and L. G. ; Harris. Reduced medical infection related bacterial strains adhesion on bioactive RGD modified titanium surfaces: A first step toward cell selective surfaces. *Journal of Biomedical Materials Research Part A*, 84(2):425–435, 2008.

[68] L. G. Harris, S. Tosatti, M. Wieland, M. Textor, and R. G. Richards. Staphylococcus aureus adhesion to titanium oxide surfaces coated with non-functionalized and peptide-functionalized poly(L-lysine)-grafted- poly(ethylene glycol) copolymers. *Biomaterials*, 25(18):4135–4148, 2004.

[69] Guruprakash Subbiahdoss, Roel Kuijer, Dirk W. Grijpma, Henny C. van der Mei, and Henk J. Busscher. Microbial biofilm growth vs. tissue integration: "The race for the surface" experimentally studied. *Acta Biomaterialia*, 5(5):1399–1404, 2009.

[70] Rupert Konradi, Canet Acikgoz, and Marcus Textor. Polyoxazolines for nonfouling surface coatings - A direct comparison to the gold standard PEG. *Macromolecular Rapid Communications*, 33(19):1663–1676, 2012.

[71] Sean Lowe, Neil M O'Brien-Simpson, and Luke A Connal. Antibiofouling polymer interfaces: poly(ethylene glycol) and other promising candidates. *Polymer Chemistry*, 6(2):198–212, 2015.

[72] K H Aaron Lau, Chunlai Ren, Sung Hyun Park, Igal Szleifer, and Phillip B Messersmith. An Experimental - Theoretical Analysis of Protein Adsorption on Peptidomimetic Polymer Brushes. *Langmuir*, 28(4):2288–2298, 2012.

[73] Wetra Yandi, Sophie Mieszkin, Pierre Martin-Tanchereau, Maureen E. Callow, James A. Callow, Lyndsey Tyson, Bo Liedberg, and Thomas Ederth. Hydration and chain entanglement determines the optimum thickness of poly(HEMA-co-PEG10MA) brushes for effective resistance to settlement and adhesion of marine fouling organisms. *ACS Applied Materials and Interfaces*, 6(14):11448–11458, 2014.

[74] Chao Zhao, Lingyan Li, Qiuming Wang, Qiuming Yu, and Jie Zheng. Effect of film thickness on the antifouling performance of poly(hydroxy-functional methacrylates) grafted surfaces. *Langmuir*, 27(8):4906–4913, 2011.

[75] Ângela Serrano, Olof Sterner, Sophie Mieszkin, Stefan Zürcher, Samuele Tosatti, Maureen E. Callow, James A. Callow, and Nicholas D. Spencer. Nonfouling response of hydrophilic uncharged polymers. *Advanced Functional Materials*, 23(46):5706–5718, 2013.

[76] Yichuan Hu, Bo Liang, Lu Fang, Guanglong Ma, Guang Yang, Qin Zhu, Shengfu Chen, and Xuesong Ye. Antifouling Zwitterionic Coating via Electrochemically Mediated Atom Transfer Radical Polymerization on Enzyme-Based Glucose Sensors for Long-Time Stability in 37 °c Serum. *Langmuir*, 32(45):11763–11770, 2016.

[77] Zohreh Amoozgar and Yoon Yeo. Recent advances in stealth coating of nanoparticle drug delivery systems. *Wiley Interdisciplinary Reviews: Nanomedicine and Nanobiotechnology*, 4(2):219–233, 2012.

[78] Victor R. De La Rosa. Poly(2-oxazoline)s as materials for biomedical applications. *Journal of Materials Science: Materials in Medicine*, 25(5):1211–1225, 2014.

[79] Stefano Salmaso and Paolo Caliceti. Stealth Properties to Improve Therapeutic Efficacy of Drug Nanocarriers. *Journal of Drug Delivery*, 2013:1–19, 2013.

[80] Richard Hoogenboom. Poly(2-oxazoline)s: A polymer class with numerous potential applications. *Angewandte Chemie - International Edition*, 48(43):7978–7994, 2009.

[81] Rupert Konradi, Bidhari Pidhatika, Andreas Mühlebach, and Marcus Textor. Poly-2-methyl-2-oxazoline: A peptide-like polymer for protein-repellent surfaces. *Langmuir*, 24(3):613–616, 2008.

[82] Mark A. Ward and Theoni K. Georgiou. Thermoresponsive polymers for biomedical applications. *Polymers*, 3(3):1215–1242, 2011.

[83] Giulia Morgese and Edmondo M. Benetti. Polyoxazoline biointerfaces by surface grafting. *European Polymer Journal*, pages 1–35, 2016.

[84] Lutz Tauhardt, Marion Frant, David Pretzel, Matthias Hartlieb, Christian Bücher, Gerhard Hildebrand, Bernd Schröter, Christine Weber, Kristian Kempe, Michael Gottschaldt, Klaus Liefeith, and Ulrich S. Schubert. Amine end-functionalized poly(2-ethyl-2-oxazoline) as promising coating material for antifouling applications. *Journal of Materials Chemistry B*, 2(30):4883, 2014.

[85] Bidhari Pidhatika, Mathias Rodenstein, Yin Chen, Ekaterina Rakhmatullina, Andreas Mühlebach, Canet Acikgöz, Marcus Textor, and Rupert Konradi. Comparative stability studies of Poly(2-methyl-2-oxazoline) and Poly(ethylene glycol) brush coatings. *Biointerphases*, 7(1):1–15, 2012.

[86] Hongbin Zhang and Mu Chiao. Anti-fouling coatings of poly(dimethylsiloxane) devices for biological and biomedical applications. *Journal of Medical and Biological Engineering*, 35(2):143–155, 2015.

[87] Fraunhofer Institute for Interfacial Engineering and Biotechnology. Plasma Technology – Key Technology for the Production. https://www.igb.fraunhofer.de/content/dam/igb/en/documents/brochures/GTM/1704_BR-gtm_plasmatechnik_en.pdf. Date of last access: 01/06/2017.

[88] M. N. Ramiasa, A. A. Cavallaro, A. Mierczynska, S. N. Christo, J. M. Gleadle, J. D. Hayball, and K. Vasilev. Plasma polymerised polyoxazoline thin films for biomedical applications. *Chem. Commun.*, 51(20):4279–4282, 2015.

[89] Melanie N. Macgregor-Ramiasa, Alex a. Cavallaro, and Krasimir Vasilev. Properties and reactivity of polyoxazoline plasma polymer films. *J. Mater. Chem. B*, 3(30):6327–6337, 2015.

[90] H Conrads and M Schmidt. Plasma generation and plasma sources. *Plasma Sources Science and Technology*, 9(4):441–454, 2000.

[91] Tim Desmet, Rino Morent, Nathalie De Geyter, Christophe Leys, Etienne Schacht, and Peter Dubruel. Nonthermal plasma technology as a versatile strategy for polymeric biomaterials surface modification: A review. *Biomacromolecules*, 10(9):2351–2378, 2009.

[92] P Chu. Plasma-surface modification of biomaterials. *Materials Science and Engineering: R: Reports*, 36(5-6):143–206, 2002.

[93] P. Cools, N. De Geyter, and R. Morent. *PLA enhanced via plasma technology: A review*. Number May 2016. 2014.

[94] N. N. Morgan. Atmospheric pressure dielectric barrier discharge chemical and biological applications. *International Journal of Physical Sciences*, 4(13):885–892, 2009.

[95] U Kogelschatz, B Eliasson, W Egli, U Kogelschatz, B Eliasson, and W Egli Dielectric-barrier Discharges Principle. Dielectric-Barrier Discharges . Principle and Applications. *Journal de Physique IV Colloque*, 07(C4):C4–47–C4–66, 1997.

[96] Kim Shyong Siow, Leanne Britcher, Sunil Kumar, and Hans J. Griesser. Plasma methods for the generation of chemically reactive surfaces for biomolecule immobilization and cell colonization - A review. *Plasma Processes and Polymers*, 3(6-7):392–418, 2006.

[97] N. De Geyter, R. Morent, L. Gengembre, C. Leys, E. Payen, S. Van Vlierberghe, and E. Schacht. Increasing the hydrophobicity of a PP film using a helium/CF 4 DBD treatment at atmospheric pressure. *Plasma Chemistry and Plasma Processing*, 28(2):289–298, 2008.

[98] N. De Geyter, R. Morent, C. Leys, L. Gengembre, and E. Payen. Treatment of polymer films with a dielectric barrier discharge in air, helium and argon at medium pressure. *Surface and Coatings Technology*, 201(16-17):7066–7075, 2007.

[99] Rajesh Sharma, Edward Holcomb, Steve Trigwell, and Malay Mazumder. Stability of atmospheric-pressure plasma induced changes on polycarbonate surfaces. *Journal of Electrostatics*, 65(4):269–273, 2007.

[100] Richard M. France and Robert D. Short. Plasma treatment of polymers: the effects of energy transfer from an argon plasma on the surface chemistry of polystyrene, and polypropylene. A high-energy resolution X-ray photoelectron spectroscopy Study. *Langmuir*, 14(17):4827–4835, 1998.

[101] Vladimir Scholtz, Jarmila Pazlarova, Hana Souskova, Josef Khun, and Jaroslav Julak. Nonthermal plasma - A tool for decontamination and disinfection. *Biotechnology Advances*, 33(6):1108–1119, 2015.

[102] Pieter Cools, Nathalie De Geyter, Els Vanderleyden, Peter Dubruel, and Rino Morent. Surface analysis of titanium cleaning and activation processes: Non-thermal plasma versus other techniques. *Plasma Chemistry and Plasma Processing*, 34(4):917–932, 2014.

[103] A. G. Whittaker, E. M. Graham, R. L. Baxter, A. C. Jones, P. R. Richardson, G. Meek, G. A. Campbell, A. Aitken, and H. C. Baxter. Plasma cleaning of dental instruments. *Journal of Hospital Infection*, 56(1):37–41, 2004.

[104] Z. Zhang, R. Foerch, and W. Knoll. Surface modification by plasma polymerization and application of plasma polymers as biomaerials. *European Cells and Materials*, 6(SUPPL. 1):52, 2003.

[105] Jörg Friedrich. Mechanisms of plasma polymerization - Reviewed from a chemical point of view. *Plasma Processes and Polymers*, 8(9):783–802, 2011.

[106] Rino Morent, Nathalie De Geyter, Martine Trentesaux, Léon Gengembre, Peter Dubruel, Christophe Leys, and Edmond Payen. Stability study of polyacrylic acid films plasma-polymerized on polypropylene substrates at medium pressure. *Applied Surface Science*, 257(2):372–380, 2010.

[107] Ivan Gordeev, Andrei Choukourov, Milan Šimek, Václav Prukner, and Hynek Biederman. PEO-like plasma polymers prepared by atmospheric pressure surface dielectric barrier discharge. *Plasma Processes and Polymers*, 9(8):782–791, 2012.

[108] S Forster and S L Mcarthur. Stable low-fouling plasma polymer coatings on PDMS. *Biomicrofluidics*, 6(3):1–12, 2012.

[109] Mingchao Shen, Laura Martinson, Matthew S Wagner, David G Castner, Buddy D Ratner, and Thomas a Horbett. PEO-like plasma polymerized tetraglyme surface interactions with leukocytes and proteins: in vitro and in vivo studies. *Journal of biomaterials science. Polymer edition*, 13(4):367–90, 2002.

[110] Frédéric Brétagnol, Michaël Lejeune, Andri Papadopoulou-Bouraoui, Marina Hasiwa, Hubert Rauscher, Giacomo Ceccone, Pascal Colpo, and François Rossi. Fouling and non-fouling surfaces produced by plasma polymerization of ethylene oxide monomer. *Acta Biomaterialia*, 2(2):165–172, 2006.

[111] Agnes R. Denes, Eileen B. Somers, A. C L Wong, and Ferencz Denes. 12-Crown-4-Ether and Tri(Ethylene Glycol) Dimethyl-Ether Plasma-Coated Stainless Steel Surfaces and Their Ability To Reduce Bacterial Biofilm Deposition. *Journal of Applied Polymer Science*, 81(14):3425–3438, 2001.

[112] Erika E. Johnston, James D. Bryers, and Buddy D. Ratner. Plasma deposition and surface characterization of oligoglyme, dioxane, and crown ether nonfouling films. *Langmuir*, 21(3):870–881, 2005.

[113] K.R. Kamath, M.J. Danilich, R.E. Marchant, and K. Park. Platelet interactions with plasma-polymerized ethylene oxide and N-vinyl-2-pyrrolidone films and linear poly(ethylene oxide) layer. *Journal of Biomaterials Science, Polymer Edition*, 7(11):977–988, 1996.

[114] Thomas E. Andersen, Yaseelan Palarasah, Mikkel Ole Skjødt, Ryosuke Ogaki, Maike Benter, Mojagan Alei, Hans J. Kolmos,

Claus Koch, and Peter Kingshott. Decreased material-activation of the complement system using low-energy plasma polymerized poly(vinyl pyrrolidone) coatings. *Biomaterials*, 32(20):4481–4488, 2011.

[115] D Cökeliler, H Caner, J Zemek, a Choukourov, H Biederman, and M Mutlu. A plasma polymerization technique to overcome cerebrospinal fluid shunt infections. *Biomedical materials (Bristol, England)*, 2(1):39–47, 2007.

[116] Alex A. Cavallaro, Melanie N. MacGregor-Ramiasa, and Krasimir Vasilev. Antibiofouling Properties of Plasma-Deposited Oxazoline-Based Thin Films. *ACS Applied Materials and Interfaces*, 8(10):6354–6362, 2016.

[117] Sudhir Bhatt, Jêrome Pulpytel, Massoud Mirshahi, and Farzaneh Arefi-Khonsari. Cell Resistant Peptidomimetic Poly (2-ethyl-2-oxazoline) Coatings Developed by Low Pressure Inductively Excited Pulsed Plasma Polymerization for Biomedical Purpose. *Plasma Processes and Polymers*, pages 519–532, 2015.

[118] Stefano Zanini, Luca Zoia, Elisa C. Dell, Antonino Natalello, Anna M. Villa, R. Della Pergola, and Claudia Riccardi. Plasma polymerized 2-ethyl-2-oxazoline : Chemical characterization and study of the reactivity towards different chemical groups. *Elsevier Science*, 108(July):791–800, 2016.

[119] Meta M. Bloksma, Ulrich S. Schubert, and Richard Hoogenboom. Poly(cyclic imino ether)s beyond 2-substituted-2-oxazolines. *Macromolecular Rapid Communications*, 32(18):1419–1441, 2011.

[120] Bart Verbraeken, Kathleen Lava, and Richard Hoogenboom. Poly (2-Oxazoline) S. *Encyclopedia of Polymer Science and Technology*, (1):1–39, 2014.

[121] Jorne Raymakers. *Drug delivery systems based on gradient poly (2-oxazoline) s.* Master thesis, UGent, 2015.

[122] Norain Binti Sahari. Generation of homogeneous glow discharge using a combination of a fine wire mesh and perforated aluminium electrode. Technical report, 2013.

[123] R. V. Ghita, C. Negrila, A. S. Manea, C. Logofatu, M. Cernea, and M. F. Lazarescu. X-ray photoelectron spectroscopy study on

n-type GaAs. *Journal of Optoelectronics and Advanced Materials*, 5(4):859–863, 2003.

[124] Yu-Yuan Liew;. *The acid catalyzed hydrolysis of methyl isocyanide.* Master thesis, Memorial University of Newfoundland.

[125] Stijn; Van Vrekhem. *Adhesion improvement of a shoulder prosthesis by plasma technology.* Master thesis, UGent, 2015.

[126] Petra J M Bouten, Dietmar Hertsen, Maarten Vergaelen, Bryn D Monnery, Marcel A Boerman, Hannelore Goossens, Saron Catak, Jan C M van Hest, Veronique Van Speybroeck, and Richard Hoogenboom. Accelerated living cationic ring-opening polymerization of a methyl ester functionalized 2-oxazoline monomer. *Polymer Chemistry*, 6(4):514–518, 2015.

[127] William Reusch. Nuclear Magnetic Resonance Spectroscopy. https://www2.chemistry.msu.edu/faculty/reusch/virttxtjml/spectrpy/nmr/nmr1.htm. Date of last access: 2017-05-07, 2013.

[128] James Keeler. Chapter 2: NMR and energy levels. In *Understanding NMR spectroscopy.* 2002.

[129] Agilent Technologies. An Introduction to Gel Permeation Chromatography and Size Exclusion Chromatography. https://www.agilent.com/cs/library/primers/Public/5990-6969EN%20GPC%20SEC%20Chrom%20Guide.pdf. Date of last access: 01/06/2017, 2015.

[130] Chromacademy. Theory and Instrumentation of GC. http://www.chromacademy.com/lms/sco10/Theory_and_Instrumentation_Of_GC_Introduction.pdf. Date of last access: 01/06/2017.

[131] Thomas R. Covey, Edgar D. Lee, Andries P. Bruins, and Jack D. Henion. Liquid chromatography/mass spectrometry. *Analytical Chemistry*, 58(14):1451A–1461A, 1986.

[132] Edmond; de Hoffman and Vincent; Stroobant. *Mass spectrometry.* Wiley, 2007.

[133] Pieter Cools, Stijn Van Vrekhem, Nathalie De Geyter, and Rino Morent. The use of DBD plasma treatment and polymerization for the enhancement of biomedical UHMWPE. *Thin Solid Films*, 572:251–259, 2014.

[134] Unistudy Guides. Numerical integration. http://www.unistudyguides.com/wiki/Numerical_Integration, date of last access: 2017-04-11.

[135] Ramé Hart. Information on contact angle. http://www.ramehart.com/contactangle.htm. Date of last access: 2017-04-12, 2017.

[136] Peter R. ; Griffiths and James A. ; De Haseth. *Fourier Transform Infrared Spectrometry*. 2007.

[137] FTIR Interferometer. https://commons.wikimedia.org/wiki/File:FTIR_Interferometer.png.

[138] George Socrates. *Infrared and Raman Characteristic Group Frequencies*. 2001.

[139] S; Deimel and F. Allegretti. Elemental and Chemical Analysis with X-ray Photoelectron Spectroscopy. Technical report.

[140] XPS Setup. XPS Setup. https://chem.libretexts.org/@api/deki/files/9549/XPS-PES-Schematic-66%25.jpg. Date of last access: 01/06/2017.

[141] IUPAC. Beer–Lambert law (or Beer–Lambert–Bouguer law). http://goldbook.iupac.org/html/B/B00626.html. Date of last access: 01/06/2017, 2014.

[142] E; Meyer. Atomic force microscopy. *Progress in surface science*, 41:3–49, 1992.

[143] Q. Zhong, D. Inniss, K. Kjoller, and V.B. Elings. Fractured polymer/silica fiber surface studied by tapping mode atomic force microscopy. *Surface Science*, 290:L688–L692, 1993.

[144] Helen Greenwood Hansma. How does the AFM work. http://web.physics.ucsb.edu/~hhansma/biomolecules.htm. Date of last access: 2017-04-13.

[145] R P de Almeida Manzano, S C Naufal, R Y Hida, L O Guarnieri, and M C Nishiwaki-Dantas. Antibacterial analysis in vitro of ethyl-cyanoacrylate against ocular pathogens. *Cornea*, 25(3):350–351, 2006.